Experimenting and modelling the role of road surface detritus in the formation of potholes

Charles Djabatey

Thesis submitted to the University of Nottingham for the degree of Doctor of Philosophy

February 2023

Abstract

Although potholes are a perennial problem in UK roads, the mechanisms of their formation are poorly understood. There is no established experimental method to characterise the pothole resistance of an asphalt mixture or means of specification directly related to this phenomenon. Inspired by recent progress in geophysics, this research models the potential mechanisms of crack propagation in asphalt, under the conditions considered to increase the likelihood of this form of deterioration and develops a novel experimental framework to validate these models.

Asphalt is a complex viscoelastic multiphase material and is known to deteriorate in a number of ways, which are dependent on various environmental and loading conditions. Most commonly, the frequency of potholes is observed to increase more during the winter than in any other time of the year, which is the stimulus of the research. There are several peculiarities of the winter months potentially responsible for this e.g., higher snowfall, lower temperatures, higher precipitation, etc. However, one possibly key factor that has received little attention is the presence of detritus on the road surface. The novelty of this research is to introduce this road detritus into the modelling and experimental environment. The hypothesis is that this will lead to accelerated crack propagation by a ratchet mechanism caused by the prevention of crack closure.

Modelling this type of phenomenon has received recent attention because a similar mechanism occurs in the fracking process, where hard particles are forced under pressure into fissures in rock to keep them open permitting shale gas release. This will be exploited by applying fracking models to pothole formation, calibrating model results using the experimental data.

From the experimentation, it is concluded that the coarse-grained detritus does prevent the closure of cracks in freezing and thawing as well as in simulated tyre loading, which in turn triggers the crack to propagate faster. It is also concluded that the presence of fine-grained detritus causes failure to occur quicker when the crack propagation is entirely fluid-driven.

Acknowledgements

I want to firstly thank God, the Holy Spirit, for influencing my intelligence to get this far in my academic career.

I also want to thank my supervisors Dr. Tony Parry and Dr. Nick Thom for their patience, encouragement, and guidance through the many periods of uncertainty in a research project eclipsed by a global pandemic.

I thirdly want to thank the Laboratory Technicians, Mr. Jon Watson (no relation to Sherlock Holmes), Mr. Martyn Barret, Mr. Lawrence Pont, and Mr. Richard Blakemore. They have been instrumental to the success of this research, if it can be termed as such.

Next, I want to thank Bishop Dag Heward Mills, Bishop Richard Aryee, Reverend Clement Amaning and Lady Reverend Dr. Marie Amaning for being great counsellors, pastors, and parents to me.

Lastly, I want to thank my mother Dr. Joyce Kwapong, my sister Dr. Janice Torsu, my brother Dr. Edem Torsu and my father of blessed memory Mr. Charles Djabatey Snr for being there for 'Little Charlie'.

Declaration

The research reported in this thesis was conducted at the University of Nottingham, Department of Civil Engineering, Nottingham Transportation Engineering Centre (NTEC) between October 2018 and March 2022.

I declare that the work is my own and has not been submitted for a degree at another university.

Charles Djabatey

Nottingham

February 2023

Contents

List of Figures

List of Tables

1 Introduction

1.1 UK road network

According to the 2021 national statistics from the Department for Transport for Great Britain (England, Scotland & Wales) and the Department for Infrastructure for Northern Ireland, the UK has a road network spanning an estimated 425,000 km (GOV.UK, 2022; Northern Ireland Executive, 2021). These same sources also report that there are about 40 million vehicles using these roads. What today is a complex transportation system, started off as something very primitive, with its inception dating back to the period of the Roman occupation. These roads served as links between forts and towns and also served as trade routes for moving goods; and fundamentally that has not changed. What has changed however is the road's structure. The typical Roman road according to Maggiore (2014), was built in three layers: the first made of large stones, the second made of smaller stones, the top layer made of gravel. Situated either side of the road was also a ditch for drainage. From this original concept of road construction, the structure of UK roads has evolved into what it is today.

1.2 UK road structure

UK roads today are generally constructed with four layers: a surface course, a binder course, a base, and a sub-base course, all resting on a compacted subgrade. This is shown in figure 1.

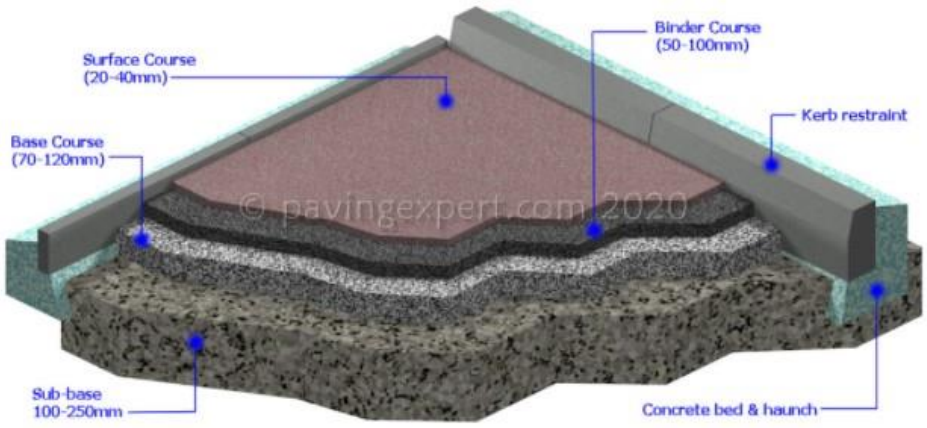

Figure 1. Structure of the modern UK road. (McCormack, 2020)

As shown in figure 1, the surface course is the part of the pavement that is directly in contact with traffic loads and is typically 20-40mm thick. The binder course beneath the top layer conventionally consists of hot mix asphalt (HMA) and is to distribute loads to the base course. The base course then provides additional load distribution and helps resist water seepage and frost damage. Lastly, the sub-base beneath it all acts as a structural support to the layers above, but also prevents intrusion of fine particles from the compacted subgrade beneath into the pavement.

1.3 Potholes

As the name suggests, a pothole is a pot-shaped hole in a road surface. It is a common and visible sign that shows a road surface is damaged, which in turn has adverse effects on the cars that drive on them. The rough edges of potholes can cause tread separation and flat tyres, as well as chips and dents to the wheels. Consistently absorbing shocks when driving over potholes also causes the vehicle's suspension to deteriorate, leading to misalignment and damage to the ball joint, shocks and struts. If deep enough, the edges of the pothole may even scrape and damage the car's exhaust system. Because of the extensive costs of repair potholes may incur to vehicle owners and city councils, it is becoming a priority of the road transportation industry to either prevent or remedy the formation of road surface potholes.

Many attempts have been made by researchers to suggest a clear mechanism by which potholes form and there appears to be some consensus on the issue. In a report commissioned by the Department for Transport (2012) entitled “Prevention and a Better Cure – Pothole Review”, it is cited that the mechanism of failure will either fall into the ‘top-down’ or ‘bottom-up’ category. Pavement damage may either commence at the top and radiate down or the damage would begin at some depth in the pavement and propagate up. “The top-down failure is essentially a localised fault that develops into fretting and becomes progressive” whereas “a bottom-up failure results from a fault at depth, usually involving the presence of water, which causes cracking and leads to a block of material breaking away.” The focus of the research project will be on the ‘top-down’ failure mechanism. Figure 2 shows an image of a pothole.

Figure 2. Fully formed pothole (Koch and Brilakis, 2011)

In an attempt to synthesise all the opinions on pothole formation to obtain a workable framework, the researcher suggests that the mechanism behind the formation of a top-down crack pothole can be divided into four main stages:

1. Crack Initiation/Presence of Voids: Apart from mastics, all asphalt pavements have air voids. These air voids are randomly distributed throughout the asphalt matrix and are largely not connected. These

dispersed air voids form the most basic building block for pothole formation. In asphalt mastics however, the inception of potholes is typically by the initiation of a tear, etching out a discontinuity in the matrix by some chemical, mechanical or thermal process.

2. Crack Propagation/Interconnection of Voids: By various processes, these dispersed voids or discrete tears can interconnect or propagate respectively. Once this occurs, a crack path with a depth is formed and is visible on the surface of the matrix. Again however, such crack paths are randomly situated across the matrix and may not converge or coalesce, even though they grow.
3. Pothole Carving/Interconnection of Cracks: At this stage, the processes responsible for crack propagation persist such that there are now, firstly sufficient crack paths in close proximity to each other. Secondly, these crack paths concentrated at an area, have also now grown considerably to the extent that they all carve out or etch out a chunk or volume of pavement, from the rest of the matrix.
4. Pothole Forming/Dislodging: Moving car tyres now exert forces, stresses and pressures on the road surface which can dislodge or displace these small chunks of loose pavement. This will persist until enough chunks are displaced to form the bowl-shaped depression in the pavement surface commonly known as a pothole.

This will serve as a framework for understanding and interpreting trends and occurrences of pothole formation for the research project.

1.4 Aim

Until recently, there has been little to no research attention geared towards gaining a better engineering understanding of how and when potholes form, how they may be predicted, and how their progression can be managed. As a result, there is no established experimental method to characterise the

pothole resistance of an asphalt mixture or means of specification directly related to this phenomenon. Therefore, one aim of the research is to establish novel and robust methods of experimentation to evaluate pothole resistance under the various environmental and loading conditions asphalt materials are subject to. This research also intends to model the potential mechanisms of crack initiation and propagation in asphalt, under the conditions considered to increase the likelihood of this form of deterioration and to validate the results using the experimental tests developed. If successful, this will form the first steps to developing and specifying asphalt materials that are more resistant to pothole formation.

In searching for a starting point to help inform the subject matter of the study, the researcher looks to an observation surrounding pothole formation widely regarded as true, but not well understood. The observation is that potholes form more frequently in the winter, than in any other time of the year. This serves as a useful first step because perhaps the peculiarities of the winter season can help isolate key factors contributing to pothole formation all year round. Being a seasonal change, obvious differences between winter and the rest of the year are in temperature and precipitation (including snowfall). To expound on this, the next step will be to also consider how the road responds to these environmental changes. Lower temperatures may make the pavement more likely to crack and less likely to flow and rut. Precipitation might cause the pavement to become saturated and thereby increase the effects of water pressure caught in the pavement's voids and pores. To best simulate a typical winter's day, the presence of road users would also have to be considered. To aid in skid resistance during the winter, grit and de-icing agents might be spread onto the road. With winter, snow sticks to car tyres and picks up dirt to deposit it onto the road surface. There are many more scenarios and factors to consider. However, to establish the framework, only those most critical to accelerated pothole formation are recreated in the laboratory. For this research, they are postulated to be:

1. Freeze thaw cycling of asphalt.
2. Top-down crack propagation under tyre-induced stresses.
3. Fluid-driven cracking or hydraulic fracturing of saturated asphalt pavements.
4. Presence of detritus on road surfaces.

An important novelty of this research will be to introduce road surface detritus, into the modelling and experimental environment. The hypothesis is that this will lead to accelerated crack propagation through a ratchet mechanism which prevents the relaxation of cracked asphalt during freeze-thaw cycling, top-down crack propagation and hydraulic fracturing.

Modelling this type of phenomenon has received recent attention because a similar mechanism occurs in the fracking process, where hard particles are forced under pressure into fissures in rock to keep them open, permitting shale gas release. This will be exploited by applying the theoretical and/or numerical models to pothole formation, calibrating the model results using the experimental data.

Hydraulic fracturing (referred to earlier) is a technology used to enhance conventional petroleum production (Chen, 2013). It plays a central role in the fast-growing development of unconventional gas and geothermal energy. This is performed by injecting fluid into a subsurface at a high rate and pressure, which opens and propagates fractures through the formation. In order to keep the fracture open, a proppant-laden fluid is injected after the fracture is created (Wang and Sharma, 2018). This draws a parallel to the formation of potholes, in that the crack frontier in the asphalt matrix may be acted on by pressurised pore water with detritus in suspension. In this case, asphalt is a ‘rock formation’ equivalent, water is a ‘fracture-fluid’ equivalent, and the detritus is a similitude of ‘proppant’. Therefore, in modelling fluid-driven crack propagation in asphalt, hydraulic fracturing models may be adopted.

1.5 Objectives

1. To develop a novel experiment to prove the existence of detritus in cracks, to examine the method of their placement, to investigate the distribution of detritus along a specimen's height and the gradation of detritus caught in cracks.
2. To develop a novel experiment and a calibrated model to investigate the potential of detritus in prevention of crack closure in freeze thaw cycling of a sample.
3. To develop a novel experiment and a calibrated model to investigate the effect of crack closure prevention on the rate of crack growth in top-down cracks induced by a sample in three-point bending. This is an approximate simulation of the tensile stresses, that are induced by a car tyre at the surface of an asphalt pavement, that cause top-down cracks to form and propagate.
4. To develop a novel experiment and a calibrated model to investigate the effect of detritus on the rate of crack growth when the crack is propagated by cyclically pressurised fluid. This is an approximate simulation of the mechanical pore water pressures, that are induced by a car tyre in the interconnected pores of a saturated pavement, that cause the cracks to propagate.

2 Literature Review

In this chapter, the researcher will review all the literature relevant to the effective carrying out of the research question on pothole formation. Therefore, the literature review will be tailored towards fulfilling the various objectives outlined in the previous chapter. First will be an overview on the basic concepts on bitumen and asphalt. Secondly, there will be an appraisal of the various literature to do with road deposited sediments and their seepage into the pavement. Thirdly, the researcher will then look at literature concerning the temperature cycling of asphalt pavements and experimental and modelling methods used to characterise the thermo-mechanical phenomena. Fourthly, an evaluation of relevant journal papers and books covering the topic of fatigue cracking will be done, which will be followed by an analysis of the sources covering mechanical pore water pressure also. Penultimately, there will be a discussion on the extent to which hydraulic fracturing models and experimental setups can be applied in a pavement engineering context. Lastly, will be an interrogation of the different variables that make winter months more ideal for pothole formation. The models, concepts and approaches found in the various papers, journals and books cited will form the knowledge base and context of the study. The limitations of these however will also carve out the knowledge gap this study intends to fill, which will all be discussed in the subsequent paragraphs.

2.1 Basic concepts on bitumen and asphalt

2.1.1 Viscosity and visco-elasticity

In the context of this research, bitumen is the binding agent used in the production of asphalt. Asphalt, therefore, is the material formed when bitumen as a binding agent is mixed in different proportions with aggregates

of varying sizes and air voids. The viscosity of a bitumen sample is determined by a penetration test, where “the test measures the viscous resistance to the penetration of a needle into a container of bitumen” (Thom, 2014). The penetration grade of bitumen used in the project is 20 pen, which means that the test needle would have a penetration of 2mm into the highly viscous fluid at a constant temperature. The viscosity of a fluid is a function of its temperature and Olard et al (2005) discusses the range of behaviour exhibited by bitumen across various temperatures as shown in Figure 3.

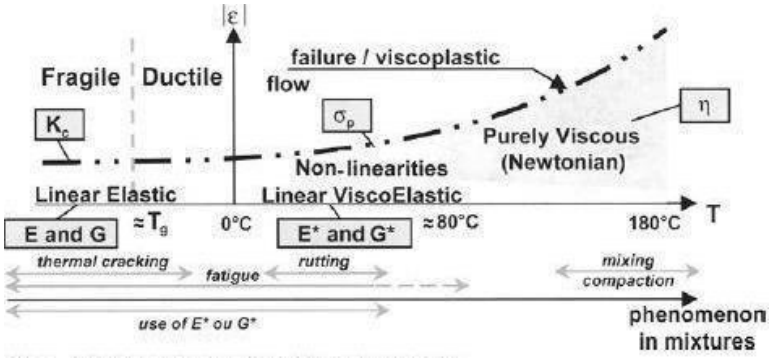

Figure 3. Typical behaviours observed on bitumens (Olard et al, 2005)

From figure 3, it is evident that at temperatures normally experienced during pavement service life, the bitumen behaviour is largely visco-elastic. This means that any deformation applied on it is recoverable, but time dependent. This characteristic is what gives rise to the temperature and time dependent nature of the asphalt pavement’s response to loading.

2.1.2 Adhesion

Adhesion is defined by the Oxford dictionary as the sticking together of two different substances. Aguiar-Moya et al (2015) class the interaction between asphalt binder and aggregate as fundamental to ensure adequate performance of asphalt mixtures. The implication of not having perfect adhesion is that the fracture will take place preferentially along one of the interfaces between an aggregate particle and the adjacent bituminous mortar (Thom, 2014). Taking the path of least resistance, the fracture would

form more easily along this frontier. One major cause of poor bitumen adhesion to aggregate is the presence of water. The work of adhesion directly affects the resistance of asphalt mixture to moisture damage because it measures the ease with which water can displace asphalt binder from the aggregate surface (Aguiar-Moya et al, 2015). This is therefore one of the cascading effects of moisture damage of asphalt; the stripping of bitumen off the aggregate's surface because of water's greater chemical affinity to adhere to the aggregates.

2.1.3 Ageing

Bitumen, being a hydrocarbon, ages. Its chemistry changes over time which triggers a change in stiffness characteristics. Bitumen ageing occurs mainly by oxidation which is influenced by temperature. During mixing, transportation, placing, compacting and any other activity occurring at elevated temperatures, bitumen ageing is taking place. (Thom, 2014) It was further explained by López-Montero and Miró (2017) that oxygen diffuses rapidly through interconnected voids, triggering chemical reactions in the aggregate-binder interface. This is cited as a major factor leading to the embrittlement of the asphalt. Another major implication of ageing binder is its reduced ability to heal, increasing the temperature threshold at which healing occurs.

2.1.4 Glass transition temperature

As earlier stated, the asphalt binder is heavily temperature-dependent, flowing at high temperatures and solid and brittle at low temperatures. According to Liu et al (2017), the change from a viscoelastic state to a glassy state [and vice versa] is defined as the glass transition. The glass transition temperature is therefore the value chosen to represent the temperature range over which this transition occurs. Below the glass transition temperature, the thermal expansion coefficient changes significantly and the asphalt binders fail due to brittle fracture (Liu et al, 2017). Moreover, it is

observed that the closer the temperature of an asphalt material is to its glass transition temperature, the more linear elastic its behaviour to applied load becomes. This becomes significant in freeze thaw cycles and at the lowest temperature to which the road surface cools. The greater the temperature change, the greater the tendency to thermal contraction. This is greeted with a response that is more elastic but more brittle if loaded above its yield strength.

2.1.5 Fatigue and fracture

Typically, failure of a material is induced by loading it beyond its yield strength. However, it is possible for the asphalt pavement to fail at a load below its yield strength, under the influence of fatigue. Under repeated loading, strains are sufficiently high to cause failure. There is a conventional understanding of failure or fracture to be a discrete crack tip being initiated and propagated through a medium. However, Thom (2014) suggests that failure in asphalt consists of enlarging existing fracture zones at contacts and developing new fractures. Figure 4 shows the image of a fracture zone.

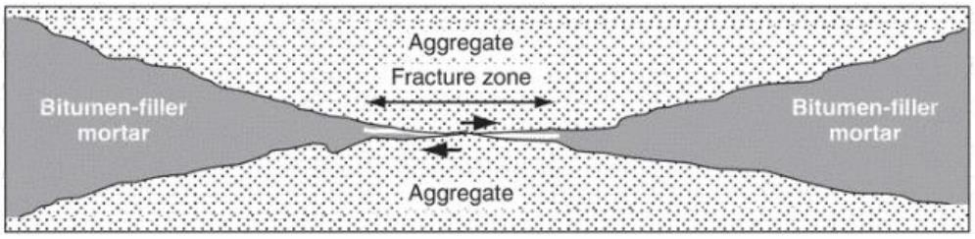

Figure 4. Image of fracture zone in asphalt matrix (Thom, 2014)

2.2 Detritus on road surface

By the proposed hypothesis, car tyres pick up dirt to deposit it onto the road surface. Once the dirt and snow are mixed, the snow melts and starts to percolate into the pavement through the cracks, transporting the dirt with it. Therefore, the quantity and particle size distribution of the dirt found in the cracks, may be a reflection of the quantity and particle size distribution of the dirt found on the road surface. A number of researchers have looked into

capturing the quantity, concentration and particle size distribution of road deposited sediments, some of which will be considered below.

2.2.1 Particle size distribution

Seleznev et al., (2019) carried out work looking at this phenomenon, known as snow-dirt sludge (SDS). 16 samples of snow dirt sludge were collected from lawn surfaces, driveways, sidewalks and road surfaces in Ekaterinburg, Russia, the snow melted off, and the particulates sieved. It was observed that about 35g of dirt was found in a litre of meltwater. This is shown in figure 5.

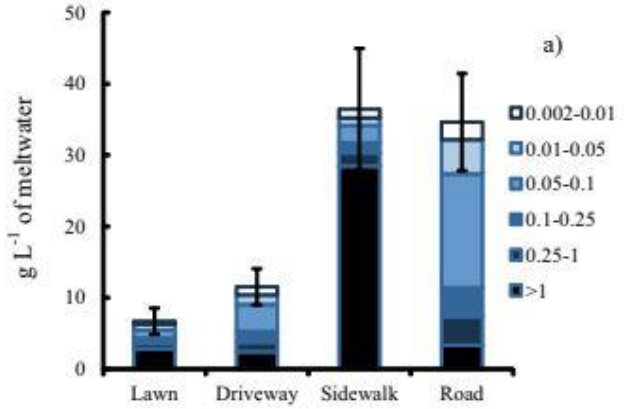

Figure 5. Absolute content of solid material in meltwater (Seleznev et al., 2019)

It was also observed that most particles found in the snow dirt sludge (SDS) were between 50-100 µm in particle size. This is shown in figure 6.

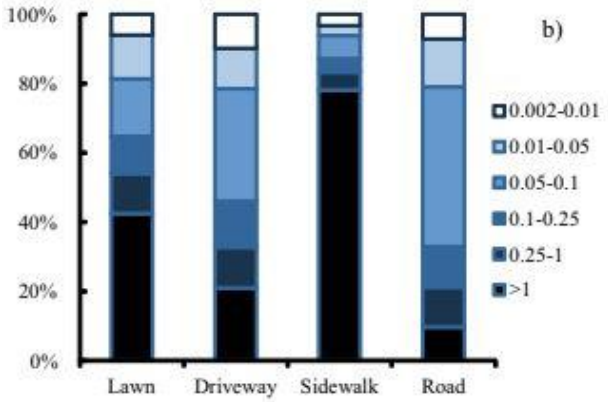

Figure 6. Relative contribution of size fractions to the mass of solid materials in SDS (Seleznev et al., 2019)

Similar research was carried out by Owens et al., (2011) in Prince George, Canada, looking at the amount of road sediment on a 1000 km stretch of road, this time however in a snow free season. The results show that most of the road deposited sediments were greater than 500 µm, and the particles passing 63 µm sieve were between 5% - 7% of the total mass. This is shown in figure 7.

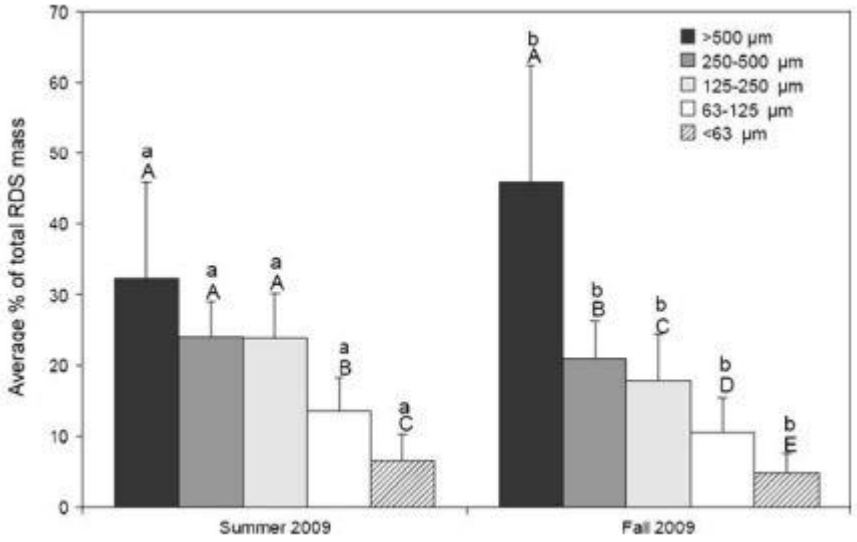

Figure 7. Grain-size mass distribution for the summer and fall 2009 sampling periods.

(Owens et al., 2011)

In Nottingham, UK, Jackson (2018) conducted a study looking again at the particle size distribution of pothole sediments on the road and arrived at a particle size distribution that saw 77% of the road sediment detritus greater or equal to a 2.8mm sieve size. This is shown in table 1.

Table 1. Particle distribution of road sediments (Jackson, 2018)

Sieve Size (mm)	% Retained on Sieve	% Retained Scaled	Mass (g)	Actual Mass in Mix (g)
6.3	20.06	22.54	112.70	112.70
4.0	36.47	40.98	204.90	204.90
2.8	12.00	13.48	67.40	31.40
2.0	8.87	9.97	49.85	63.30
1.0	7.25	8.15	40.75	63.30
0.5	2.38	2.67	13.35	13.35
0.25	1.08	1.21	6.05	6.05
0.125	0.51	0.57	2.85	2.85
0.063	0.23	0.26	1.30	1.30
Rec	0.15	0.17	0.85	0.85
Total	89.00	100.00	500.00	500.00

This already offers some insight into the quantity and grain size of sediments from the surface entering a 1mm crack for example.

2.2.2 Mineral composition

The mineral composition of the particulates was also evaluated by Seleznev et al (2019) after mineral analysis was run on the 50-100 µm sized particles. It was discovered that about 60% of the particulates were mafic rocks. E.g., basalt, diabase, gabbro, etc. Examples of Felsic rock are granite, quartz, muscovite, etc. This is shown in figure 8.

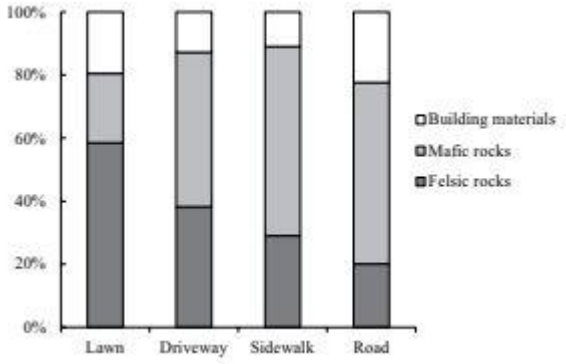

Figure 8. Mineral composition of the solid phase in snow dirt sludge (Seleznev et al., 2019)

Work carried out by Adachi and Tainosho (2005) in Kobe, Japan revealed that the road deposited sediments contained asphalt, calcium and iron bearing materials, ilmenite, quartz particles, organic matter, and tire dust. The particle size distribution and mineral analysis would be of interest to the researcher to conduct on particulates gained from cracks in the road also. Both these data sets might give more or less credence to the hypothesis of dirt being washed into the crack, as opposed to elements of the matrix breaking and falling into the crack.

2.2.3 Detritus in the crack

Once the dirt is washed into the crack by the meltwater, it sits in any existing pores close to the surface. One area of pavement engineering which looks at

the occurrence of this is the clogging of porous asphalt pavements. This is evidenced in the work done by Mahmud et al, (2021) where microstructural analysis of porous asphalt showed that clogging or reduction of air void content due to the presence of road sediments deposited in pores is most severe in the top 17mm of a circular sample 50mm in height. This is shown in figure 9.

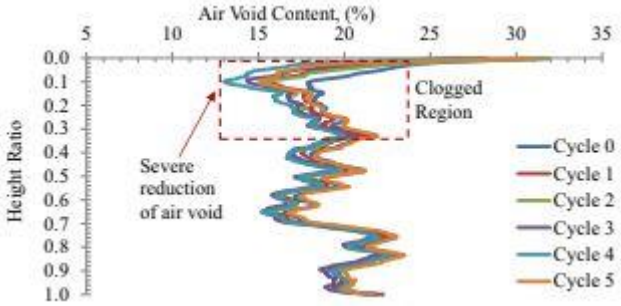

Figure 9. Effect of repeated clogging cycle on the distributions of air void content (Mahmud et al., 2021)

Assuming these pores are interconnected to form a crack path, a process similar to clogging may take place in the cracks of standard graded asphalt. Once placed, the road sediments then begin a sequence of processes which in turn progressively and incrementally widen the width and length of the crack. By a finite element model simulation, Ma et al., (2020) considered the increase in the pore water pressure of a pavement with more material clogging the pores per unit force, shown in figure 10.

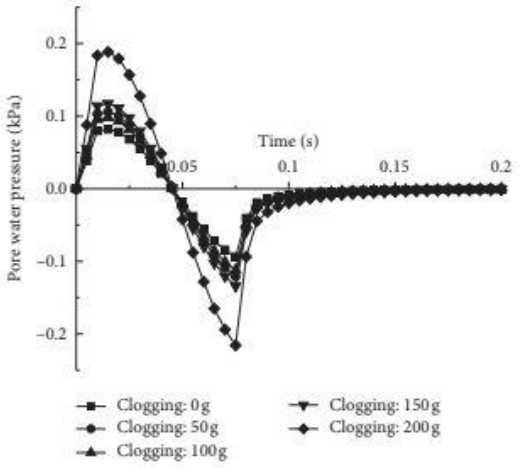

Figure 10.Pore water pressure at a depth of 3 cm and a void rate of 25% (Ma et al., 2020)

The paper demonstrates that when the pore water is prevented from draining out by the presence of the clogging material, there is an internal build-up of water pressure. An increase in water pressure per cycle of loading can ultimately accelerate crack growth, a phenomenon which will be discussed in subsequent paragraphs.

Moreover Croll (2009) acknowledges another such process of detritus acting to progressively increase crack dimensions, in a paper outlining the stages of a ratchet mechanism triggered by the presence of detritus filling the cracks, shown in figure 11.

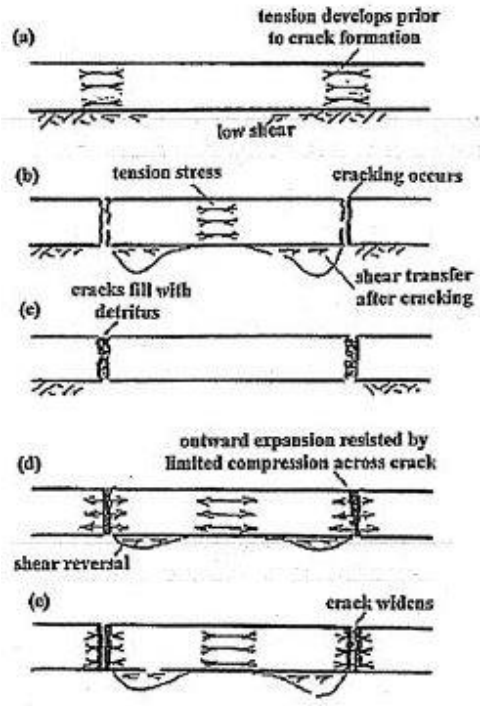

Figure 11. Schematic illustration of thermo-mechanical ratchet and growth of alligator cracking in a layer of asphalt (Croll, 2009)

He postulates that once thermal contraction/expansions from temperature variations generate cracks, detritus sits in these cracks and prevents them from reaching their original dimension, thereby causing a gradual widening each time there is expansion and contraction. This will also be discussed subsequently: the influence of temperature cycling on asphalt pavements.

2.3 Temperature cycling of asphalt

In this section the modelling, experimentation and factors affecting asphalt temperature cycling will be discussed.

2.3.1 Modelling of freeze thaw cycles

In order to understand the impact of freeze thaw cycles, their influence must be quantified and the factors affecting this phenomenon and the relationships between them characterised by some equation or formula. Vu et al., (2018) In their modelling of the behaviour of partially saturated asphalt in freezing condition postulate that the thermo-mechanical strain from freezing and thawing has 3 parts: an isothermal strain term, thermal expansion/contraction term and a volumetric expansion of ice term. By superposition, these are summed up to constitute the global thermo-mechanical strain term of the sample.

2.3.1.1 Isothermal strain term

Since the bitumen [and therefore the asphalt] behaves in a more viscous way at a higher constant temperature and therefore tends to flow and deform more, the viscoelastic and creep behaviour must be taken into account in the modelling. Vu et al., (2018) in their research characterise visco-elasticity by using the Huet model, composed of a linear elastic spring connected in series with two dashpots damping the spring's amplitude. The creep function is written with respect to time and temperature. The researcher may be more inclined to develop an empirical measurement of this strain term, rather than to derive the isothermal strain term from theory as the literature in question has propounded.

2.3.1.2 Thermal expansion/contraction strain term

The thermal expansion and contraction strain term is purely the product of the coefficient of thermal expansion/contraction and temperature difference. Vu et al. (2018) considers this coefficient to be 25 µm/m/°C,

however there are other researchers that consider the coefficient to be a function rather than a constant. Islam and Tarefdar (2015) develop two empirical formulae describing coefficient of thermal expansion and contraction as a function of temperature, over a range of -20°C to 50°C. This is shown by Equation 1 & 2.

$$CTC = (-0.0016T^2 + 0.0946T + 1.7457)10^{-5}\ per\ ℃ \quad \text{Equation 1}$$

$$CTE = (0.0004T^2 - 0.0234T + 2.781)10^{-5}\ per\ ℃ \quad \text{Equation 2}$$

$Where\ CTE = Coefficient\ of\ thermal\ expansion$

$CTC = Coefficient\ of\ thermal\ expansion$

$T = Temperature$

2.3.1.3 Volumetric expansion of ice term

There is also a term that characterises the swelling effect when temperature changes the phase of pore water to ice. With an increase in volume of 9%, the strain caused by the swelling of the ice was determined to be about 150 micro-strain by Vu et al, (2018). According to Lamothe, Perraton and Di Benedetto, (2014) the greatest values of the strain due to volumetric expansion can reach up to 250 micro-strain. They postulate a theoretical model for the calculation of maximum axial strain, based on the assumptions that during freezing:

1. Air voids are perfectly saturated with water.
2. Ice is considered incompressible.
3. Asphalt is an isotropic material.
4. Air void content is 4.4% for a sample.
5. Relative expansion of water during freezing is 9%

$$\frac{\Delta V_F}{V_0} = 3 \cdot \varepsilon_1 \quad \text{Equation 3}$$

$$\Delta V_F = V_a \times 9\% = 4.4\% \times 9\% = 3.96 \times 10^{-3} \quad \text{Equation 4}$$

$$\frac{\Delta V_F}{V_0} = \frac{3.96 \times 10^{-3}}{100\%} = 3 \cdot \varepsilon_1 \rightarrow\ \varepsilon_1 = 1320\ \mu m/m \quad \text{Equation 5}$$

Where ΔV_F is the volume change generated by freezing of water; V_0 is the initial volume of the material; V_a is the volume of air voids filled with water and ε_1 is the axial strain of material. There might need to be additionally a term added into the modelling of freeze thaw cycling for this project which factors in the influence of detritus preventing crack closure into the global equation.

2.3.2 Factors affecting freeze thaw cycles

The following factors impact the extent to which freeze thaw cycles can damage an asphalt pavement.

2.3.2.2 Void content

Beside the aggregates and the binder, air voids are the third key constituent of an asphalt pavement structure and the amount of air voids in a pavement restricts the amount of water the pavement can absorb. Xu, Guo and Tan, (2015) suggest that the region or air void content that could leave an asphalt sample most susceptible to damage from freeze thaw cycles is between 6% - 13%. This is shown in figure 12.

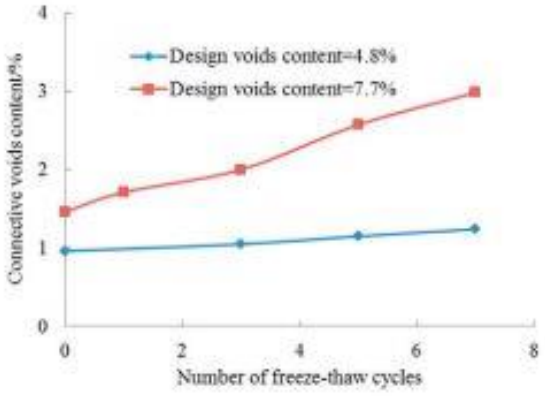

Figure 12. Connective void content for different air voids contents

(Xu, Guo and Tan, 2015)

2.3.2.3 Degree of saturation

The degree of saturation is essentially the percentage of the existing air voids that are filled with water. Understandably, more of the air voids filled with water means more of an effect the volumetric expansion of ice has for the

pavement. Xu, Guo and Tan (2015) looked at an increase in air voids for 60% and 100% degree of saturation. This is shown in figure 13.

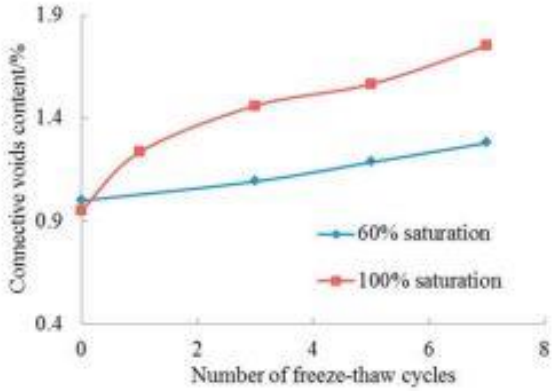

Figure 13. Connective void content for different degrees of saturation (Xu, Guo and Tan, 2015)

2.3.3 Experimentation of freeze thaw cycles

In the laboratory experimentation of freeze thaw cycles, a number of approaches have been taken by various researchers to simulate the cycling of asphalt temperature above and below freezing. This is seen in the different choices of freeze thaw regimes and testing methods for freeze thaw investigations.

2.3.3.1 Freeze thaw regimes

Fan et al (2020) first saturate their circular samples in a vacuum chamber for 15 minutes. Then they freeze the saturated samples in a refrigerator at -18°C for 12 hours and thaw them in a water bath at 60°C for 12 hours. This is done for up to 30 cycles on some samples. Duojie et al (2021) place rectangular samples in sealed plastic bags, place them in a freezer for 12 hours at -25°C and thaw them in a water bath at 25 for 12 hours. They also cite the AASHTO 283 testing procedure for freeze thaw cycles that each vacuum saturated specimen be placed in a plastic wrap, which is then placed in a plastic bag with 10 ml water. Then the plastic bag is placed in a freezer at -18°C for 24 hours and a water bath at 60°C for 24 hours. Then finally, it is placed in a water bath at 25°C for 2 hours to achieve room temperature. Some other regimes even involve the freezing of samples in either water or air, one such

being research undertaken by Xu, Guo and Tan, (2015). In terms of choice of temperature, if the research would attempt to better simulate real life scenarios during the winter months, the temperature difference cannot be so exaggerated as in the previous papers (50 - 80°C temperature difference). However, the reason for this is understandable; to magnify the effect of freeze thaw cycles to more significant magnitudes within a given number of cycles. Regarding the choice of duration, a 24-hour period is more attractive because of the issues of access to freezers and cabinets at certain hours. However, in the thawing phase, this may increase the effect of the asphalt's isothermal viscous behaviour aiding crack closure.

2.3.3.2 Test setups

Upon appraisal of the relevant literature, freeze thaw cycle testing seems to be grouped into two main categories: one where the temperature cycling affects a measurable physical property of a specimen e.g., porosity, the other where the temperature cycling affects some mechanical property of the specimen e.g., compressive strength. In the first instance, the freeze thaw cycling is essentially the main testing method, and some imaging method is taken to witness the changes made to the sample as a result of the test. With the latter however, the freeze thaw cycling is used almost as a form of conditioning of samples for the test that will measure the mechanical property being scrutinized e.g., Flexural tensile characteristics tested in a three-point bending test. The former is of more interest to the researcher; to see how the temperature cycling affects the evolution of crack dimensions, the coalescing of pores or the development of internal stresses by restrained boundary conditions. In the study by Vu et al. (2018) two experiments were conducted; the first being a cooling test in free stress conditions (CTFS) and the latter, a thermal stress restrained specimen test (TSRST). The CTFS analyses cylindrical cores [of 80mm diameter & 120mm height] with two gauges attached to measure both axial and radial strain. Strain gauges measure the response of the sample to a temperature variation of -10 to 10°C for 0.5 hours, at a rate of 40°C/hr. Most importantly however, is the free

boundary condition to allow sample deformation. This is shown in figure 14.

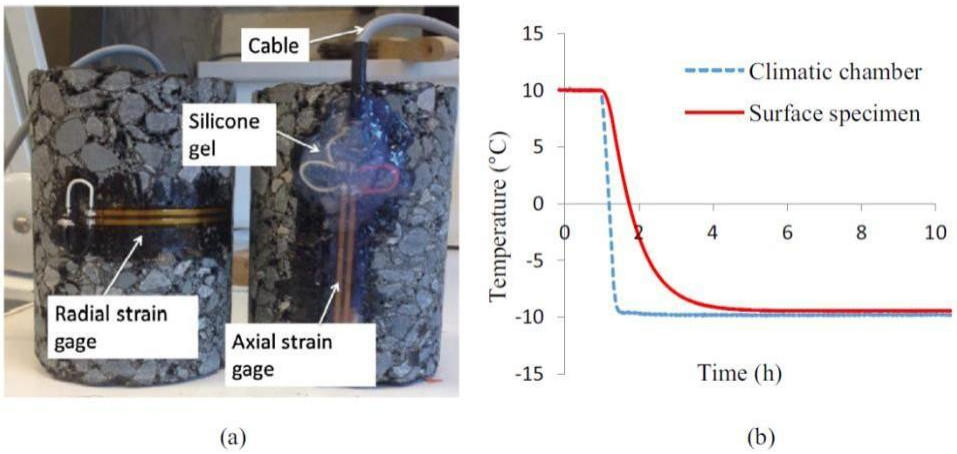

Figure 14. (a) Picture of the instrumented AC specimen.

(b) Evolution of the controlled temperature of the climatic chamber and of the temperature measured at the surface of a dry AC specimen during CTFS testing. (Vu et al, 2018)

Figure 18 shows the apparatus of a CTFS test as well as the graph of temperature to time to demonstrate freeze-thawing. As the name suggests, The TSRST conversely considers the evolution of thermal stresses in a [50mm diameter & 160mm length] cylindrical core, "clamped between two press pistons… [where] the length of the specimen is maintained constant during the test." (Vu et al., 2018) The temperature is decreased at a rate of 10°C/hr and is lowered from 18°C to -25°C. This is also shown in figure 15.

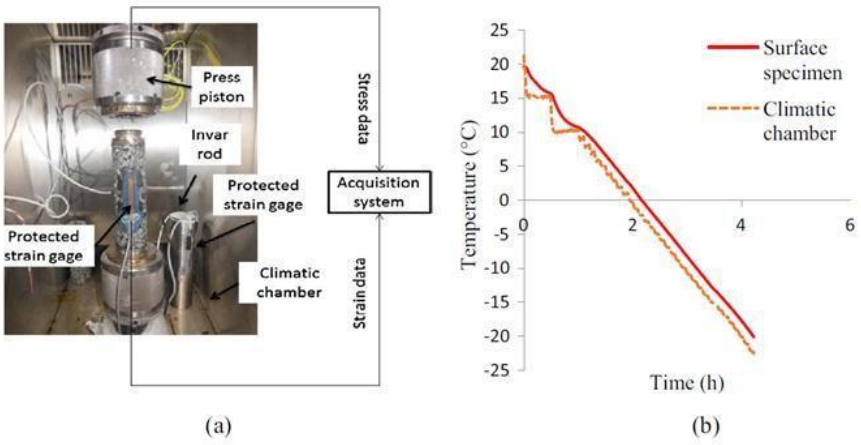

Figure 15. (a) Experimental set-up used in TRST testing.

(b) Evolution of the controlled temperature of the climatic chamber and of the temperature measured by a sensor glued at the surface of an AC specimen. (Vu et al, 2018)

Tests of this nature are useful and innovative. However, they make the inclusion of detritus into the testing environment difficult.

2.3.4 Effect of freeze thaw cycles

As earlier mentioned, freeze thaw cycles either directly affect some physical property of asphalt or indirectly affect some mechanical property. For completeness, the researcher will now discuss the effect of freeze thaw cycles on some of the mechanical properties of asphalt, namely permeability, compressive strength, and performance in flexure.

2.3.4.1 Permeability

Owing to the dilation and coalescing of existing voids and the formation of new ones from temperature cycling, the speed at which water passes through the sample in a permeability test increases with increasing freeze thaw cycles. This is evidenced in the research done by Xu, Gou and Tan, (2016), which is shown in figure 16.

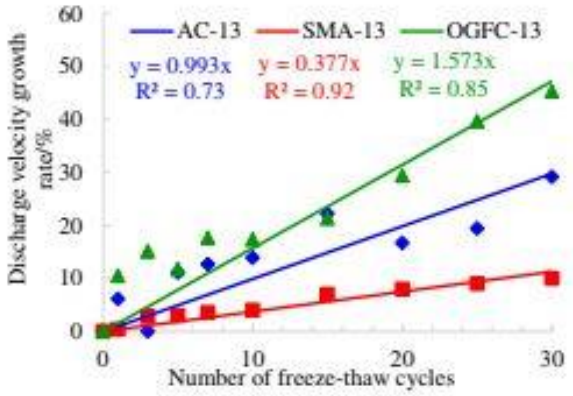

Figure 16. Discharge velocity growth rate versus number of freeze-thaw cycle (Xu, Guo and Tan 2016)

In the context of a road, this has a direct impact on the seepage of water through the surface course to eventually accumulate at a pavement layer boundary and cause frost heave.

2.3.4.2 Compressive characteristics

The compressive strength of an asphalt sample is calculated by Equation 6:

$$R_c = \frac{4P}{\pi d^2}$$ Equation 6

$Where\ Rc = Compressive\ strength\ (MPa)$,

$P = Ultimate\ loading\ at\ failure\ (N)$

$d = diameter\ of\ specimen\ (mm)$

In the work done by Si et al. (2015) the ultimate loading at failure decreased with samples exposed to increased freeze thaw cycles. Figure 17 shows this.

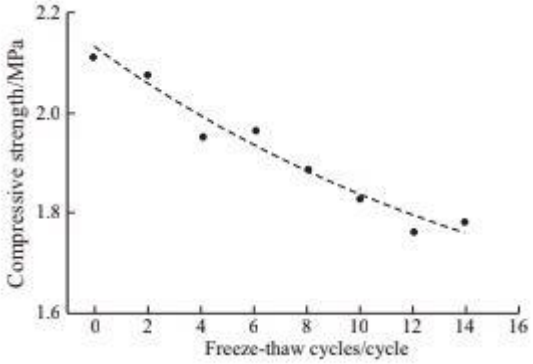

Figure 17. Impact of Freeze-Thaw cycles on compressive characteristics (Si et al., 2015)

Again, considering the effects on the UK road network, depending on the given temperature, cracking or rutting will become more prevalent in a pavement with lower compressive strength.

2.3.4.3 Flexural tensile Characteristics

Similarly, the flexural tensile strength of an asphalt sample is calculated the by the following equation:

$$R_B = \frac{3 \times L \times P_B}{2 \times b \times h^2}$$ Equation 7

$Where\ R_B = the\ failure\ flexural\ strength\ (MPa)$,

$L = distance\ between\ beam\ supports\ (200\ mm)$,

$P_B = the\ ultimate\ loading\ at\ failure(N)$,

$b = wideth\ of\ beam\ specimen\ (30\ mm)$,

$h = height\ of\ beam\ specimen\ (35\ mm)$

In the work done by Doujie et al (2021) the ultimate loading at failure decreased with samples exposed to increased freeze thaw cycles. This is shown in figure 18.

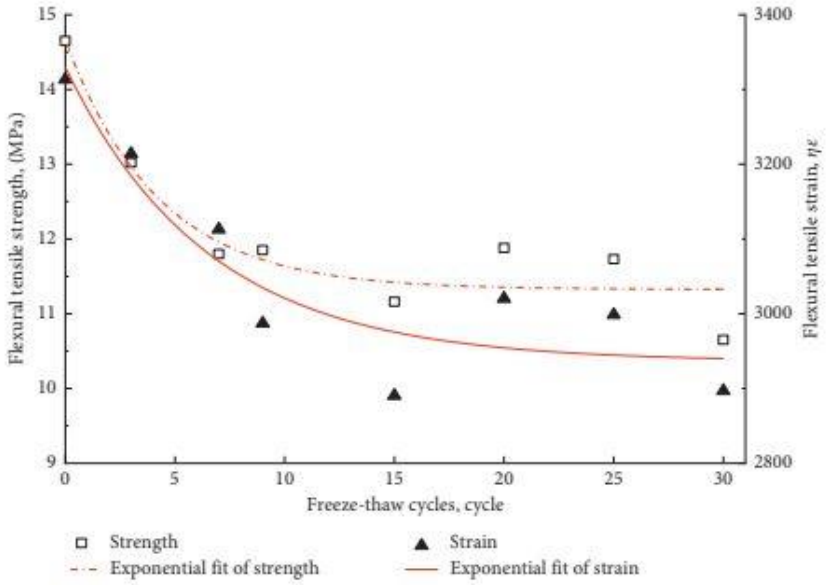

Figure 18. Relationship of flexural tensile characters and F-T cycles (Duojie et al., 2021)

This is particularly significant as tensile stress at the pavement surface is a central reason for the initiation and propagation of top-down cracks. This will be discussed in the subsequent portion of the literature review.

2.4 Cracking and failure of asphalt

Fatigue cracking is the initiation and propagation of cracks in asphalt due to cyclical loading. Fatigue cracks can propagate in different directions, can be experimented in different ways and can be modelled using different

approaches from theory or by empiricism. The subsequent paragraphs will discuss these considerations in the scope of the research project, top-down cracking, fatigue experimentation and modelling.

2.4.1 Top-Down Cracking

One key hypothesis of this research is that detritus or road debris is transported into the crack by water and may accelerate crack propagation. This is not necessarily plausible if the cracks in the surface course are all conventional bottom-up cracking caused by tensile bending stresses at the bottom of the layer. If so, the role of the detritus at the time of entry into the crack would only be to fill an already evolved crack and not to help propagate it down the layer (increase in crack length). The hypothesis is better substantiated by the presence of top-down cracking. This is shown in figure 19.

Figure 19. Image of a top-down crack from a cored asphalt sample

According to Thom (2014), cracking can occur in any area where tensile strain exists, such as:

1. The bottom of the layer under the load
2. Near the surface either side of the load
3. At the surface in the tyre tread contact zone

This is illustrated in figure 20:

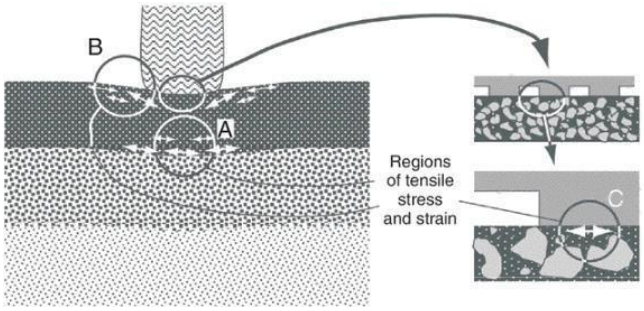

Figure 20. Tensile strains in asphalt under wheel loading. (Thom, 2014)

Figure 20 shows tensile strains in asphalt under wheel loading. Therefore, top-down cracking can be simulated in the laboratory by somehow generating a tension at the top of a sample which can push the crack down.

2.4.2 Experimentation

The following considerations cover various elements of experimentation of top-down fatigue cracking.

2.4.2.1 Test orientation

The testing methods typically adopted are indirect tensile tests, tension-compression tests and flexural testing. Most notably Portillo and Cebon (2014) adopted an adaptation of a flexural three-point test that appears inverted. This is shown in figure 21.

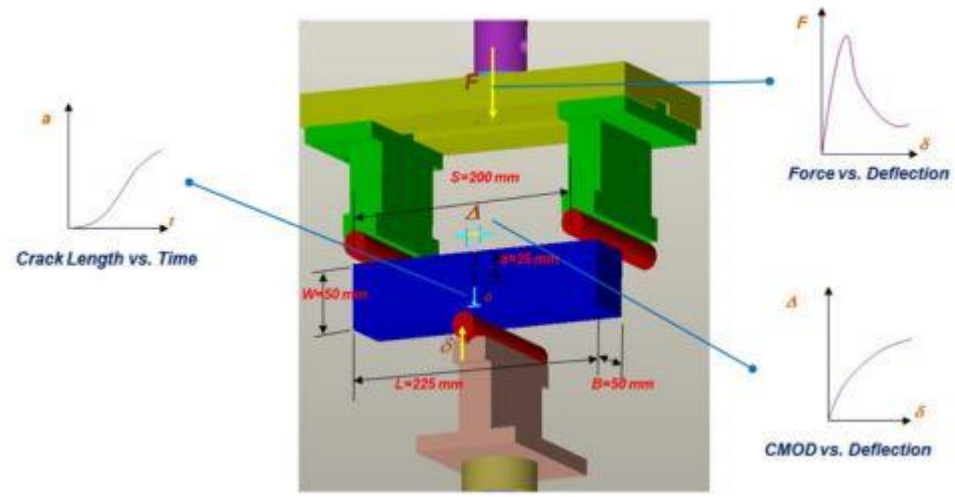

Figure 21. Three-point bend test showing inverted set up (Portillo and Cebon, 2014)

Dimensions of crack length, crack mouth opening displacement (CMOD) and deflection are recorded with time, along with the corresponding force. It is also an interesting approximation to top-down cracking in the laboratory, with tensions at the sample top surface and compressions at the specimen's base. This orientation also makes it more practical to include detritus into the experimenting environment.

2.4.2.2 Underlying layers

If a sample is tested alone, the rate of fracture will be faster than observed in the road because of the lack of underlying layers offering more stability. To better approximate the experimental setup to reality, some consideration may need to be taken on how to characterise underlying layers of the pavement. In order to simulate these layers beneath the surface course, different approaches have been made to include their effect into the experimental setup. Yin (2012) achieves this by using a rubber cushion 25mm thick, at the base of a steel mould. This is shown in figure 22.

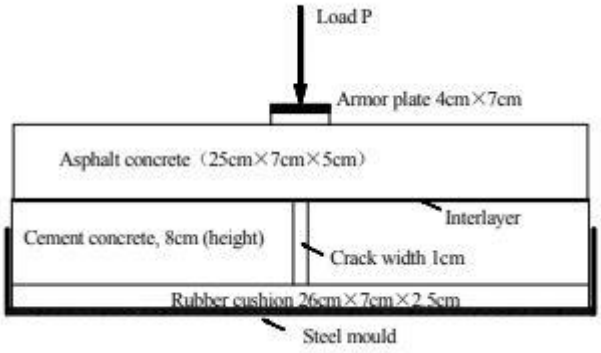

Figure 22. Experimental setup to simulate reflective cracks with rubber cushion padding (Yin, 2012)

2.4.3 Modelling

As earlier discussed, analytical models have been suggested by researchers in the prediction of thermal stresses and strains arising in the asphalt sample. However, prediction of the crack growth is yet to be addressed. There are two main methods of modelling fatigue cracking that are of interest to the researcher:

1. Phenomenological Model
2. Fracture mechanics

2.4.3.1 Phenomenological model

The fatigue of asphalt specimens using these models is not derived from theory, but more empiricism. From repeated quantitative observations, a relationship between the number of cycles to failure and initial stress or strain can be drawn. Maggiore (2014) describes these using the equations below:

$$N_f = A\left(\frac{1}{\varepsilon}\right)^b, in\ strain\ control\ mode \quad \text{Equation 8}$$

$$N_f = C\left(\frac{1}{\sigma}\right)^d, in\ stress\ control\ mode \quad \text{Equation 9}$$

$where\ N_f = Cycles\ to\ failure,$

$a, b, c, d\ are\ fitting\ constants$

There is a tendency for researchers to prefer controlled strain mode because test results are approximately independent of temperature conditions. Also, for experiments which have been modified so much that the laboratory setup has departed significantly from the theory of the model, this approach may be more practical.

2.4.3.2 Fracture Mechanics:

According to Gauthier and Anderson (2006), failure properties can be characterised in a number of ways. Of these, linear elastic fracture mechanics is the model of interest to the researcher. “LEFM is based on the assumption that the material under consideration is linear elastic in behaviour up to the point of failure.” (Gauthier and Anderson, 2006) If a crack grows, the strain energy produced by stress must exceed the energy of the newly created surface. This is what gives rise to the concept of stress intensity factor, K, describing the state of stress in the vicinity of a crack for a linear elastic material. The general formula for K is given by:

$$K_I = \sigma\sqrt{\pi a} \cdot f\left(\frac{a}{W}\right) \quad \text{Equation 10}$$

$where\ K_I = stress\ intensity\ factor,$

$\sigma = stress,$

$a = crack\ length,$

$W = width\ of\ the\ sample,$

$f\left(\frac{a}{W}\right) = Dimensionless\ quantity\ dependent\ on\ sample\ geometry$

This method is not particularly an accurate representation of the propagation of a crack in asphalt because it is not a homogeneous medium with discrete cracks. The propagation in asphalt is more of a coalescence of voids in a non-homogeneous medium. Moreover, asphalt is more visco-elastic within the range of temperatures above the glass transition temperature which is around -20°C. Nevertheless, it is a simple and useful framework that helps characterise the growth of cracks.

2.5 Water damage

According to Sun et al., (2018), water damage happens when the pavement is subject to traffic loads in the presence of water. This influences the asphalt in three ways:

1. It generates a flow field.
2. It acts as static water.
3. It may be absorbed by the aggregate.

Additionally, traffic loads result in an increase in hydrodynamic pressure in the pavement causing a pumping action. This is illustrated in figure 23.

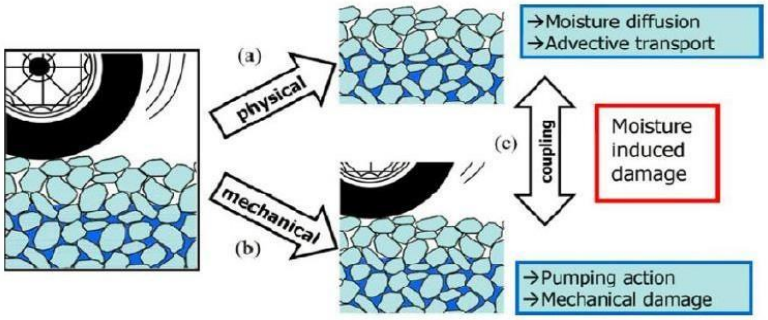

Figure 23. Separation of water Damage into physical and mechanical progresses (Kringos et al., 2008)

Figure 23 shows the separation of water damage into physical and mechanical processes. Fluctuation in the pore water pressure caused by the loading can cause stresses and induce strains in the pavement.

2.5.1 Modelling

Some researchers have looked at empirical expressions to model pore water pressure. Sun et al (2019) in his study on dynamic response characteristics of saturated asphalt pavement, uses finite element modelling to obtain pore water distribution across different asphalt layers. He also develops a relationship for determining peak pore water pressures, as shown below.

$$Y = 3.834 + 0.7019V - 0.2153T - 0.1885V^2 - 0.2893VT - 0.1455T^2$$

Equation 11

$Where\ Y = lnp_{max}$,

$V = speed$,

$T = time$

Intuitively, when a tyre goes over a road the front end of the tyre applies a pumping effect to the pavement. This is shown in figure 24.

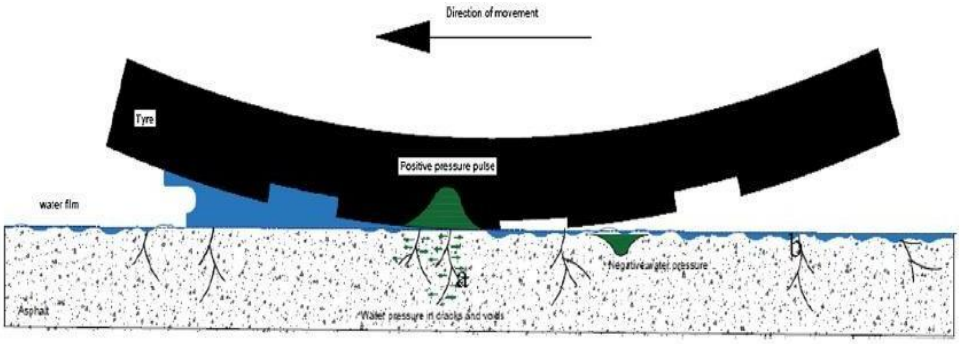

Figure 24. Conceptual illustration of the tyre-water-pavement interaction (Saeed et al 2019)

Sun et al (2019) however model and quantify what occurs from a tyre travelling off a segment of road, a suction effect at the back of the tyre (negative pore water pressure). This is shown in figure 25.

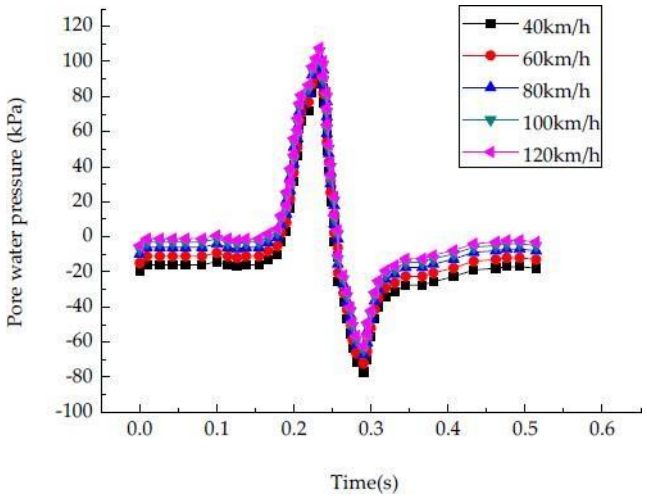

Figure 25. Pore-water pressure-time curves at middle points of upper-middle points of upper-middle layers at different speeds. (Sun et al 2019)

Figure 25 shows pore-water pressure-time curves at different speeds. From the graph we see that the lower the vehicle speed, the less the suction effect.

2.5.2 Experimentation

With regards to testing, attempts have been made by researchers to find an appropriate method of simulating tyre loads on a saturated pavement. Yilmaz and Karahancer (2012) prescribes the Hamburg wheel tracking device to measure combined effects of rutting and moisture damage by rolling a steel wheel across the surface of an asphalt concrete specimen which is immersed. Saeed et al (2019) however, attached a loading plate to an INSTRON machine to apply a 5 kN sinusoidal compression load at 5 Hz frequency to the sample. Also, they included an 80 mm concrete slab base to simulate the lower asphalt layers, a 40mm rubber pad to represent the pavement foundation and a rubber pad between the loading plate and the asphalt surface to mimic a car tyre. The loading was carried out in dry and wet conditions. In the latter, the surface was covered with 1-2mm of water.

This experimental set up at least gives a range of loads, frequencies, and thicknesses of sample and rubber to help inform decisions in the development of the novel experiments for the research. The schematic of the set-up is shown in figure 26.

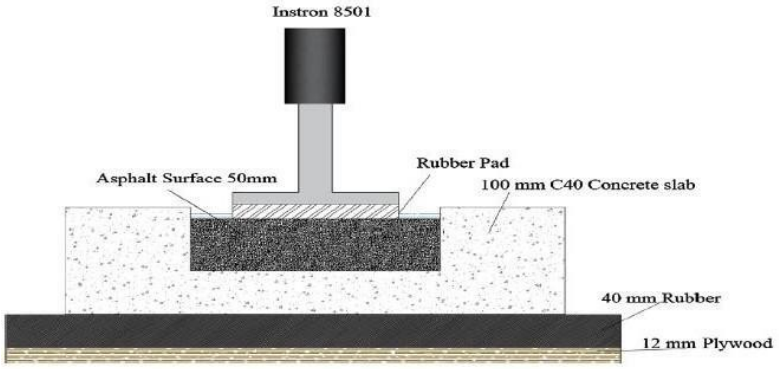

Figure 26. Schematic diagram of simulated pavement structure. (Saeed et al 2019)

Figure 26 shows a schematic diagram of a simulated pavement structure. For many researchers, there is no consideration of suction mechanism in testing for this area of research, perhaps due to the simplicity offered by its omission. Therefore, considering only pore water pressure in the range of pumping (positive pressures) may be a reasonable simplification. The methods discussed in this section characterising the effect of pore water pressure on asphalt may satisfactorily simulate the water damage effects on the asphalt surface, but not what is happening within the matrix, in the researcher's opinion. Perhaps, other fields of study may better simulate this phenomenon in the laboratory.

2.6. A significant observation

In an article entitled "Is Pothole damage really more common during winter months?", Lampe (2020) discusses a commonly observed trend that in the winter months, potholes form more than in other times of the year. Clearly, the rate of pothole formation seems to increase in the winter months and to understand why this occurs is the motivation of this research project. An appraisal of the possible peculiarities of the winter months may hold the

understanding of this commonly observed trend. It may also isolate potentially key factors which unlock the reason for this phenomenon, and it also serves as a good starting point for developing an approach to the investigation.

2.6.1 Road traffic

One may argue that perhaps there is simply more road activity during the winter months and that the problem is more to do with human behavioural patterns than some physical process. Interestingly, data from the UK Department for Transport on road traffic estimates demonstrate the converse. Figure 27 shows the road traffic (vehicle miles) in Great Britain from 2006 to 2019 on all British roads.

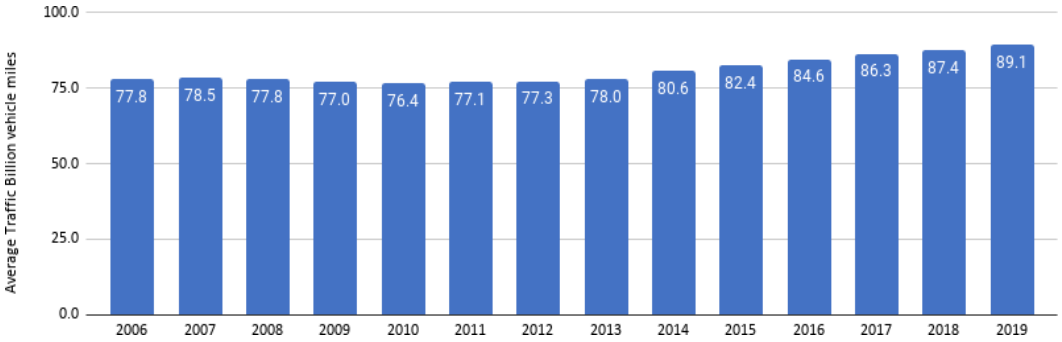

Figure 27. Graph showing average road traffic through each year from 2006-2019 (UK Department for Transport, 2020)

Figure 28 also shows the average UK vehicle miles from 2006-2019 for every quarter.

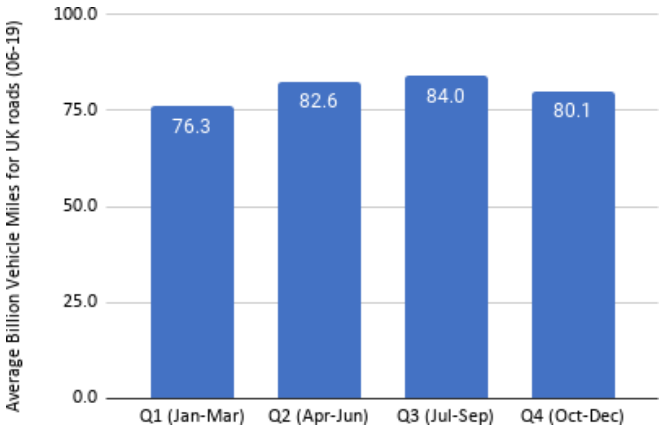

Figure 28. Graph showing average road traffic throughout each season from 2006- 2019 (UK Department for Transport, 2020)

With the winter months spanning from December through till February, the statistics show the opposite; that there is less road activity at those times of the year with more road damage due to potholes. It can therefore be safely concluded that it is not necessarily due to increased road traffic. Nevertheless, it is the wear and tear from the cyclic vehicle loads that trigger the 'Crack Initiation' and continue the distress by fatigue loading till the 'Crack propagation/Interconnection of voids' is complete. Thereafter, the action of the car tyre at speed facilitates the 'Pothole forming/dislodging'.

2.6.2 Temperature cycling

The temperature of the asphalt road is a major contributing factor to pothole formation. When the temperature reduces, asphalt becomes more brittle and is more prone to micro-cracks forming and propagating. This facilitates the first step of the top-down failure mechanism: 'crack initiation'. Secondly, the cycling of temperature above and below freezing (during ground frost days) causes the pavement to thermally expand and contract respectively. What hence happens to the cracks is that they contract in width above the freezing point (0°C) and expand in width below freezing, much like an expansion joint. By Poisson's ratio, a change in crack width will in turn encourage a change in crack length and will aid in the acceleration of the second stage of the top-down failure mechanism: 'Crack Propagation/Interconnection of voids. Aside from the impact to the asphalt, the changing temperatures also affect the water trapped in the cracks and pores of the pavement. When the temperature descends below freezing, the water in the pavement expands volumetrically by 9%, inducing internal stresses in pores which further widens cracks. Figure 29 shows the potholes reported in the UK from 2006 to 2019.

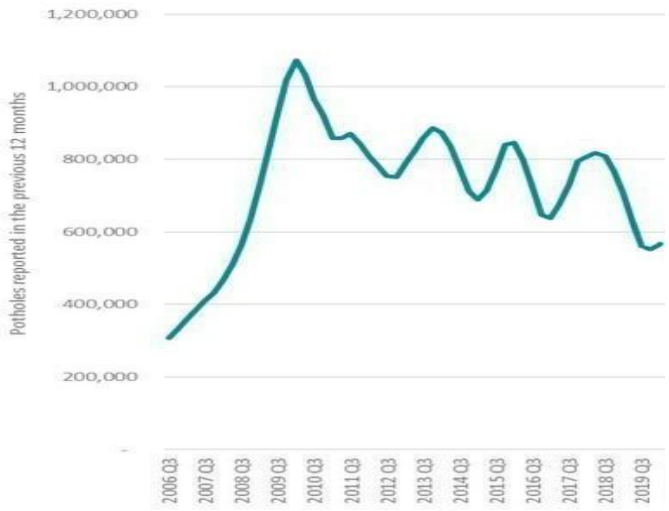

Figure 29. Graph showing reported potholes each year. Shah (2020)

This is to be compared to Figure 30, showing the number of frost days in the UK from 2006 to 2019.

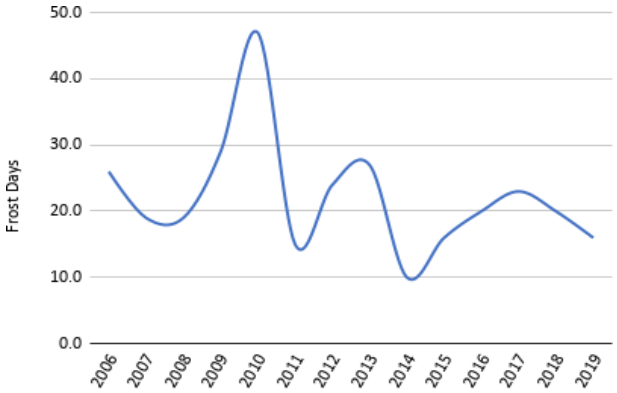

Figure 30. Graph showing frost days in London, UK from 2006-2019. Source: Weatheronline.com

It is evident that there is a positive correlation between freeze thaw cycling and pothole formation, as their peaks coincide in the same year (2010), and they follow a similar and generally downward trend. Moreover, it is also evident that the frost days for the year largely occur during the winter months. Figure 31 shows the number of frost days that occur in each month averaged over thirteen years from 2006 to 2019.

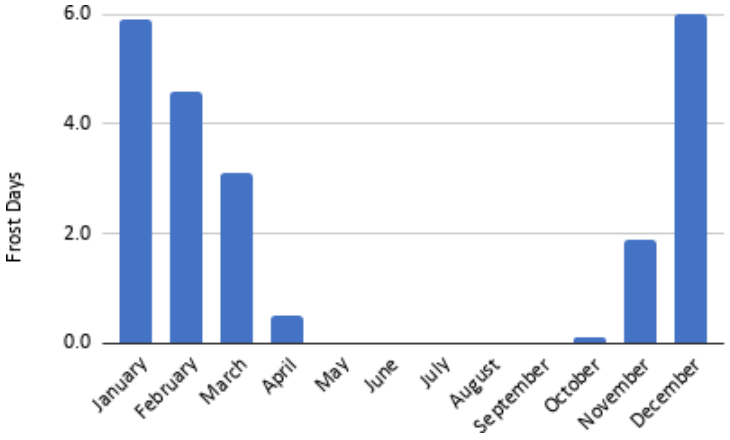

Figure 31. Graph showing average number of frost days in London, UK in each month from 2006- 2019. Source: Weatheronline.com

2.6.3 De-icing salt

According to McSweeney et al. (2016), more than 2 million tonnes of salt are spread onto UK roads every year at a cost of over £150 million. The reason for these large quantities and this great expense is because salt is the method used to melt the ice and snow that cover road surfaces during the winter. This is because salt, when added to ice, lowers its freezing point (from 0°C to -5°C for example). Therefore, at a given temperature of -1°C for instance, the ice or snow changes phase to liquid. This therefore is a secondary peculiarity, one that exists in response to snow/ice which is a primary driver of pothole formation. The de-icing salt interestingly can help reduce the impact of freeze thaw cycling because temperatures lower than 0°C are required to induce the internal stresses from the volumetric expansion of ice, as earlier discussed. However, in another way it does negatively affect the pavement because the presence of salt converts all the snow, ice and sleet precipitation into liquid form faster, which will seep through and saturate the road's cracks and pores.

2.6.4 Higher precipitation

Rainfall, snow, sleet or hail prove an important factor in pothole formation. This is because these forms of precipitation eventually seep through cracks and pores to saturate the pavement. As earlier discussed, this is even true in the case of snow and ice because they become meltwater in the presence of salt. The winter months demonstrate a marked increase in precipitation relative to the rest of the year. Figure 32 shows the average monthly precipitation values from 2006-2019.

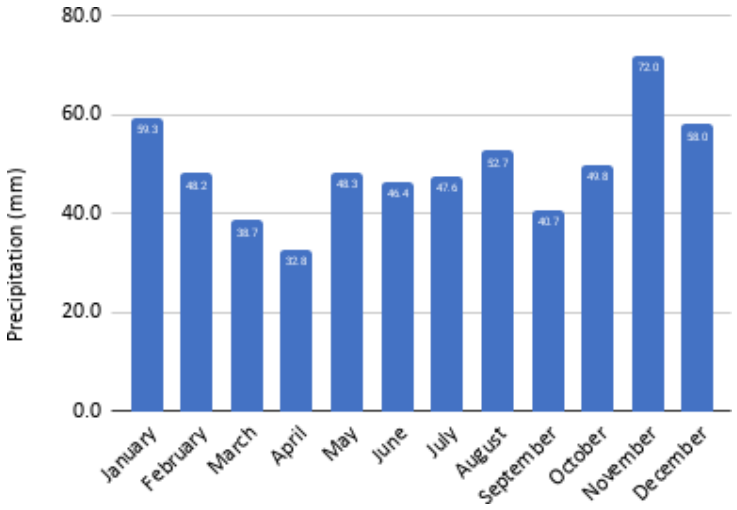

Figure 32. Graph showing average monthly precipitation in London, UK from 2006-2019. Source: Weatheronline.com

The months of November, December and January show the three highest precipitation levels across a thirteen-year span. With pavements closer to the condition of 100% saturation, larger pore water pressures are generated when a tyre goes over the road. This can in turn result in fluid-driven 'Crack Propagation/ Interconnection of voids'. Figure 33 shows annual precipitation levels from 2006-2019.

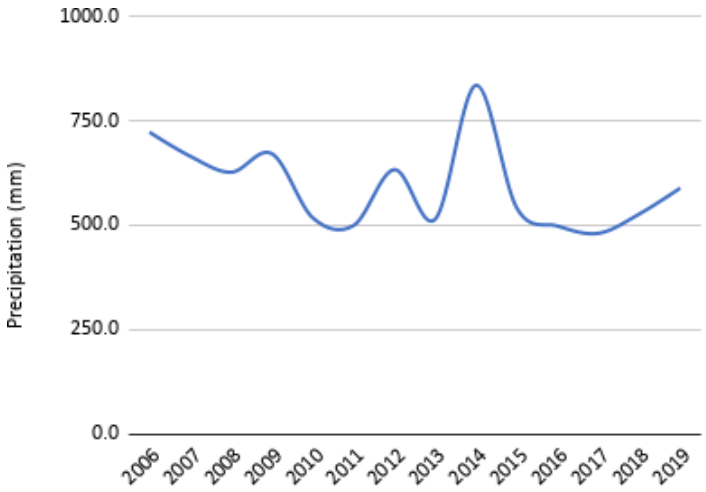

Figure 33. Graph showing annual precipitation levels in London, UK from 2006-2019

Source: Weatheronline.com

2.6.5 Other variables

Other factors unique to the winter months include fewer daily hours of sunshine, higher wind speeds, among others. Albeit relevant, these do not seem to be leading contributors to pothole formation in the UK, but however feed into more primary factors e.g., lower average temperatures coupled with less sunshine may mean snow will not readily melt and so requires an alternative method (de-icing salt).

2.6.6 Snow adhesion and detritus

As earlier mentioned, snow is one of the forms of precipitation that falls on the road surface during winter and increases the potential of the pavement to be saturated. However, the snow poses a unique problem that is discussed in an article by Pflanzer, (2015). He explains that “once snow is on the ground… it goes through a process called dry deposition, in which dust and dirt particles stick to the snow.” Scott (2013) discusses one significant effect of this: that the presence of the dust reduces the snow’s albedo – how much light it reflects off its surface – and therefore increases the amount of energy from the sun the snow absorbs, causing it to melt much faster. Once the sediments aid in accelerating the melting of snow, they are then transported

into cracks by the meltwater. Seleznev et al., (2019) also demonstrate this, as they evaluated “the formation of snow-dirt sludge (SDS) via the mixing of snow and surface-deposited sediment by vehicles and pedestrians.” They cite that “the average content of the SDS solid phase was approximately 35 gL^{-1} of meltwater on heavy traffic roads, of which the dust fraction (<0.1mm) accounted for 23 gL^{-1}.” Relative to the other forms of precipitation, snow therefore has the greatest potential to wash impurities and detritus into cracks because of its good adhesive properties. Figure 34 shows average monthly snow depth from 2006-2019.

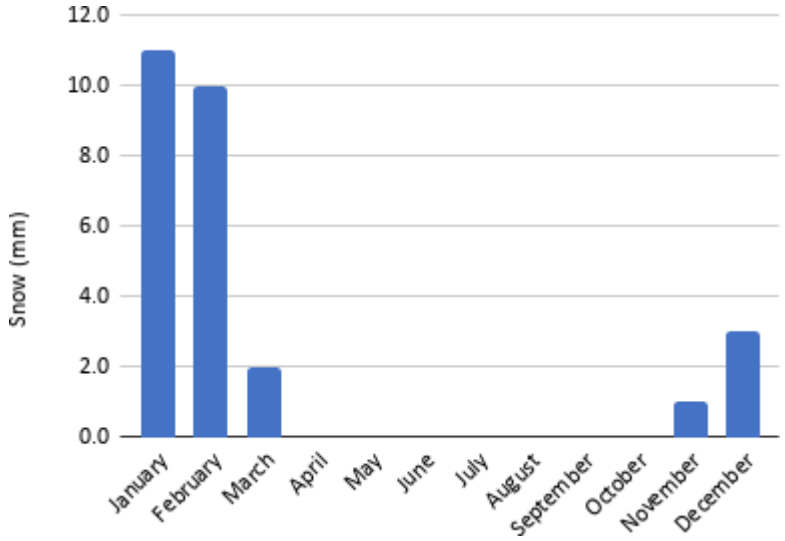

Figure 34. Graph showing average monthly snow depth in London, UK from 2006-2019 Source: Weatheronline.com

Figure 34 demonstrates that the winter months have more snow precipitation which has an increased potential to trap and collect detritus and wash it into pavement cracks. How the sediments or detritus may act will be to prevent the relaxation or closure of cracks. In other words, they will directly impact the crack width and indirectly affect the crack length or ‘Crack propagation/Interconnection of voids’ phase of pothole formation. This is the novelty and hypothesis of this research: that the presence of grit or road surface detritus inside a crack contributes to accelerate crack propagation by preventing the relaxation of cracked material under the cyclic actions of freezing-thawing and tyre loading. In hydraulic fracturing, a similar

mechanism exists where hard particles are forced under pressure into fissures in rock to keep them open in order to harness shale gas. Detritus caught in a pavement crack seems to parallel this process, especially when tyre loading pressurises the meltwater also caught in the top-down crack.

2.7. Hydraulic fracturing and proppant technology

The fracking process in shale gas release, has two key elements: the fluid driven fracture of rock formations and the proppants within the fluid that keep rock fissures open. The literature surrounding the modelling and experimentation of these will be discussed below.

2.7.1 Hydraulic fracture models

As earlier stated in Chapter 1, Hydraulic fracturing is a technology used to enhance conventional petroleum production (Chen, 2013). It plays a central role in the fast-growing development of unconventional gas and geothermal energy. This is performed by injecting fluid into a subsurface at a high rate and pressure, which opens and propagates fractures through the formation. In order to keep the fracture open, a proppant-laden fluid is injected after the fracture is created (Wang and Sharma, 2018). The parallel this draws to the formation of potholes is that the crack frontier in the asphalt matrix is acted on by pressurised pore water with detritus in suspension. In this case, asphalt is a 'rock formation' equivalent, water is a 'fracture-fluid' equivalent, and the detritus is a similitude of 'proppant'. Therefore, in modelling fluid-driven crack propagation in asphalt, hydraulic fracturing models may be adopted. There are three significant phenomena to model:

1. Crack propagation
2. Fracture opening
3. Proppant Volume & Concentration

2.7.1.1 Crack propagation

O'Keeffe, Huppert and Linden (2018) employed linear elastic fracture mechanics to characterize the propagation of a crack through an elastic medium. The model suggests that a fracture will only propagate provided the stress intensity factor is greater than the material toughness. This is shown below:

$$K_I = K_{IC} \quad \text{Equation 12}$$

$$K_{IC} = \sqrt{2\gamma_s E'} \quad \text{Equation 13}$$

$where\ K_{IC} = fracture\ toughness$

$\gamma_s = fracture\ surface\ energy\ of\ the\ elastic\ medium$

For a penny shaped radial fracture, as shown in figure 35, the stress intensity factor is defined as:

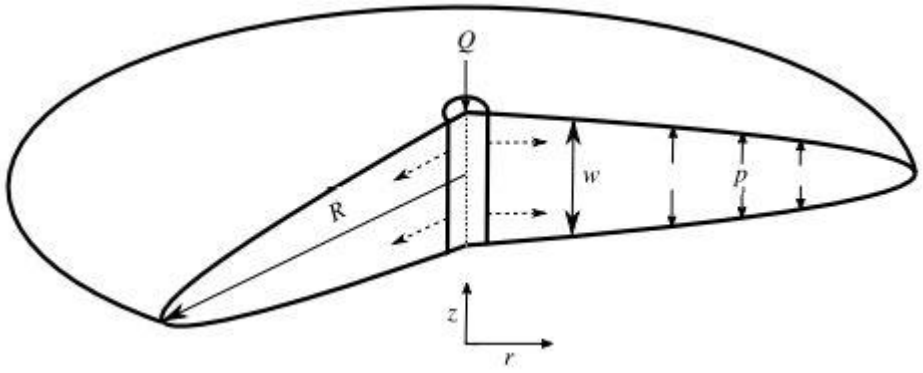

Figure 35. Schematic diagram showing the radial fracture geometry (O'Keeffe, Huppert and Linden, 2018)

$$K_I = \frac{2}{\sqrt{\pi R}} \int_0^{R(t)} \frac{p(r,t)}{\sqrt{R^2 - r^2}} r\ dr \quad \text{Equation 14}$$

2.7.1.2 Fracture opening

From the work done by Bessmertnykh, Dontsov and Ballarini (2020), an equation is developed between the fracture width and fracture depth, which is shown in Figure 36:

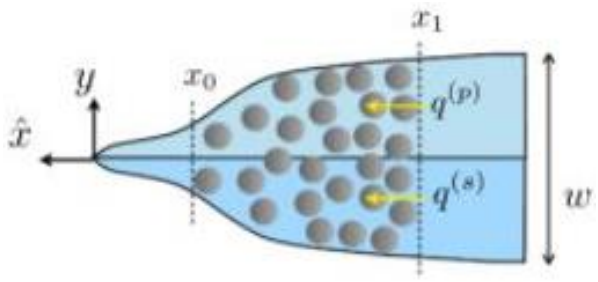

Figure 36. Schematics of a plane strain hydraulic fracture (Bessmertnykh, Dontsov and Ballarini, 2020)

$$w(x) = \frac{K\prime}{E\prime} x^{1/2} - \frac{4}{\pi E\prime} \int_0^{\infty} F(x,s) \frac{dp(s)}{ds} ds \qquad \text{Equation 15}$$

$$where\ F(x,s) = (s-x) ln \left| \frac{x^{1/2}+s^{1/2}}{x^{1/2}-s^{1/2}} \right| - 2x^{1/2}s^{1/2} \qquad \text{Equation 16}$$

$where\ w(x) = width\ of\ crack,$

$x = crack\ length,$

$K' = Scaled\ Fracture\ Toughness,$

$E' = Scaled\ Youngs\ Modulus$

2.7.1.3 Proppant volume and concentration

Again, from the work of Bessmertnykh, Dontsov and Ballarini (2020), The equation for proppant concentration is shown in Equations 17-20 and in Figure 37:

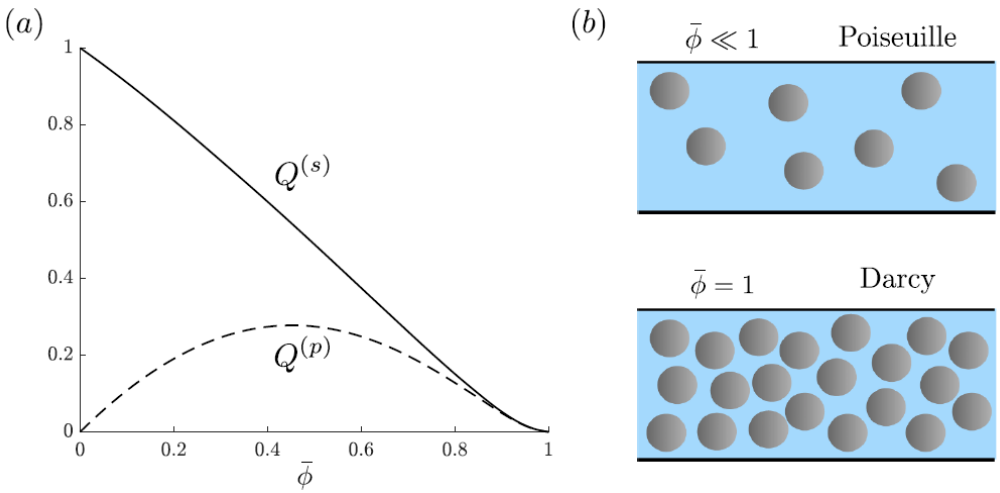

Figure 37. (a) Variation of normalized volumetric slurry flow Q(s). (b) Schematics of the limiting regimes of slurry flow in a channel. (Bessmertnykh, Dontsov and Ballarini, 2020)

$$B\left(\frac{w}{a}\right)\hat{Q}^{(p)}\left(\bar{\phi},\frac{w}{a}\right)\left(V+2C'\frac{\sqrt{Vz}}{w}\right)-V\bar{\phi}(w(z),z)=0 \qquad \text{Equation 17}$$

Where $B\left(\frac{w}{a}\right)$ is the blocking function,

V is the crack propagation velocity.

$\hat{Q}^{(p)}\left(\bar{\phi},\frac{w}{a}\right)$ is a function defined below:

$$\hat{Q}^{(p)}=\frac{Q^{(p)}(\bar{\phi})}{\hat{Q}^{(s)}\left(\bar{\phi},\frac{w}{a}\right)} \qquad \text{Equation 18}$$

Where $Q^{(p)}(\bar{\phi})$ is the normalized proppant flux coefficient.

$$B\left(\frac{w}{a}\right)=\frac{1}{2}H\left(\frac{w}{2a}-N\right)H\left(\frac{w_B-w}{2a}\right)\left[1+\cos\left(\pi\frac{w_B-w}{2a}\right)\right]+H\left(\frac{w-w_B}{2a}\right)$$

Equation 19

Where N is the bridging factor and w_B is the critical width.

$$B=\begin{cases}1, & w>w_B=2a(N+1)\\ 0, & w<2aN\end{cases} \qquad \text{Equation 20}$$

2.7.2 Experimentation

The experimental program set up by O'Keeffe, Huppert and Linden (2018) mimics very well in the laboratory, the nature of hydraulic fracturing in the real-life context. A transparent hydrogel is poured around a syringe which is connected to a syringe pump and allowed to harden. The dimensions of the mould housing the hydrogel and the positioning of the syringe tip is chosen such that the fracture propagates towards the camera. Since the crack will always follow the path of least resistance, the setup is done in such a way that the shorter distance is in the direction of fluid flow through the needle. This is shown in figure 38.

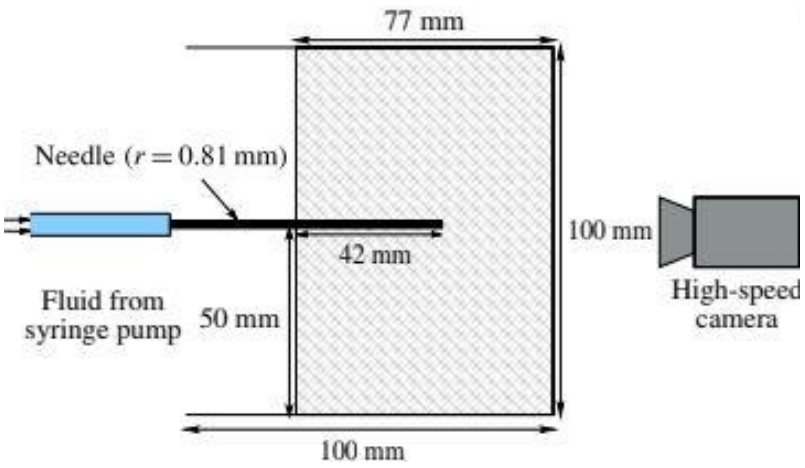

Figure 38. Schematic diagram of experimental set up in elevation view

(O'Keeffe, Huppert and Linden, 2018)

A camera is the data acquisition tool to measure fracture surfaces. In applying this to asphalt, the first issue is that with asphalt requiring compaction, a syringe set in the centre of it will be damaged. Secondly, even if a hole is made and the syringe is placed in the centre and backfilled, the presence of interconnected voids will simply mean that the water will leak out of voids and not drive any cracking. As a remedy, either homogeneous bitumen or an asphalt filler blend mastic may be adopted. If so, another challenge is posed in seeing the evolution of a crack using camera data acquisition because the sample would be black and opaque. There are evidently some challenges with adopting this approach to asphalt. However, it is still a relevant starting point which, with some adaptations, holds greater possibilities for characterising fluid driven crack propagation within pavements than the existing tests in the current literature.

2.8 Summary

In summary, these are the literature finding relevant to the research project. Firstly, was a look at some basic concepts surrounding bitumen and asphalt. Secondly was a look at detritus on the road surface and in surface cracks. Thirdly was a review of literature on temperature cycling. In considering the experiments on temperature cycling and the effect of freeze thaw cycles, there however seemed to be no method which focused on the evolution of a crack's width over time. Even though radial and axial strains are recorded, there may yet be an adaptation of a freeze thaw cycle experiment that more closely mimics what is visibly observed in the road i.e., crack mouth widening at the surface. Thereafter, was a look at fatigue cracking. Particularly important was the inverted three-point bending test setup used by Portillo and Cebon, (2014) to characterise top-down cracking and validate fracture mechanics models. This presents a good simulation of cracks and their propagation in the laboratory. Concerning the literature discussing the experimentation of water damage on asphalt, there appeared no significant source to inform the researcher in determining a suitable test. There however appeared to be a method applied in fluid driven fracture of hydrogels proposed by O'Keeffe, Huppert and Linden (2018) of a needle set in a matrix, which may better approximate the pore water pressure effects evident in saturated pavements. This may require some adaptation to best apply it to asphalt. Finally, was an unpacking of the various environmental conditions unique to winter that potentially have a bearing on accelerated crack propagation and thereby pothole formation. The stand-out parameters to be tested in the research were identified to be road traffic, precipitation, freeze thaw cycling and detritus on the road surface. These isolated factors will form the framework of testing, with road surface detritus as the novelty and focal point of the experiments.

Overall, the project considers the nature of the asphalt matrix and its response to temperature and loading rate, being a visco-elastic material. In this case, the asphalt's response under the influence of freeze-thaw cycles

and tyre loading will be measured by the rate of crack propagation. The purpose of the experiments in this research therefore is to simulate the loads and actions applied on a strip of asphalt road on a typical winter's day. The parameters to be measured would be crack width at the surface, crack length and any internal stresses and strains. A critical appraisal of the relevant and existing literature reveals a knowledge gap in the understanding of pothole formation, stemming from either ineffective simulation of road actions in the laboratory or failure to include key factors in designing the experiments. Once a typical winter's day can be reasonably recreated in the laboratory, the researcher argues that a framework is then established to investigate the role of detritus as a potentially key missing parameter in crack propagation. Analogous with the role of proppants in a hydraulically fractured rock, detritus tested in a suitable experimental context may be demonstrated to prevent crack width closure and thereby ratchet crack length elongation.

3 Methodology

3.1 Introduction

The experimental design of this thesis is intended to investigate the different circumstances under which the pavement is most likely to fail. On a typical winter's day, several events take place in an asphalt pavement crack. If top-down cracking of a saturated pavement is assumed, the most significant of these events contributing to crack propagation will be reviewed in the scope of this study. These are the following:

1. The presence of detritus in a road, substantiated by what will be known as the 'Detritus in cores experiment'.
2. Freezing and thawing of water in the pavement crack and its associated thermal expansion and contraction, simulated in what will be known as the 'Freeze thaw cycling experiment'.
3. Tyre loading from vehicles leading to tension applied on the crack mouth at the pavement's surface, simulated in what will be known as the 'Three-point bending experiment'.
4. Tyre loading of vehicles leading to increased water pressure in pavement cracks, simulated in what will be known as the 'Hydraulic fracturing experiment'.

If these are taken to be the most significant contributors to top-down crack propagation, the winter pothole problem becomes easier to characterise. Moreover, if it is taken that these are the various conditions under which detritus works, it also becomes easier to determine which process detritus influences most greatly to aid in crack propagation. It is true that these processes are related and combine to affect the complete response of the pavement crack. However, for purposes of simplicity, they will be investigated independently.

This is the framework of loading and environmental conditions that the

asphalt crack is subject to in the researcher's investigation. There are other factors that were excluded such as the effect of de-icing agents on the pavement. Another potential factor excluded was the complex shear and compressive stress profiles generated in a vehicle wheel path. The fundamental reason for these exclusions in the experimentation is that the research is inherently comparative, looking at the effect of crack propagation with and without detritus preventing crack widths from returning to their original size after loading. Therefore, the study does not demand that the experiments exactly mimic the events happening in the actual road pavement, but that key actions exist in the testing. Therefore, the influence of temperature is represented and so are the two key resultant impacts of tyre loading; a crack opening at the pavement surface and propagating at the crack tip, as well as the fluid in that crack being pressurised. This offers enough resemblance to the reality on the road, such that the impact of detritus in a crack can be sufficiently investigated and for the findings of the investigation to be meaningful to real-life scenarios. It must be established however that in pursuing a robust experimental framework, the purpose of the study is to offer enough breadth in covering key contributors to pothole formation. Once this is successful, it forms the basis for in depth study of the key parameters in further research, even beyond the scope of this study.

Regarding the role of detritus however, it must again first be established whether it exists in cracks in real-life scenarios. After this, two concepts will be investigated: Development of crack width with detritus and the effect of changes in crack width (due to detritus) on crack propagation.

In the subsequent paragraphs, there will therefore be an evaluation of the generic experimental and testing techniques which make up the complete method of the PhD study. The researcher will hereafter consider the manufacture or sourcing of samples for testing, their storage, the testing rigs these samples are placed under and the methods to glean meaningful data from them. Also, there will be an overview of how novel experimental equipment was developed, forming the framework of the experimentation.

3.2 Materials

The first material used in this project is a 10mm Stone Mastic Asphalt (SMA). This is chosen because it is the typical material used in the UK road network, for the construction of a surface course. The aggregate type was granite (from Aggregate Industries' Bardon Hill quarry). The design for the asphalt mixture was based on a 0/10mm size surface course according to British Standard BS EN 13108-5.

A 20-penetration grade bitumen from a Venezuelan crude source was used throughout this project. The penetration grade was chosen to encourage the samples to exhibit less ductile behaviour in experimentation so as to generate cracks that are more defined and easier to measure.

The grading specification for the 10mm SMA is reported in Table 2 whereas the design gradation curve is shown in Figure 39. Four lines are presented: the upper and the lower limits, the midpoint curve from the British Standards and the aggregate gradation.

Table 2. Percentage passing for sieve sizes used to form grading envelope.

Test sieve aperture size (mm)	Passing sieve (% by mass)
14	100
10	90 – 100
4	40 – 50
2	20 – 35
0.063	5 – 13

According to the British Standard, in addition to 14mm, 10mm, 2mm and 0.063mm test sieve sizes, a fifth sieve size can be included in determining the grading envelope. From the guidance given by the British Standard, the researcher chooses this grain size to be 4mm.

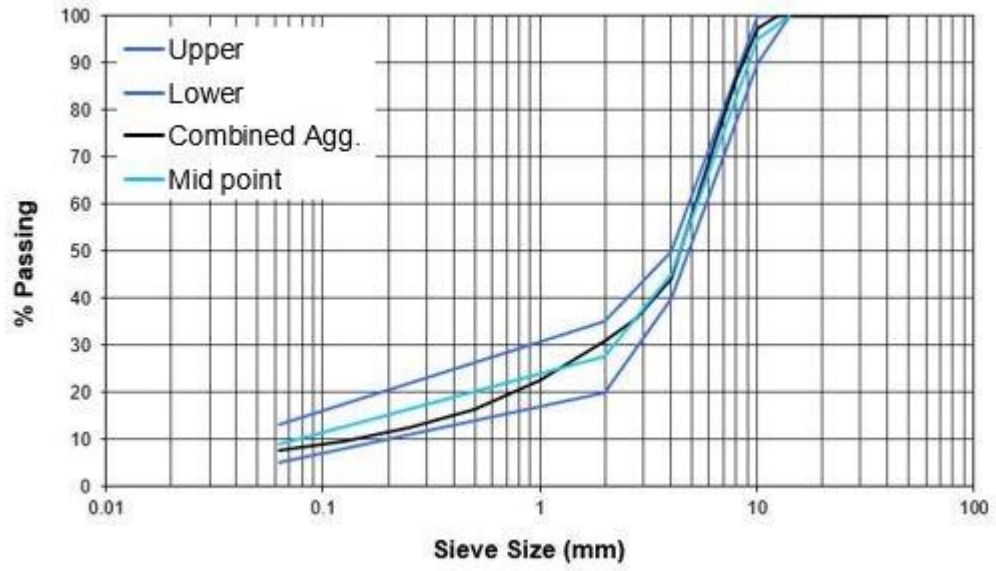

Figure 39. Graph showing design gradation curve.

The second material used in the project is a 50% asphalt filler blend mastic. This is a mixture consisting of 160g of 20 penetration grade bitumen and 160g of Bardon hill granite filler material, mixed over a hot plate. The filler blend mastic is set at 50% filler content because typically for a 10mm Stone Mastic Asphalt, both the bitumen content and filler content are each about 5% of the total mass of the mixture. Therefore, the ratio of bitumen to filler in a typical SMA specimen would be 1:1. This material will be used in the experiment designed to test the effect of pore water pressure, to be discussed in later chapters.

3.3 Mixing and compaction

The procedures chosen in producing the asphalt mixtures, in terms of laboratory mixing and compaction by roller compactor, conform to BS EN 12697-35: 2004 and BS EN 12697-33: 2003 respectively. The aggregates, bitumen and filler are uniformly mixed and the temperature before compaction is about 180°C. This is shown in figure 40.

Figure 40. Aggregates and binder mixing

The hot mixture is then poured into the pre-heated square mould (305 mm by 305 mm) and compacted to a slab thickness of 50 mm in order to achieve the desired 6% air void content. The resulting slab is shown in figure 41:

Figure 41. Resulting Asphalt slab in 305 x 305mm mould

The chosen slab thickness is 50mm even though the desired sample thickness is 30mm. 10mm is cut off from the top and bottom of the sample to reduce any potential variations in air voids across the sample's height/thickness.

3.4 Detritus in cores experiment

This section of the methodology covers the specimen preparation, the process of sieving and the image acquisition method for this experiment.

3.4.1 Specimen cutting and preparation

Cracked highway cores are the type of specimen used in the Detritus in ores Experiment. To obtain slices, these cores are surrounded by ice or epoxy resin, placed under the saw cutter and 10mm or 20mm slices taken from the cores. This is shown in figure 42 and 43.

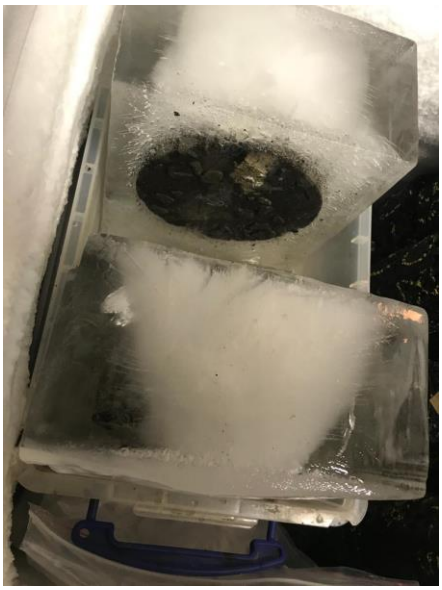

Figure 42. Cores frozen in ice

Even though it would mean more exposure of the ice or resin to heat generated from the friction of the cutting blade, 10mm thin slices were chosen firstly for imaging purposes. By nature of the image analysis method, it is only possible to take images of the top and bottom face of the slice. Therefore, if 30mm thick slices were chosen for example, there would be only 2 sets of data describing the nature of the crack at the top and bottom of a 30mm surface course layer, whereas with 10mm thin slices, there are 6 data sets. Furthermore, 10mm is the smallest thickness that can be cut.

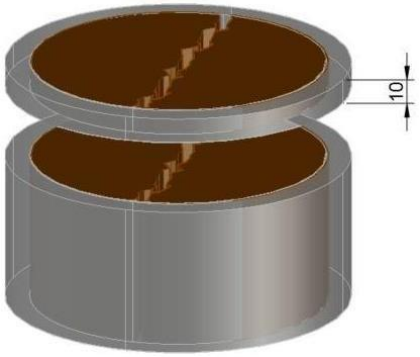

Figure 43. Cutting diagram for cores immersed in ice or cured resin

3.4.2 Sieving

The novelty of the research is to look at the effect the presence of detritus has on the development of crack dimensions. Therefore, knowing the particle size distribution of detritus, and hence sieving, is an important part of the methodology. In the experiment proving the existence of detritus in the road, detritus recovered from existing road cores will require sieving. Also, in all the other experiments, grain sizes of detritus may be an independent or controlled variable. Therefore, discrete grain sizes e.g., 0.5mm will need to be isolated from the larger mass of aggregates using sieves. The sieve sizes used are 4.000mm, 2.000mm, 1.000mm, 0.500mm, 0.250mm, 0.125mm, 0.063mm and a pan underneath. All detritus is placed in the sieves and shaken for 5 minutes, after which the grammage of detritus remaining on each sieve is brushed off, dried, and measured on a scale.

3.4.3 Image Acquisition method

The Leica M125 C is the optical microscope used in the image capture of data for the experiment proving the existence of detritus in the crack. The Leica M125 C stereo microscope offers high end quality images at a range of different optical properties. It therefore had to be set at a certain configuration to suit the purpose of the study. When these are set and the image is captured, there is a scale showing 5 mm on each image. This is used for calibration when it comes to image analysis. This is shown in figure 44.

Figure 44. Image of Leica M125C

3.5 Freeze thaw cycle experiment

This section of the methodology covers the specimen preparation and the image acquisition method for this experiment.

3.5.1 Specimen cutting and preparation

Rectangular samples notched by a cutter are the type of specimen used in the Freeze thaw cycle experiment. The rectangular samples will be made by placing slabs under a saw blade cutter which cuts under running water to prevent dust build up in the air. The width of the notch was determined by the width of the cutting blade. The height of the sample is chosen to be 30mm because this is typically the thickness of a surface course layer on UK roads. The breadth of the sample was also set at 30mm for simplicity in choosing a sample face to notch. If the sample is a square prism, it allows for any of the 4 long faces of the sample to be chosen as the face the notch will be made in. The length of the sample is chosen to be 150mm for two reasons.

1. Firstly, the ASTM recommendation for a single edged notched beam specimen in three-point bending is that the length between two load points should be 4 times the height of the specimen. Therefore, that sets the lower limit of the length at 120mm.
2. Secondly, if the square mould is 305 x 305mm, the researcher can obtain about 10 samples if the length is set at 300mm or about 20 samples if the length is set at 150mm. To obtain more samples per slab, while satisfying the single edged notched beam specimen recommendation, the researcher opted for a 150mm long rectangular beam.

Figure 45. Image of rectangular specimen

After cutting, all samples are painted over with white aerosol paint and allowed to dry. The samples are painted in order to create sufficient contrast for image analysis between the crack showing the specimen's interior (which is black) and the surface (which is white).

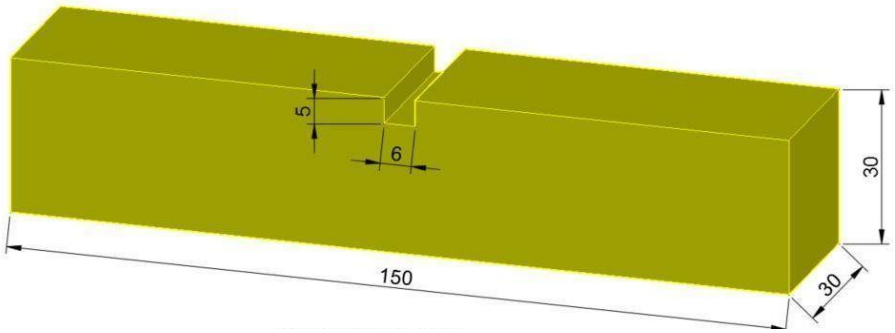

Figure 46. Rectangular specimen cutting diagram with dimensions.

3.5.2 Image acquisition method

The Leica M125 C discussed in section 3.4.3 is the optical microscope used in the image capture of data for the Freeze thaw cycle experiment.

3.6 Three-point Bending Experiment

This section of the methodology covers the specimen preparation, the testing machine, and the image acquisition method for this experiment.

3.6.1 Specimen cutting and preparation

Rectangular samples notched by a cutter (as discussed in section 3.5.1) are the type of specimen used in the Three-point bending experiment.

3.6.2 Testing Machine

One testing machine used in the project is the Nottingham Asphalt Tester (NAT). This machine was used in the experiments testing the effect of tyre loading on crack propagation. The NAT is essentially a pneumatic pressure loading system with an actuator, encased in a conditioning cabinet. It can be calibrated by its software to a variety of loads and loading regimes, depending on the experiment to be carried out. Built into the actuator is an LVDT for detecting vertical displacement and a load cell. The limits of the actuator are around 30mm vertical displacement and 10 kN load. The temperature can also be calibrated before testing across a reasonable range of values (5 - 45°C). The uniqueness of each test is in the setup beneath the actuator, e.g. indirect tensile tests, three-point bending, etc.. The researcher intends to manufacture novel testing rigs to be used in the NAT, under the influence of the actuator. An image of the NAT is shown in figure 47.

Figure 47. NAT machine

3.6.3 Image Acquisition method

The Canon EOS 200D DSLR camera is the optical device used in the image capture of data for the experiment evaluating the effect of tyre loading on top-down cracking. The 24.1-megapixel DSLR Camera is placed on a stand, in frontof the bespoke rig designed for the testing of top-down cracking, to measure crack profiles and dimensions. For calibration, a mensurated ruler is placed in the camera's field of view. In order to obtain a close-up view of the crack profile, the camera was set to a 5x magnification for all tests. This is shown in figure 48.

Figure 48. Canon EOS 200D DSLR camera

3.7 Hydraulic Fracturing Experiment

This section of the methodology covers the specimen preparation and the testing machine for this experiment.

3.7.1 Specimen preparation

Circular samples made by pouring 50% asphalt filler blend mastics into a mould are used in this test. These samples are chosen because they require no compaction or cutting, which is necessary for the bespoke mould because the material is poured around a hollow syringe. Secondly, filler blend mastics represent a material often used to fill pre-existing cracks in the road. This is shown in figure 49.

Figure 49. Solid Circular sample in bespoke mould

3.7.2 Testing Machine

The Second testing machine used by the researcher is called the MAND. Unlike the NAT tester, it is a hydraulic pressure loading system with a more powerful actuator with more range. The limits of the actuator are around 100mm vertical displacement and about 50 kN load. This machine is used in investigating the effect of pore water pressure on an asphalt pavement. The only disadvantage to this testing rig is the absence of temperature control. This is shown figure 50.

Figure 50. MAND Machine

3.8 Storage

The cored and cut specimens are then stored in a cold room on one of their flat faces for up to two weeks from compaction in dry atmosphere at 5°C. Specimens are only removed from this controlled environment to be conditioned and tested at the required temperature. Conditioning cabinets are also used for storage. These are useful, because they provide a range of temperatures to store the samples at, as opposed to the fixed 5°C cold room temperature. However, conditioning cabinets are used for shorter term storage i.e., days before testing.

3.9 Novel experimental equipment manufacture

As earlier mentioned, although potholes are a perennial problem in UK roads, the mechanisms of their formation are poorly understood. As a result, there is no established experimental method to investigate the phenomena related to potholes. Therefore, one of the objectives of the research is to attempt to develop some experimental framework with which to study pothole formation. Because of this, novel apparatus was required. The process of novel equipment manufacture underwent three main stages:

1. Concept design
2. Material assignment
3. Dimensioning, sourcing, and costing

3.9.1 Concept design

The first stage of the equipment manufacture is the initial conception of the ideas. This is carried out in the AutoDesk AutoCAD software. The 3D elements of the rigs are created and assigned to individual layers. Any potential changes to the dimensions, shape, form, or transparency of any design element also takes place at this stage after deliberation. Once completed, the concept is made more concrete as it is easier to visualise, and the 3D model is ready to move to the second stage of equipment manufacture. This is shown in figure 51.

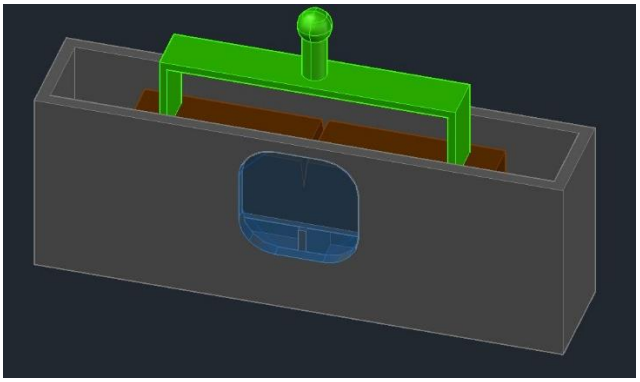

Figure 51. Conceptual model of three-point bending rig

3.9.2 Material assignment

In this stage, every 3D polygon is assigned a material type with associated material properties. This is carried out in the AutoDesk INVENTOR software and is interoperable with AutoCAD. To import the 3D AutoCAD model into INVENTOR, each layer may be imported, and assigned its material type e.g. aluminium, polycarbonate, etc. This is done until all layers are imported and assigned. An image of this model is shown in figure 52.

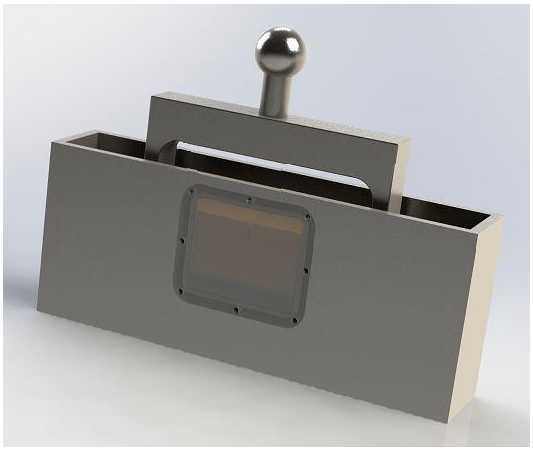

Figure 52. AutoDesk INVENTOR Model of three-point bending rig

3.9.3 Dimensioning, sourcing, and costing

Once the AutoDesk INVENTOR 3D model is complete, it is then ready for the final stage of the equipment manufacture. Here, the elements can be dimensioned, the total quantity of different materials necessary for the manufacture is known and can be sourced and ordered, and a final budget for the manufacture can be made. The cost of all manufactured equipment for this project stands at over £2500.

4 Detritus in Cores Experiment

4.1 Introduction

In the earlier chapters, it has been hypothesized that one peculiarity that makes the winter months potentially more conducive for accelerated crack propagation and hence pothole formation is the presence of detritus on the road surface. This is because, it is reasonably assumed that by the transport of precipitation or meltwater, this detritus is deposited within the cracks in the road and remains there even after the suspension it was carried in has evaporated off. Once present in the crack, it is then further hypothesised that the detritus being relatively incompressible, prevents crack closure thereby indirectly accelerating crack growth further into the pavement. The experiments carried out in this chapter are to firstly prove this fundamental premise: whether dirt is ever deposited in the crack to begin with. Secondly, to know typical crack dimensions (width with changing depth) that practically occur in existing roads. Lastly, the results of this study will have integrated in them some applied hydraulic fracturing concepts, considering the detritus as proppants as discussed in the literature review.

4.2 Modelling

As discussed in the literature review, there are three elements of hydraulic fracturing models in this research: crack propagation, fracture opening width and lastly proppant concentration & volume. This chapter will consider the last two terms, expanding on and applying the equations used to characterise them. In hydraulic fracturing, a crack is measured by its length, because it travels horizontally or perpendicular to gravity. In this research on pavement engineering, a crack is measured by its depth, because the cracks of interest to the researcher travel vertically in the direction of gravity. When hydraulic fracturing models are applied to asphalt in this research, crack length and crack depth are analogous.

4.2.1 Fracture opening width

$$w(x) = \frac{K\prime}{E\prime} x^{1/2} - \frac{4}{\pi E\prime} \int_0^{\infty} F(x,s) \frac{dp(s)}{ds} ds, \quad \text{Equation 21}$$

$where\ x = crack\ length.\ This\ is\ from\ Equation\ 15.$

$$but\ \frac{dp(s)}{ds} = 0\ (no\ flow) \quad \text{Equation 22}$$

$$w(x) = \frac{K\prime}{E\prime} x^{1/2} - \frac{4}{\pi E'} \int_0^{\infty} 0\ ds \quad \text{Equation 23}$$

$$w(x) = A\frac{K\prime}{E\prime} x^{1/2} - \frac{4}{\pi E'} C\ , \quad \text{Equation 24}$$

$where\ C\ is\ 0, \quad and \quad A\ is\ a\ fitting\ constant$

With the crack width measurements obtained for each slice, a graph showing the relationship between crack width and the square root of the crack length can be drawn with the gradient being $A\frac{K\prime}{E\prime}$.

4.2.2 Proppant concentration

When equation 17 is simplified, it gives:

$$B\left(\frac{w}{a}\right)\hat{Q}^{(p)}\left(\bar{\phi},\frac{w}{a}\right)\left(V + 2C'^{\frac{\sqrt{Vz}}{w}}\right) - V\bar{\phi}(w(z),z) = 0 \quad \text{Equation 25}$$

$$no\ leak\ off,\ C' = 0, \quad \text{Equation 26}$$

$$B\left(\frac{w}{a}\right)\hat{Q}^{(p)}\left(\bar{\phi},\frac{w}{a}\right)V - V\bar{\phi}(w(z),z) = 0 \quad \text{Equation 27}$$

$$V\left(B\left(\frac{w}{a}\right)\hat{Q}^{(p)}\left(\bar{\phi},\frac{w}{a}\right) - \bar{\phi}(w(z),z)\right) = 0 \quad \text{Equation 28}$$

$$\bar{\phi}(w(z),z) = B\left(\frac{w}{a}\right)\hat{Q}^{(p)}\left(\bar{\phi},\frac{w}{a}\right) \quad \text{Equation 29}$$

Equation is 29 is the simplified form of equation 17 characterising proppant concentration, where $\bar{\phi}(w(z), z)$ is proppant concentration, N is the bridging factor and $\hat{Q}^{(p)}\left(\bar{\phi}, \frac{w}{a}\right)$ is the normalised proppant flux coefficient.

The proppant flux coefficient is a dimensionless value that is multiplied by the volumetric flow of a slurry in order to obtain the volumetric flow of the proppant within the slurry, provided there is no bridging. The bridging factor (N) is defined as the number of particles of a given grain size necessary to form a bridge over a crack of a given width. This is shown in equation 30:

$$B = \begin{cases} 1, & w > w_B = 2a(N+1) \\ 0, & w < 2aN \end{cases} \qquad \text{Equation 30}$$

The proppant concentration varies with corresponding changes in crack width, crack depth as well as particle size. In the hydraulic fracture model, the proppants are all the same radius which is not the case in the asphalt problem. Therefore, the concentration of each grain size present in the detritus slurry will be evaluated for particles of size: 6.3mm, 4.0mm, 2.8mm, 2.0mm, 1.0mm, 0.5mm, 0.25mm, 0.125mm, 0.063mm & pan.

4.2.3 Proppant volume Equation

The volume of proppant caught in the crack is the sum of all the volume fractions for each depth.

$$V_P = \int_{x_0}^{x_1} w(x)\phi_m\bar{\phi}(z)\, dz, \qquad \text{Equation 31}$$

Where x_0 is the point along the depth of the sample at which bridging occurs and x_1 is the point along the depth of the sample where proppant exists.

4.3 Experiments

The specimens used in this experiment are asphalt cores of 150mm in diameter and of varying depths. These cores were sourced from AECOM, a prominent engineering consultancy in the UK. These specimens were cored

out of existing road surfaces because they were cracked or damaged and AECOM were tasked with the diagnostics of the observed pavement failure. For data protection purposes, the origins of the various cores and information about the asphalt mix designs have not been disclosed by the engineering consultancy. Nevertheless, these asphalt cores will provide a reasonable starting point to understand the nature of cracks observed in road surfaces across the UK.

4.3.1 Resin core preparation

One of the objectives of this test is to first have some understanding of typical crack widths observed in the road at varying depths. Secondly is to also understand how much dirt is caught in these cracks, relative to the total crack volume. Therefore, to do this, images of core slices need to be obtained somehow. One potential approach considered by other researchers is to use non-destructive x-ray imaging to obtain these images. However, there may not be sufficient contrast between the asphalt matrix and detritus caught in the crack to differentiate them. The researcher therefore adopted the use of optical microscopy, using the following steps:

4.3.1.1 Sample preparation

A core with a deep crack (greater than 30mm depth) is taken and placed in a cylindrical tin. An epoxy resin is then prepared and poured into the cylindrical tin until the asphalt core is submerged in the resin. The cylindrical tin is then placed in a vacuum chamber and covered with its lid. The chamber is then connected to a pump which sucks the air out of the core's pores and thereby sucks the resin into the core. This is done for 30 minutes. The core is then allowed to sit until the resin cures after 24 hours, as shown in figure 53.

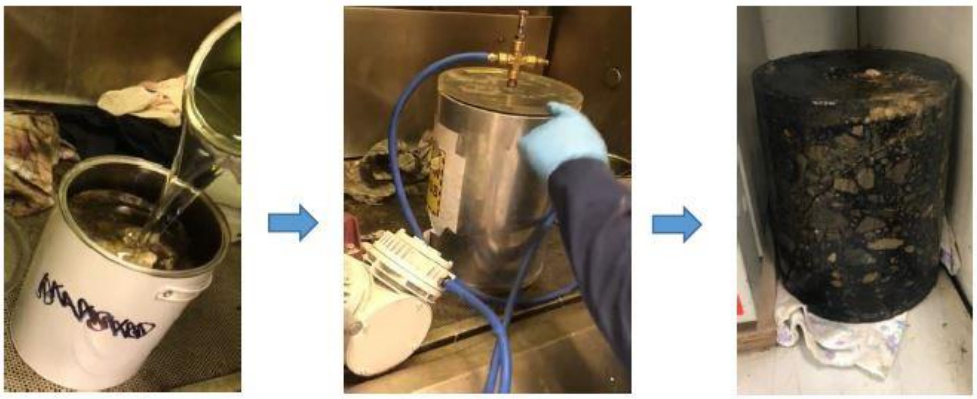

Figure 53. Schematic of resin core preparation

4.3.1.2 Cutting

The core must then be taken out of the tin and kept at low temperatures in preparation for cutting. The epoxy resin gives off a pungent and strong smell because the friction from the cutting blade generates heat. In the absence of a fume extractor present near the cutting rig, this process will typically be carried out for one core and for 7 slices of the core before the epoxy begins to give off a strong smell. The first two slices were 10mm thick. However, to cover more of the core's depth with the remaining five slices, a slice thickness of 20mm was then adopted. This is shown in figure 54.

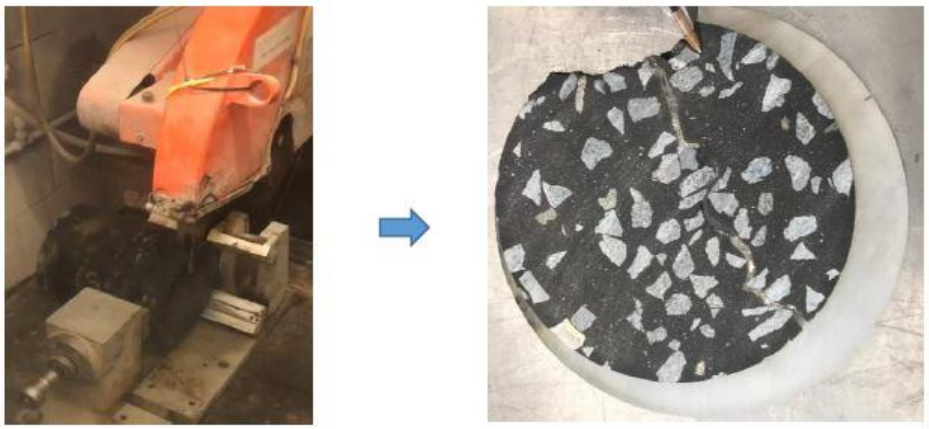

Figure 54. Image of cutting process and resulting slice

4.3.1.3 Measurement

These slices are now placed under an optical microscope and images of the full length of the crack are taken, for both sides of each slice. Once the scale is set in the image analysis software, there are three measurements made for every side of every slice:

- 100 width measurements across the length of the crack
- Area measurements of crack
- Area measurements of portions of crack filled with detritus.

This procedure was carried out for only 1 core.

4.3.2 Ice core preparation

The third motivation behind this test is to quantify the gradation of detritus trapped in the cracks. To accomplish this, a core must be cut into slices without disturbing the contents of the cracks, or without splitting or damaging the slices. Resin could be seen as a potential solution, however, there are no means of extracting the detritus from the resin. Therefore, water was adopted in this case, using the following steps:

4.3.2.1 Sample preparation

A core is placed in a cuboid container and filled with water. It is placed in a freezer at -20°C for 24 hours. When frozen, the contents of the cuboid container should be emptied. At this point, the ice block may now be taken to cutting for the first stage of cutting.

4.3.2.2 Cutting

The core is first cut to blocks of dimensions 60mm x 60mm x the depth of the core. This first cutting stage is done so that the block is easier to handle in the second and final stage of cutting but also to ensure there is sufficient ice

surrounding the core slice to hold it together after cutting and to withstand the heat generated when cutting without significant melting. The blocks are then placed back in the freezer to cool for another 24 hours. In the second stage of cutting, 4 x 10mm slices are cut from the top of the core and stored in a freezer. An image of this is shown in figure 55.

Figure 55. Ice core in cutting rig

4.3.2.3 Detritus Extraction

To extract the detritus, a bucket is placed in a sink and on top of the tap, a mesh tray is placed over the bucket, and the slice is placed on the mesh tray. Passing running water over the ice-covered slice till the ice thaws causes the slice to split along the crack. The running water collects in the bucket underneath. The running water continues to pass over the crack face, washing the detritus off the surface of the crack face. Figure 56 shows this.

Figure 56. Crack face of slice showing dirt caught in cracks.

4.3.2.4 Sieving

When this is done for all slices, the mesh tray is removed off the bucket and bucket is allowed to sit for some hours. This will allow the detritus washed into it to set to the bottom of the bucket. Then, the contents of the bucket was poured through a sieve lined with filter paper till all the detritus was sieved off from the water, as shown in figure 57.

Figure 57. Detritus caught in cracks on filter paper in funnel.

The sieved-off detritus is placed in an oven and the resulting gradation is measured. This process was repeated for 10 cores.

4.4 Results

4.4.1 Crack dimensions – width vs depth

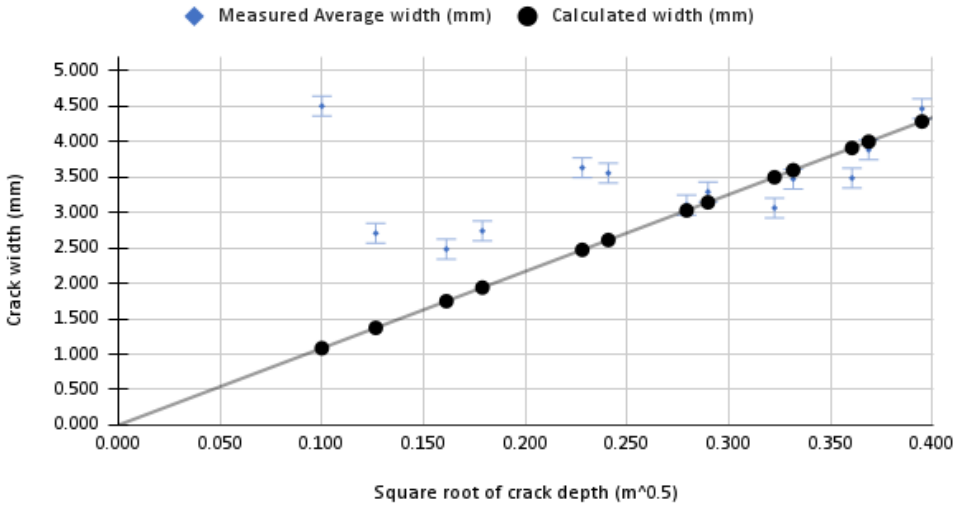

Figure 58. Graph of average crack width and the square root of crack depth

In figure 58, the average observed crack width with change in square root of crack depth is compared to the predictions of the hydraulic fracturing model, which is graphically shown in figure 36. The calculated width is obtained from Equation 24, where C = 0 and A is set at 1.5. The observed points for crack widths demonstrate a “w” shape, where the crack width decreases, then at some crack depth, begins increasing, then at another discrete crack depth decreases again, and finally starts to conform to the trend of the hydraulic fracturing model. This may imply different forms of cracking along the crack depth of the samples; where top-down cracking is the dominant failure method at the top of the sample, bottom-up cracking being the more prominent failure method at the bottom of the sample and a transition between these two mechanisms in the middle of the samples. The hydraulic fracturing model fundamentally predicts a scenario where crack width is proportional to crack depth. The predominant region of interest for the research will be the surface course, which is the region of the graph which does not conform to this proportionality. Therefore, an equation relating crack width to crack depth must still be established. It may also be helpful in gauging what range of crack widths can be expected or applied to other experiments (2.4 - 4.5mm).

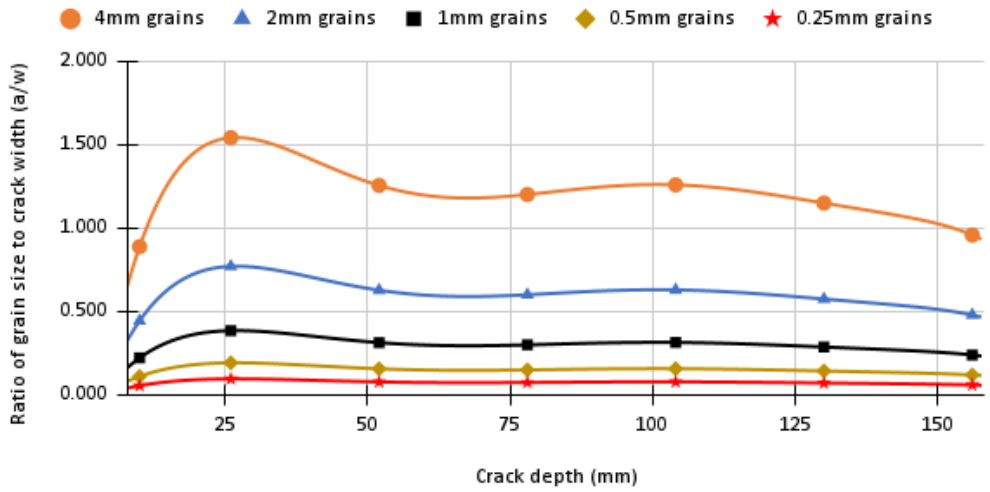

Figure 59. Graph of ratio of grain size to crack width at each depth of crack for coarse grain sizes

Figure 59 shows the various grain sizes of detritus present and these grain sizes as a fraction of the crack width corresponding to the crack depth on the x-axis. This is shown for the grain sizes of 4.00, 2.00, 1.00, 0.50, 0.25mm respectively. Values greater than 1.00 mean that the detritus grain size is greater than the crack width corresponding to a given crack depth. For example, the crack depth 26mm has a crack width of 2.482mm. Therefore, the ratio of a 4mm aggregate to the crack width at 26mm depth will be greater than 1. Figure 59 shows that the ratio of grain size to crack width increases until the crack depth crosses 30mm, at which point it plateaus and eventually decreases with increase in crack depth. The global trend of the plot demonstrates the nature of the cracks in the pavement to almost act as a sieve, filtering out grain sizes larger than their width. Even though there are some examples of larger angular aggregates existing in relatively smaller crack widths, these are rarities. An example of this is shown in figure 60.

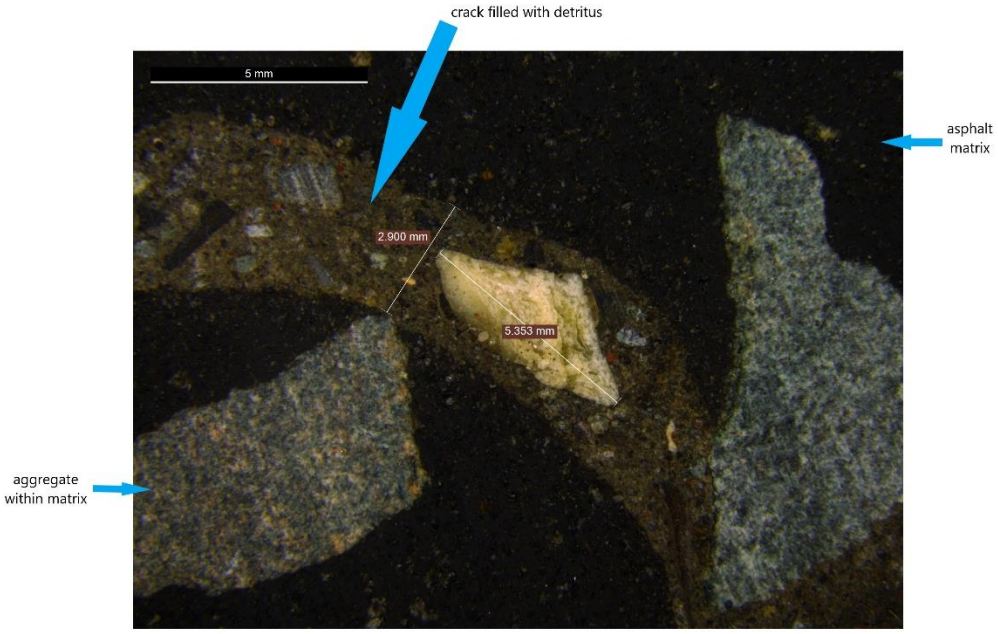

Figure 60. Image of larger angular aggregates existing in relatively smaller crack width

Another key implication of this graph is to show how susceptible each crack depth is to detritus bridging, which is the ability of two or more grains to form a bridge across the crack's width and prevent further detritus from passing through to layers beneath.

4.4.2 Bridging

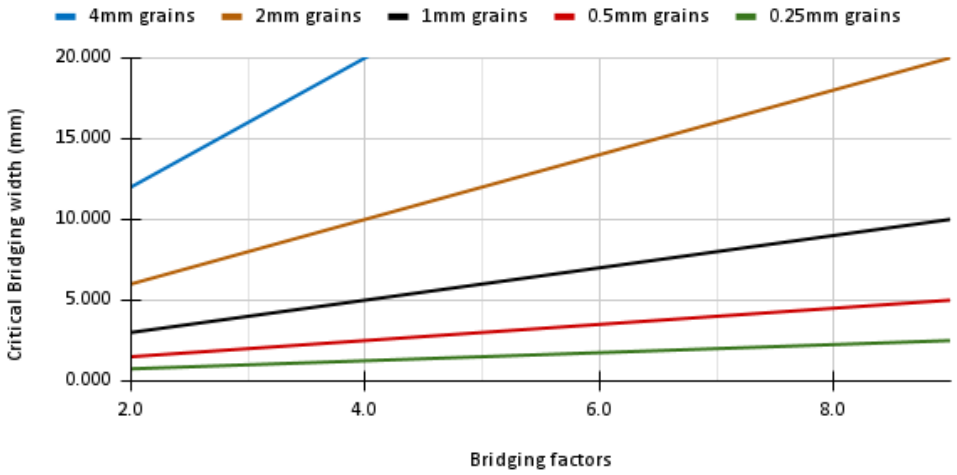

Figure 61. Graph of calculated critical bridging width to grain size for varying bridging factors

Figure 61 predicts that for the crack widths on the y-axis, it will take a

corresponding number of grains of a given grain size on the x-axis to cause bridging. This is obtained from calculations using Equation 30. As earlier mentioned, the bridging factor is defined as the number of other particles of a given grain size is needed to form a bridge over a crack of a given width. For example, if a crack grows to be 5mm wide, its width now becomes the critical bridging width necessary for 4 other particles of 1mm grain size to interlock with an existing particle of 1mm grain size to form a bridge over the crack. Seeing as the average crack widths observed are between 2.4 to 4.5mm, this shows that it is more likely for 0.25mm, 0.5mm and 1.0mm particles to form a bridge. For example, it will take only two or three 1.0mm particles aligned in a row to form a bridge across a 3-4mm crack width, compared to a 0.5mm particle which would require five to seven particles to bridge the same crack width. It must also be noted that there are no fine-grained particles represented in the graph. This is because in the hydraulic fracturing models only coarse grain particles are considered. However, there is evidence of fine grain particles bridging a crack width which is shown in figure 62.

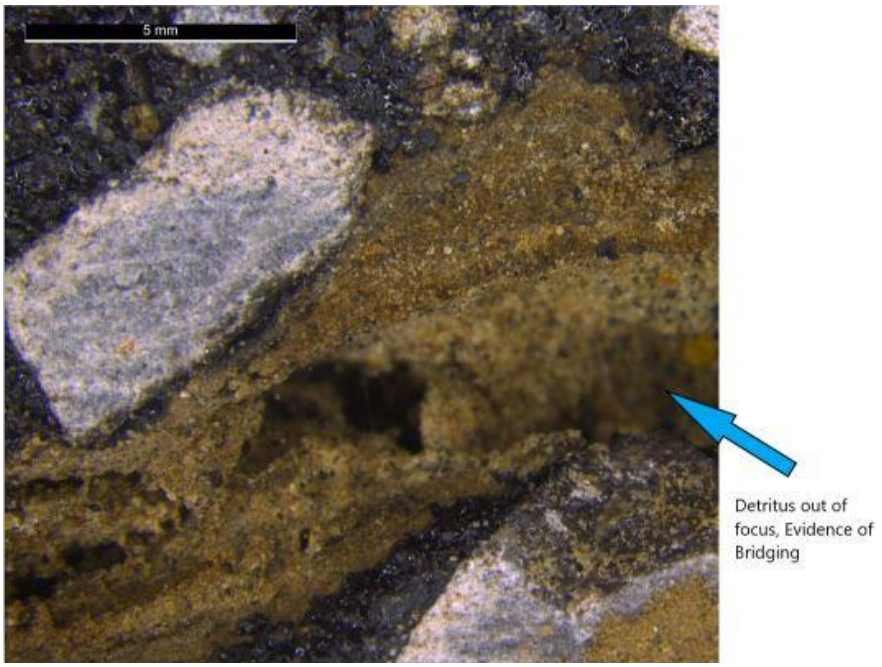

Figure 62. Image of fine grain particles bridging

Figure 62 shows a crack width with some detritus in-focus and other parts of the crack, filled with detritus out of focus. This suggests that they are at different depths which further implies that the portion of the crack with

detritus out of focus has been bridged. This occurs at 136mm depth. With bridging comes the concept of crack volume fractions filled with dirt.

4.4.3 Volume fraction

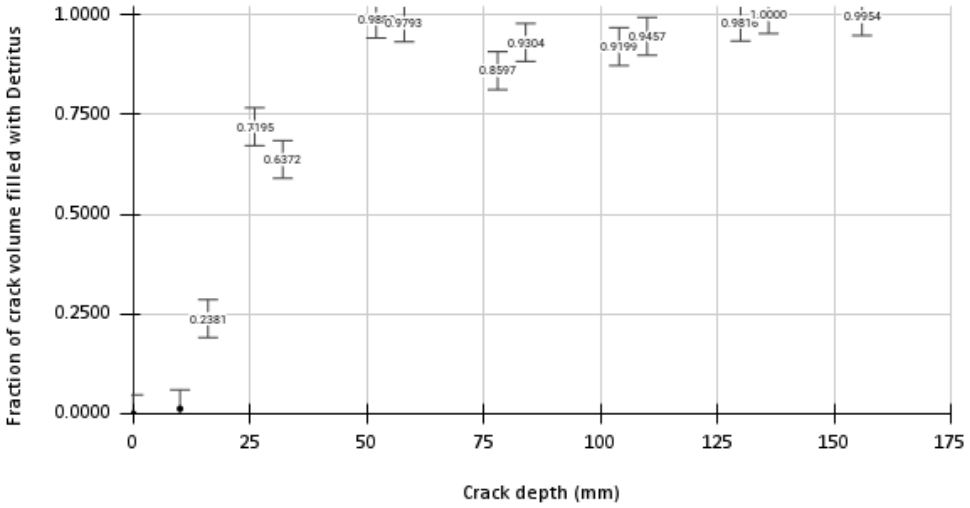

Figure 63. Graph of Volume fraction at each slice depth of crack

Figure 63 shows the fractions of the total crack volume at each crack depth that is filled with detritus. The volume fraction increases with depth until the sample is fully filled with dirt at 136mm depth. This graph seems to suggest that the detritus enters the crack from the road surface.

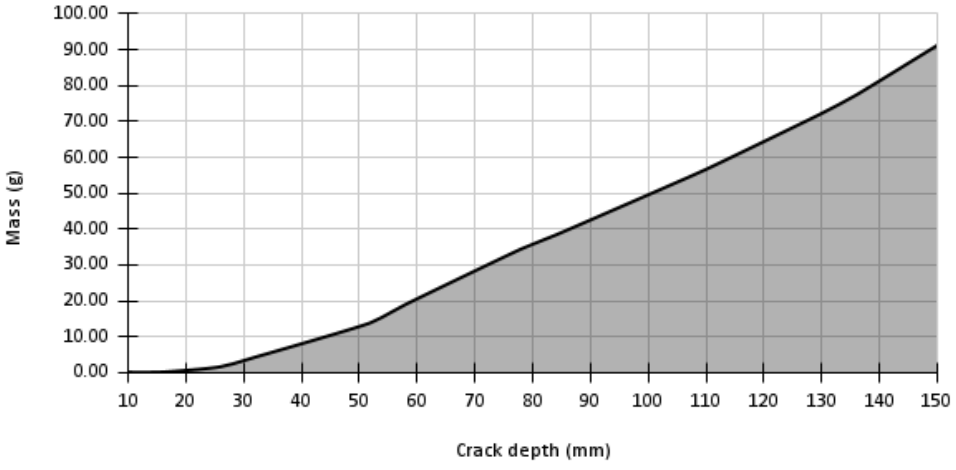

Figure 64. Graph of Calculated cumulative mass of detritus in each crack depth

Figure 64 shows the predicted mass of detritus across the crack depth. This is obtained from calculations using equation 31. The calculation is simply the product of the volume of each slice, the volume fraction for each slice and the density of the aggregate; taken to be 2.75 g/cm³. This plot again gives some indication of the mass of detritus to expect once it is extracted from the various cores. Also, it gives some indication of the mass of detritus present in each layer. For the surface course, about 4g of detritus is predicted to be present.

4.4.4 Particle distribution

A graph of particle size distribution for all grain sizes of detritus obtained, is shown in figure 65:

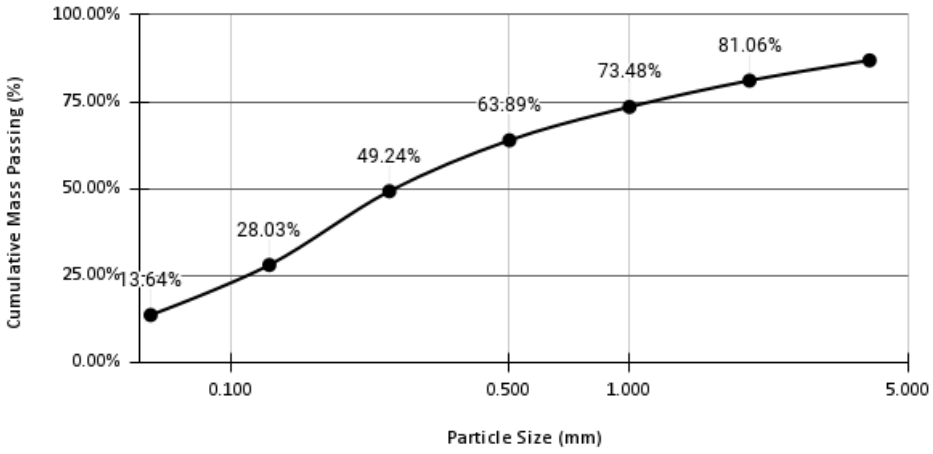

Figure 65. Particle size distribution for all grain sizes of detritus obtained.

Figure 65 shows the particle size distribution of the detritus extracted from the top 40mm depth of 10 asphalt cores. The steepest part of the distribution was between 0.25mm and 0.125mm grain size.

4.4.5 Masses of each grain size

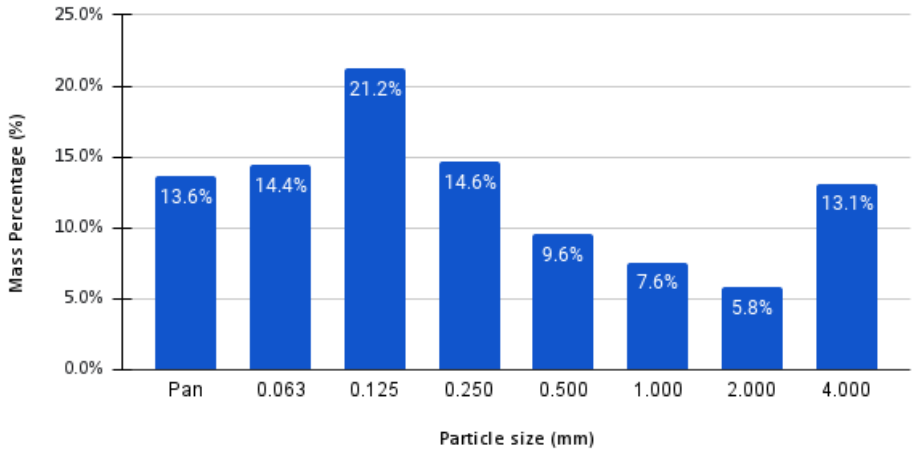

Figure 66. Graphs of percentage masses of particles from all samples to grain sizes

Figure 66 shows percentage masses of detritus obtained for all grain sizes. Across the 10 samples, 39.6g of detritus was extracted from them. This implies that there was on average 3.96g of detritus extracted from each core, which is relatively consistent with the prediction of the calculated cumulative mass of detritus of 4g in the first 32mm of sample depth. Out of this mass of 39.6g however, the detritus which has the highest percentage and therefore occurred the most was 0.125mm, which is a fine-grained aggregate. The least occurring grain size was 2.00mm which is a coarse-grained aggregate. Summing up all coarse grain aggregates, they add up to 50.7%, with the remaining 49.3% being fine grained aggregates. This is a significant result, because the element of detritus responsible for the prevention of crack closure is largely the coarse-grained particles. This means that on average 2g of detritus is involved in the hypothesised ratchet mechanism in each core. Secondly, the result of the percentage masses is significant because it gives some insight to how the detritus is introduced into the crack. From qualitative observations it appears that there are some particles that are washed in by meltwater or precipitation, which would typically be the fine-grained particles because they are more easily transported by water in suspension. Conversely there are also other particles which once seemed part of the asphalt matrix but were stripped of bitumen and fell into the

crack. These are the coarser grained.

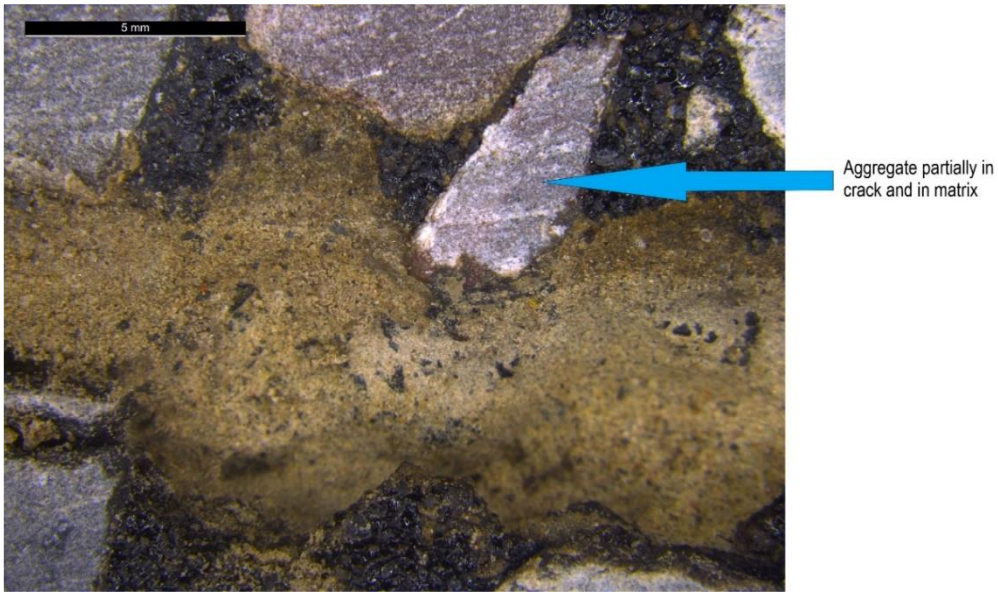

Figure 67. Coarse grain aggregate partially in crack

Figure 67 shows an aggregate partially in the crack and also partially in the matrix. Such a stone is likely to be stripped of bitumen and eventually fall into the crack. Upon interrogation of this qualitative data, the researcher was uncertain as to the extent of these two phenomena. Figure 66 does not fully quantify this, but it however gives more insight as to the degree to which dirt is being washed in or aggregates already in the matrix are stripped.

4.5 Summary

1. The crack widths observed are within the ranges of 2.7- 4.5mm. This will inform the choice of crack width in the Freeze Thaw experiment
2. The hydraulic fracturing model only predicts crack width and crack length proportionality. Therefore, there is still a need to establish a relationship between crack width and crack length within the surface course where the relationship between the two quantities is inversely proportional.
3. Volume fraction measurements are around 70% in the surface course and reach 100% at 136mm depth. This is the depth therefore at which bridging is observable.

4. The ratio of a particle size to crack widths for each crack depth shows the likelihood of that particle entering that crack or bridging it.
5. For bridging cracks widths of 2.7 - 4.5mm, the most plausible grain sizes to achieve this are 1mm, 0.5mm and 0.25mm grain sizes.
6. 51% of detritus is coarse grained and 49% of detritus is fine grained. 40g of dirt obtained from 10 samples suggests that 4g of detritus exists in one sample.

5 Freeze Thaw Cycling experiment

5.1 Introduction

Arguably, the most important peculiarity of the winter months, that makes roads more susceptible to pothole formation relative to any other time of the year, is the high occurrence of frost days and freeze thaw cycles. The cycling in temperature above and below freezing triggers thermal expansion and contraction of asphalt. Also, relatively lower average temperatures mean that asphalt behaves in a more brittle manner and is more likely to crack than to rut and flow. Moreover, there is precipitation trapped in the pores of the pavement that undergoes a phase change. When the pore water becomes ice at sub-zero temperatures, its volume expands by 9%, pushing against the surrounding asphalt matrix. With all these thermo-mechanical processes happening, there is also the effect of the detritus which the meltwater may wash into the road cracks, and which may prevent crack closure. The experiments in this chapter are intended to simulate most of these processes and the effect of detritus on the evolution of crack widths after significant temperature cycling. Because of the uniqueness of the study, equipment tailor-made to the experiment has been developed to provide some framework for the effective investigation of the hypothesis and the extent to which a robust methodology has been achieved will be discussed.

5.2 Modelling

There are fundamentally five phenomena which will be modelled in the freeze thaw cycle: thermal expansion, thermal contraction, volumetric expansion of ice, isothermal creep flow and prevention of crack closure by detritus. These actions will be divided into the two phases: either in freezing where crack width increases or in thawing where the width decreases.

$T = Temperature$

$C = Contraction$

$E = Expansion$

$H = Height\ of\ the\ sample$

$\mathrm{B} = breadth\ of\ the\ sample$

$w_0 = Initial\ crack\ width$

$L_{Specimen} = Initial\ length\ of\ specimen\ before\ pre\text{-}cracking$

$\varepsilon_T = Thermal\ strain\ of\ asphalt,$

$\Delta w_v = Volumetric\ expansion\ of\ ice,$

$\Delta w_D = Detritus\ width\ change$

$\Delta w_{IAF} = Isothermal\ asphalt\ flow,$

The formulae for crack width change due to freezing are:

$$\Delta w_{Freeze} = \left(\varepsilon_{TC} \times L_{Specimen}\right) + \Delta w_v \qquad \text{Equation 32}$$

$$\varepsilon_{TC} = \int_{T_1}^{T_2} \alpha_C(T)\, dT \qquad \text{Equation 33}$$

$$\alpha_C(T) = 25\mu m/m/^{\circ}\mathrm{C}$$

$$T_1 = -10^{\circ}\mathrm{C} \qquad \& \qquad T_2 = 20^{\circ}\mathrm{C}$$

$$\varepsilon_{TC} = \int_{-10^{\circ}\mathrm{C}}^{20^{\circ}\mathrm{C}} \alpha_C(T)\ dT \qquad \text{Equation 34}$$

$$\varepsilon_{TC} = 30^{\circ}\mathrm{C} \times \alpha_C \qquad \text{Equation 35}$$

$$\Delta w_v = \frac{1.09}{HB}\left[\left(HB \times \left(L_{specimen} \int_{0^{\circ}\mathrm{C}}^{20^{\circ}\mathrm{C}} \alpha_C(T)\, dT\right)\right) - V_D\right] \qquad \text{Equation 36}$$

$$\Delta w_{Freeze} = \left(30^{\circ}\mathrm{C} \times \alpha_C \times L_{Specimen}\right) + \Delta w_v \qquad \text{Equation 37}$$

The formulae for crack width change due to Thawing are:

$$\Delta w_{Thaw} = \left(\varepsilon_{TE} \times L_{Specimen}\right) + \Delta w_D + \Delta \mathrm{w}_{\mathrm{IAF}} \quad \text{Equation 38}$$

$$\varepsilon_{TE} = \int_{T_1}^{T_2} \alpha_E(T)\, dT \quad \text{Equation 39}$$

$$\alpha_E(T) = 25\mu m/m/^{\circ}\mathrm{C}$$

$$T_1 = -10^{\circ}\mathrm{C} \qquad \& \qquad T_2 = 20^{\circ}\mathrm{C}$$

$$\varepsilon_{TE} = 10^{-5} \times \int_{T_1}^{T_2} \alpha_E(T)\ dT \quad \text{Equation 40}$$

$$\varepsilon_{TE} = 30^{\circ}\mathrm{C} \times \alpha_E \quad \text{Equation 41}$$

$$\Delta w_{Thaw} = \left(-30^{\circ}\mathrm{C} \times \alpha_E \times L_{Specimen}\right) - \Delta \mathrm{w}_{\mathrm{IAF}} + \Delta w_D \quad \text{Equation 42}$$

where $\Delta \mathrm{w}_{\mathrm{IAF}}$ *and* Δw_D *are terms determined by experimental data*

The global model for Crack width is therefore:

$$w_n = w_0 + J \cdot \left(\frac{2n+\left(1+(-1)^{n-1}\right)}{4}\right) \Delta w_{Freeze} + K \cdot \left(\frac{2n-\left(1+(-1)^{n-1}\right)}{4}\right) \Delta w_{Thaw}$$

Equation 43

where $n, \qquad 0 \leq n \leq 13$

where J *and* K *are constants for graph fitting*

5.3 Experiment

The experiments testing the effect of detritus on a road under freeze thaw cycles is the focus of this chapter. This experiment will not consider the propagation of cracks, but the response of crack width to the presence of detritus. Also, there are generally four cases that will be tested:

1. the dry case (without dirt or water),
2. the water without dirt case,
3. the dirt without water case and
4. the dirt and water case.

Each case corresponds to a real-life scenario, especially the dirt without water case which is in the event that the meltwater or precipitation evaporates off or percolates deeper into the pavement, leaving the dry detritus within the crack. Moreover, considering the various crack widths observed in the previous experiment, an initial crack width of about 2.75 mm is chosen. This seems to be the typical crack width obtained for slices in the surface course. Because crack growth is not the focus of this experiment, the sample is cracked all the way through its 30mm height. Furthermore, 1g of detritus at a grain size of 0.5mm was chosen for the experiment as representative of coarse aggregates capable of preventing crack closure. The temperature difference of 30°C ranging from 20°C to -10°C was chosen because it still puts the asphalt samples in the region of visco-elastic behaviour. The upper limit of this range is chosen because it is the standard temperature for UK climate. The lower limit was chosen firstly because it was the lowest temperature the conditioning cabinet used could achieve. Secondly, it was a temperature high enough that the freezing point that did not place the asphalt sample within reach of the glass transition temperature. Minimum temperatures significantly below the glass transition temperature (e.g. -25°C) would be considerable enough to induce low temperature cracking. However, such low temperature conditions generally would not be observed on UK pavements.

5.3.1 Bespoke equipment parts

As earlier mentioned, the uniqueness of the test requires equally unique testing equipment. Below is an overview of the bespoke equipment as shown in figure 68 and 69 and the relevance of each part and rationale behind the choice of configuration, material and dimensioning.

Figure 68. Image of Freeze Thaw rig

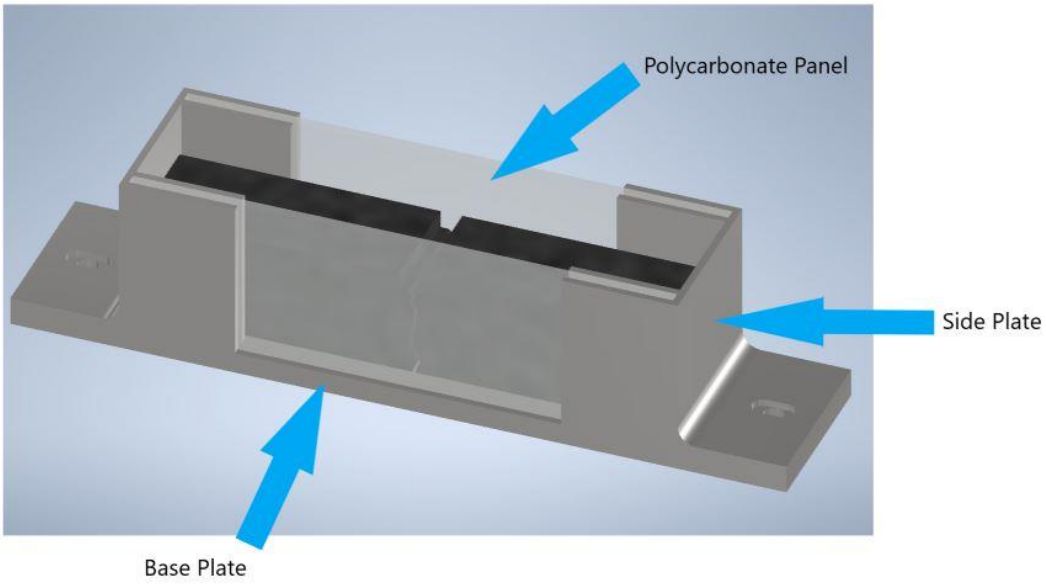

Figure 69. Image of 3D rendering of Freeze Thaw rig

1. **Base plate:** The base plate is the unit on which the two halves of the sample rest, as well as the polycarbonate panels and the side plates. Therefore, the widths of all these elements were factored into the determination of the base plate width. It is also made of aluminium, for ease of sourcing even though it has the tendency to corrode in contact with water. The side plates are fastened by screws onto the base plate, hence the holes at the ends.

2. **Side plates:** These are the units that hold the sample. Each half of the sample is glued to the side plate by high strength araldite. The side plates have an inner dimension of about 31mm to accommodate a 30mm wide sample. The side plates also have a slit for housing the polycarbonate panels. The position of side plates determines the initial crack width of the sample. Therefore, the hole through which a bolt is placed, is shaped as an oval to allow for some variability in crack width (0.5mm - 4mm).

3. **Polycarbonate panels:** These are on the sides of the sample and are held in place by the side plates. They permit the researcher to look at the water level when the sample is tested under the water case and to view whether the detritus has filled the crack along the specimen's height. The polycarbonate panels are also to help ensure that the detritus is held in place in the crack and is not washed out by the presence of water.

5.3.2 Sample preparation

In order to prepare the sample for the test, it must first be painted with white aerosol paint on every side and allowed to dry. Once this is done, it must then be fully cracked. A typical three-point bending test can ensure that. After this, each half of the specimen must be smeared with a high strength araldite and glued to the side plates and left for 24 hours for the araldite to harden. Then, the sample is ready for testing.

5.3.3 Test

Once the sample is prepared, the test can be run. The samples used for the test are 10mm Stone Mastic Asphalt samples with dimensions 150 x 30 x 30mm as earlier described in the methodology chapter. The sample is to undergo 24 hours of freezing in a conditioning cabinet at -20^{o}C and 24 hours of thawing at 10^{o}C. After each set of 24 hours, the sample is placed under an optical microscope and images of the top of the sample are taken. This is done for 14 days: 7 days of freezing and thawing each.

5.3.4 Image analysis

Once the images are taken, set to scale, and aligned, the greyscale value of each pixel must be plotted to obtain a profile. The surface of the sample painted white will have a high greyscale value, and the crack being inherently black will have a low greyscale value. The change in greyscale profiles across images taken on different days is what is measured as the change in crack width over time. Figure 70 shows a crack and a rectangle marking the region of interest (ROI). The grey values for the ROI are then plotted along the length of the rectangle to obtain the profile.

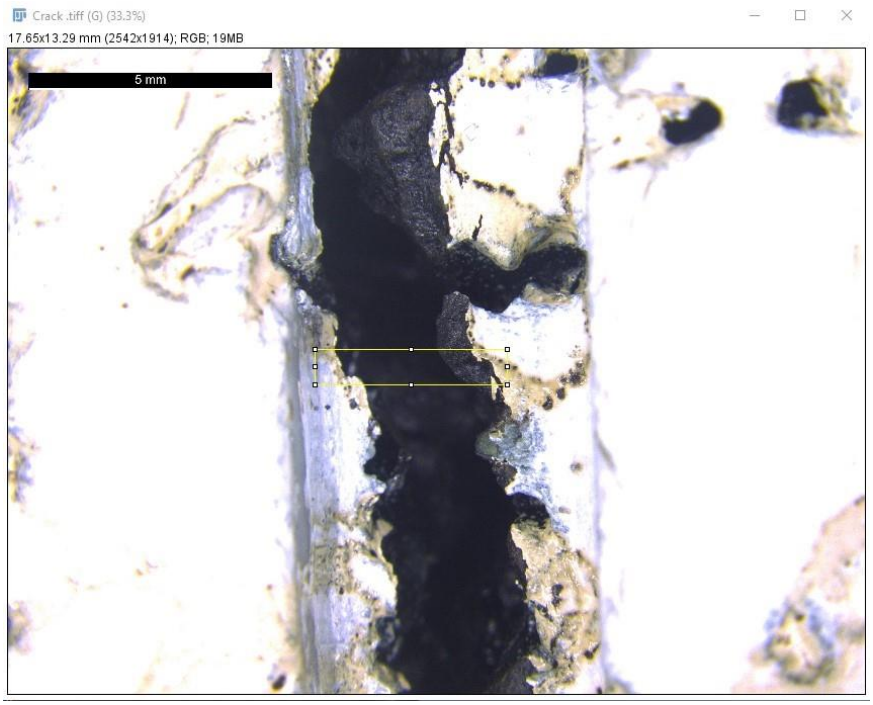

Figure 70. Image of crack showing ROI

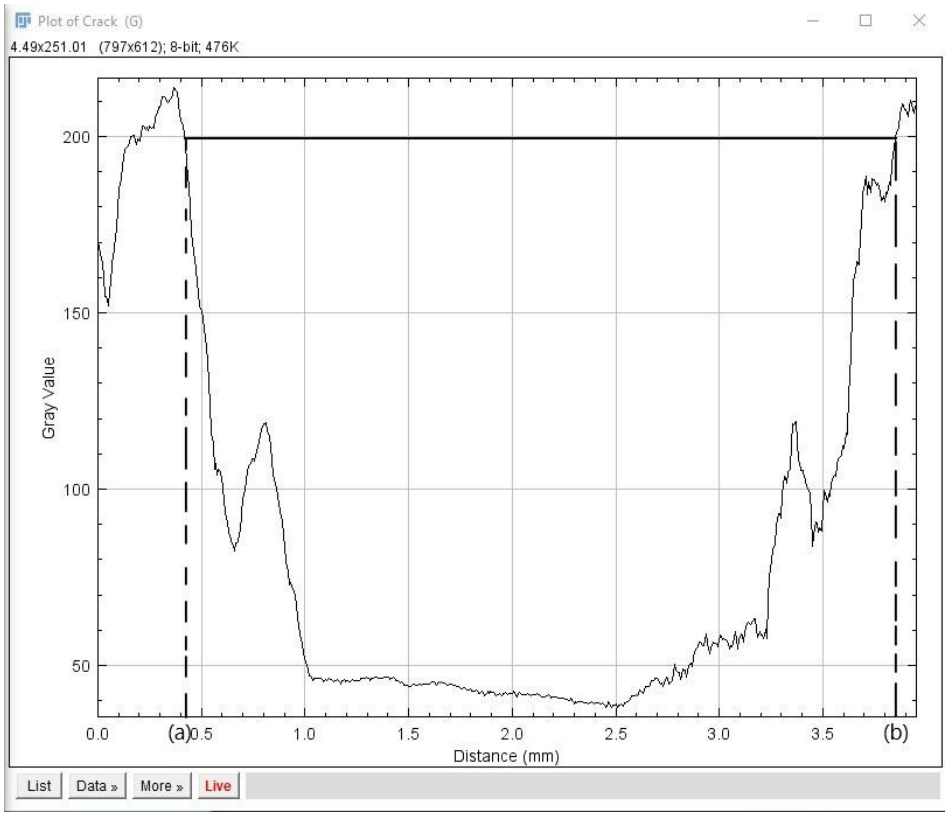

Figure 71. Gray value profile of ROI

Figure 71 shows the plot obtained from the image analysis that is used to obtain all measurements of crack width for the experiment. On the left and right of the graph, it is easy to identify the extents of the crack by considering that the surface of the sample is white (high grey value) whereas the crack is black (low grey value). This is shown in the image. The crack width therefore is (b) – (a) if a threshold grey value of 200 is chosen.

5.3.5 Detritus Inclusion

In the tests requiring the presence of detritus, 1g of detritus of 0.5mm grain size was funnelled into the crack until it was filled, shown in Figure 72. From the earlier experiment, on average 4g of detritus is obtained from a specimen of 100mm depth. Therefore, around 1g is expected to be observed across a 30mm depth.

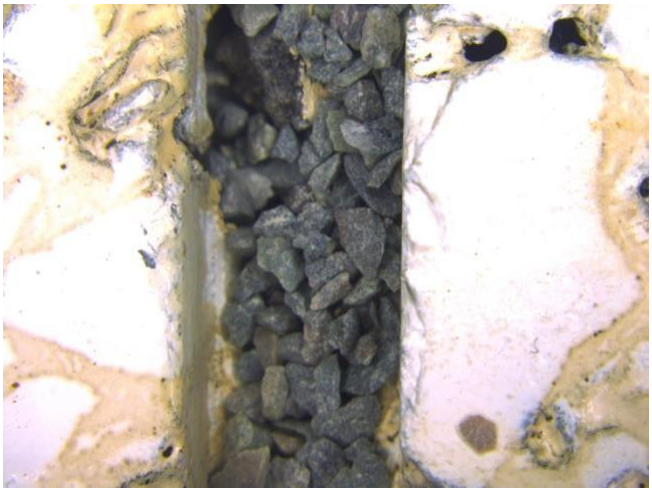

Figure 72. Image of detritus within a crack

5.4 Results

The results of the freeze thaw testing are discussed below.

5.4.1 No dirt, No water

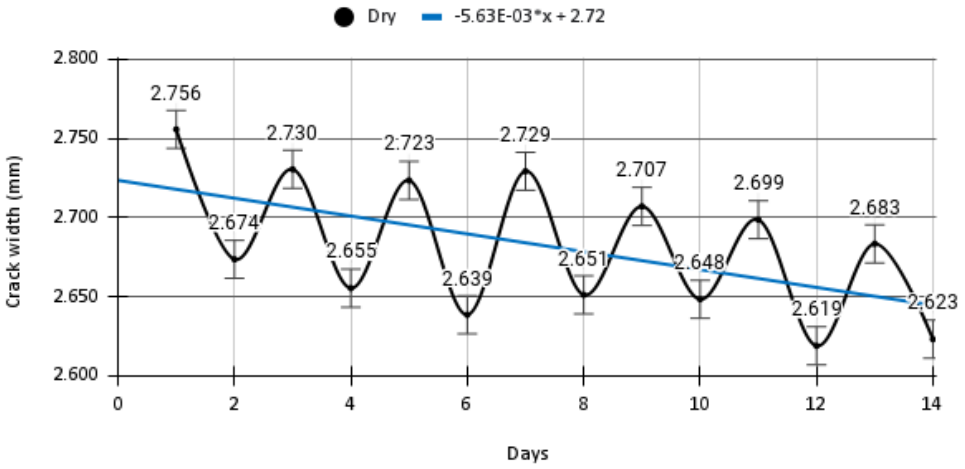

Figure 73. Graph of average measured crack width with increasing FT cycles in the "No dirt No water" case with trend line

Figure 73 shows the cycling of the asphalt sample's temperature from -10^{o}C to 20^{o}C in air and the presence of a downward trend in crack width over time. The extent of this downward trend is shown by the gradient -5.63 x 10^{-3}mm/day. The average initial width of the crack is also shown by the y-intercept of the trend line which is 2.72mm. Even though the thermal coefficients of thermal expansion and contraction are very similar, this trend may be due to the isothermal flow of the bitumen after having reached the target 20^{o}C in the 24 hours phase of thawing. If it takes the sample 10 hours for example to reach the target 20^{o}C, it will remain at that temperature for 14 hours at which point the contraction of the crack would no more be due to thermal expansion but simply due to the viscoelastic ability of the bitumen to flow at that temperature. Generally, the difference between peaks and troughs is in the region of about 60-90 µm.

5.4.2 Dirt, No water

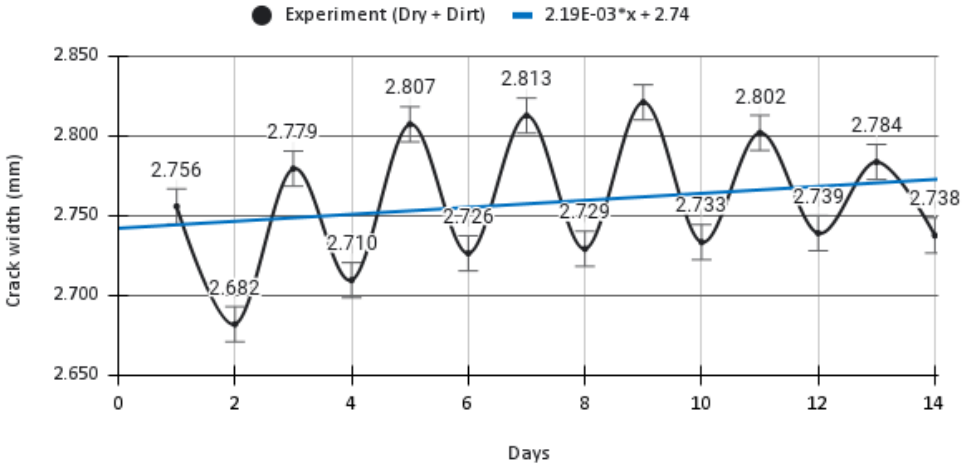

Figure 74. Graph of average measured crack width with increasing in F-T cycles in the "Dirt, No Water" case with trend line

Figure 74 shows the influence of the dirt in preventing crack closure, by the presence of a global upward trend in crack width over time. The extent of this upward trend is shown by the gradient 2.19 x 10^{-3}mm/day. The average initial width of the crack is also shown by the y-intercept of the trend line which is 2.74mm. What is also notable is a pattern in the thaw measurements, taken on the even numbered days (2,4,6, etc.) There seems to be an increase from 2.682 in the thaw measurement crack widths until it appears to plateau at about 2.738, which is an increase of about 56 µm. The grains seem to interlock to form a bridge across the crack width at different depths, and act to prevent crack closure, being incompressible in this context. The thermal expansion of the asphalt or the isothermal flow of the bitumen do not seem able to return the crack back to previous widths because of the presence of the coarse-grained detritus within the crack. Generally, the difference between peaks and troughs is in the region of about 50-100 µm.

5.4.3 No dirt, Water

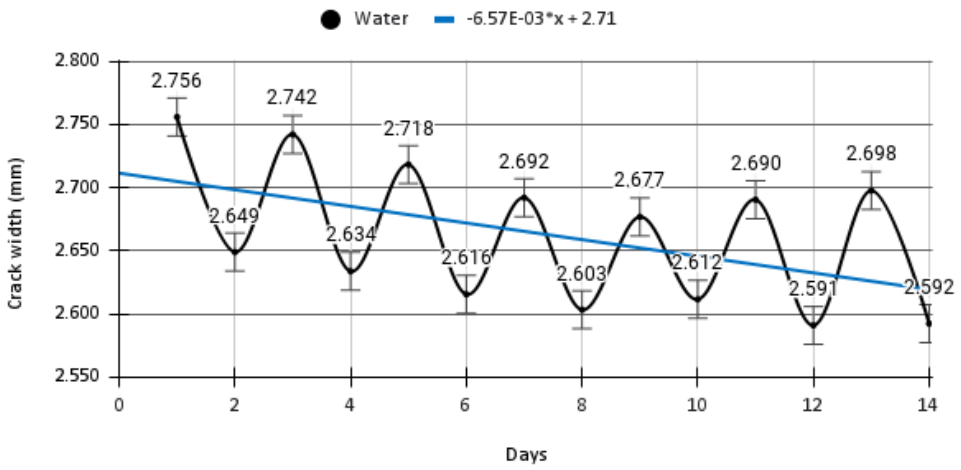

Figure 75. Graph of average measured crack width with increasing F-T cycles in the "No dirt, Water" case with trend line

Figure 75 shows the cycling of the asphalt sample's temperature from -10 to 20^{o}C in water and the presence of a downward trend in crack width over time. The extent of this downward trend is shown by the gradient -6.57 x 10^{-3}mm/day. The average initial width of the crack is also shown by the y-intercept of the trend line which is 2.71mm. This gradient is steeper than that of the gradient in air, although it appears to plateau as the graph approaches 14 days. This may perhaps be since water has a thermal conductivity 23 times that of air and so the specimen achieves the target 20^{o}C much quicker. This leaves more time and opportunity for the isothermal viscoelastic behaviour of the bitumen to close the crack further per cycle. This results in a global reduction of crack width because even though the thermal expansion of the specimen is fully recoverable, the viscoelastic flow may not entirely be. Generally, the difference between peaks and troughs is in the region of about 70-110 µm. This is also because the volumetric expansion as the water in the crack turns to ice may contribute to the crack opening, hence why it shows the largest differences across the 4 tests. Even though the ice has a free surface to expand upwards towards the opening of the crack, it is also expected to open outwards, pushing against the sides of the sample as well.

5.4.4 Dirt, Water

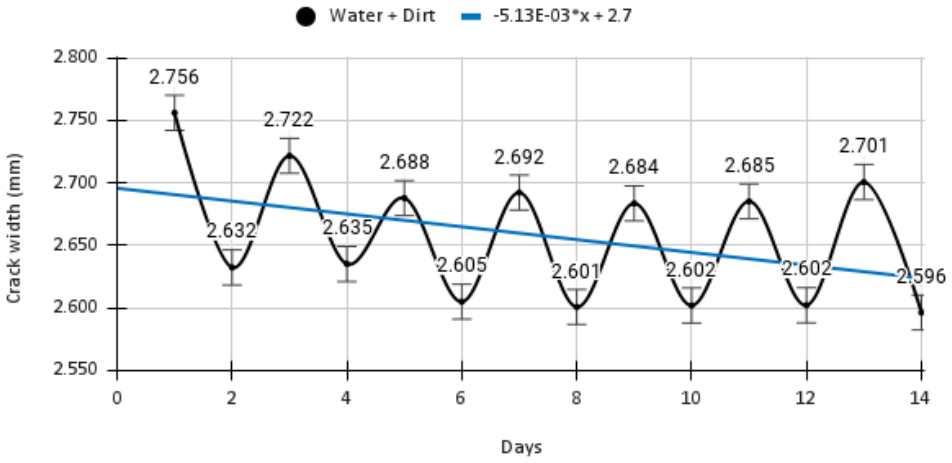

Figure 76. Graph of average Measured crack width with increasing F-T cycles in the "Dirt, Water" case with trend line

Figure 76 shows the cycling of the asphalt sample's temperature from -10 to 20^{o}C with water and dirt filling the crack and the presence of a downward trend in crack width over time. The extent of this downward trend is shown by the gradient -5.13 x 10^{-3}mm/day. The average initial width of the crack is also shown by the y-intercept of the trend line which is 2.70mm. This is the least steep negative gradient in the test. It appears that even though the dirt is attempting to prevent crack closure, perhaps because it is in water, the grains more easily rotate and do not interlock as much to form a bridge. Another feature that is characteristic of width plots of cracks with dirt in them is that there is a pattern that the thaw measurements follow, in that they are not particularly random. In this graph, the first and second trough remains at around 2.632-2.635, then the third to the sixth troughs plateau at 2.601-2.605. Perhaps, this drop in trough measurements between day 4 and day 6 may be due to this rotation and repositioning of particles in the suspension earlier spoken off. Generally, the difference between peaks and troughs is in the region of about 50-120 µm.

5.4.5 Changes in crack width

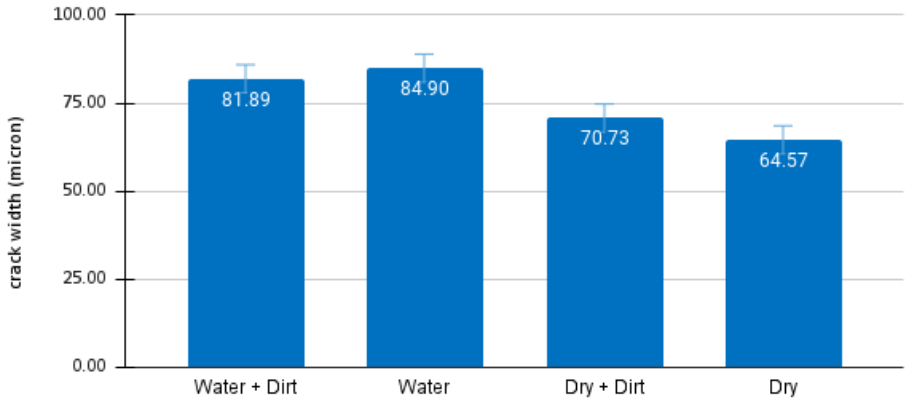

Figure 77. Graph of average change in crack width per cycle in each of the four F-T cycle cases

One freezing event and one thawing event make up one cycle, in that order. In Figure 77 we see that all these changes in crack widths are in the order of magnitude of what's expected for the thermal expansion and contraction of asphalt 150mm long, cracked at its centre, which is about a 100 µm change. In the graph, it is evident that the lowest recorded average crack change is in the dry case followed by the Dry + Dirt case. This is evidence to show that the prevention of crack closure by the dirt in turn increases the extent of crack opening in each cycle, albeit by about a 5 µm difference. The presence of water in the Water case causes the greatest average changesin the crack width (85 µm), with the volumetric expansion of ice as an aid. Comparatively, the Water + Dirt case is slightly less (82 µm), probably because there is less volume of water expanding into ice because the dirt occupies the rest of the crack's volume.

5.4.6 Crack Opening and Closure strains:

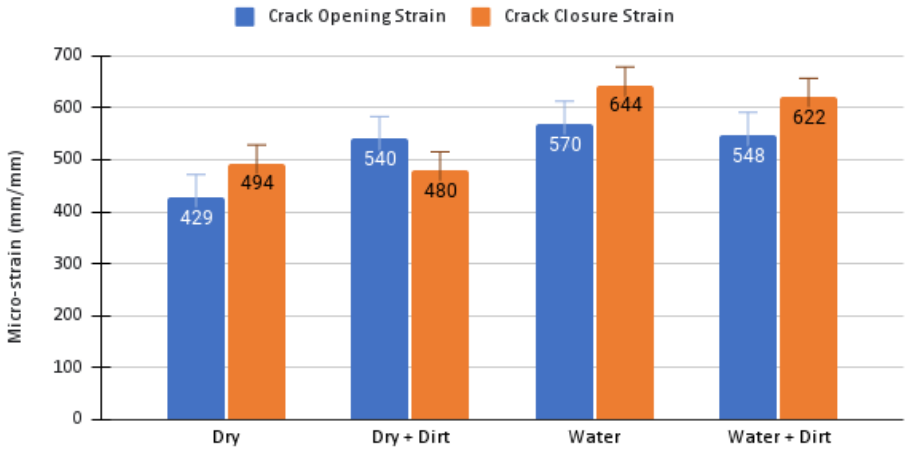

Figure 78. Crack of average crack opening and closing strain in each of the four F-T cycle cases

For every cycle of test, there are two phases, crack opening and crack closing. With each phase is an associated strain, a change in crack width relative to the previous crack width. Figure 78 shows the crack opening strain and crack closure strain for the different cases of test. In the dry case, the crack opening strain is 429 whereas in the water case, the crack opening strain is 570, with that difference of +141 micro-strain demonstrating the influence of the water/ice, on average. Now, another key feature of the graph is that the Dry+ Dirt case is the only scenario where the crack opening strain is greater than the crack closure strain. In every other test, the crack closure is greater than crack opening and there is a consistent difference of about 71 micro-strain between them. This would mean that in the absence of the dirt in the Dry + Dirt case, the crack closure strain would have been 611 micro-strain. However, because the dirt prevented the crack closure of the specimen, the crack closure strain was reduced to 480 micro-strain. Therefore, the quantifiable influence of the detritus is -131 micro-strain on the average crack closure strain. This may even be used to determine the residual stress carried by the sample because of the prevention of crack closure. In the case of the Water + Dirt, it is evident that the dirt affects the crack closure strain but not significantly. Interestingly it also indirectly affects the crack opening strain by reducing the volume of water present to volumetrically expand.

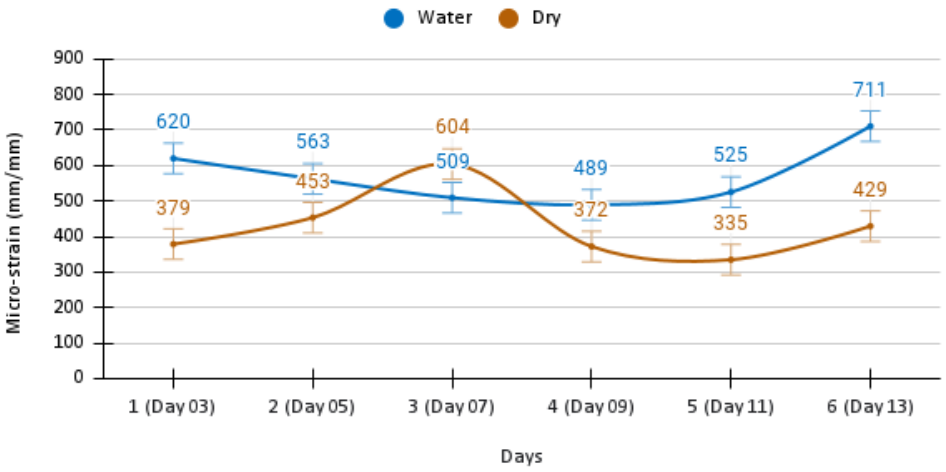

Figure 79. Graph of Crack Opening Strain for the "No Dirt, No Water" & "No Dirt, Water" cases

Prior to now, only average crack opening and crack closure strains have been considered. Now, the evolution of each strain for each day will be evaluated. Figure 79 demonstrates the potential of the volumetric expansion of ice in aiding crack opening. Most data points seem to show consistently that a crack width full of water expands more than a dry crack. The differences in crack opening strain range from about 110 – 282 micro-strain except for day 7. On Day 7, the dry specimen expands more than the wet specimen which has volumetric expansion of ice aiding in crack opening.

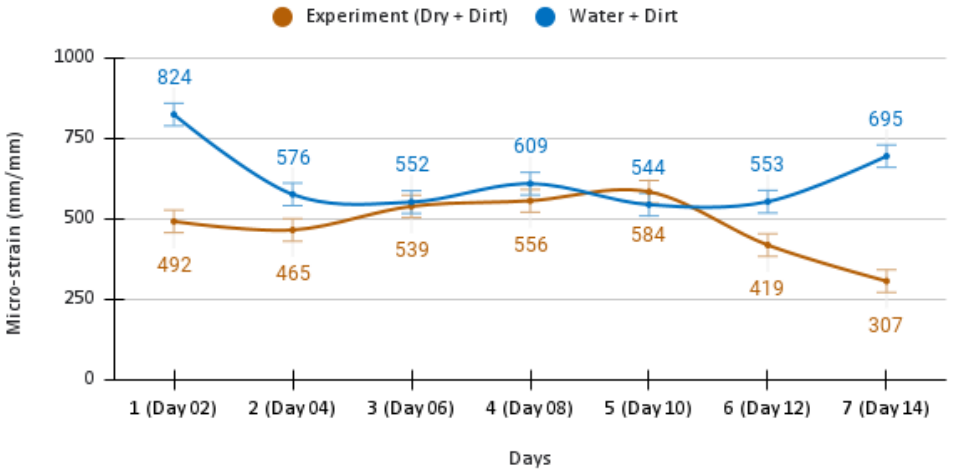

Figure 80. Graph of Crack Closure strain for the "Dirt, No Water" & "Dirt, Water" cases

Figure 80 demonstrates the potential of the detritus in preventing crack closure, even in suspension. Most data points seem to show consistently that a crack width full of water expands more than a dry crack. The differences in crack closure strain range from about 53 – 388 micro-strain except for day 10. On Day 10, the Water + Dirt specimen contracts less than the Dry + Dirt specimen which has detritus aiding in the restriction of the crack closure strain. This is perhaps because the detritus is in water and therefore the grains more easily rotate and did not interlock as much to form a bridge on that day.

5.4.7 Modelling

From Figure 78 showing crack opening and crack closure strain, the strain due to volumetric expansion of ice, crack closure prevention of detritus and isothermal asphalt flow can all be obtained. These strains are then multiplied by the initial width of the crack to obtain the value of crack width change they add or subtract.

Volumetric Expansion of Ice:

$$\Delta w_v = 150mm \times [opening\ strain\ (water) - opening\ strain\ (dry)]$$

Equation 44

$$\Delta w_v = (570 - 429) \times 10^{-6} \times 150mm$$ Equation 45

$$\Delta w_v = 22.9\ \mu m$$ Equation 46

Isothermal Asphalt flow:

$$\Delta w_{IAF} = 150mm \times [closure\ strain\ (dry) - opening\ strain\ (dry)]$$

Equation 47

$$\Delta w_{IAF} = (494 - 429) \times 10^{-6} \times 150mm$$ Equation 48

$$\Delta w_{IAF} = 9.73\ \mu m$$ Equation 49

Crack Closure prevention of detritus:

$$\Delta w_D = 150mm \times [opening\ strain\ (dry + dirt) + (622 - 548) \cdot 10^{-6} - closure\ strain\ (dry + dirt)]$$ Equation 50

$$\Delta w_D = 150mm \times 10^{-6} \cdot [(540 + 74) - 480]$$ Equation 51

$$\Delta w_D = 20.0\ \mu m$$ Equation 52

After these values were found, what remained was to find the J and K fitting terms which determine the linear combination of the freeze phase and the thaw phase. To test the model, the dry + dirt phase was used. In this case, because there is no water the volumetric expansion term is zero. Below is the table showing the J and K terms for the model.

Table 3. J and K fitting terms for dry + dirt freeze thaw modelling

Freeze-Thaw Cycles	Days	J term	K term
1	1 & 2	-0.61	-0.79
2	3 & 4	-0.58	-0.87
3	5 & 6	-0.73	-1.10
4	7 & 8	-0.76	-1.05
5	9 & 10	-0.80	-1.03
6	11 & 12	-0.52	-0.66
7	13 & 14	-0.42	-0.51

Figure 81 shows a model result plotted graphically with the experimental results. This is from the calculations made using Equation 43. With the greatest difference between the model and the experimental data being 7µm, the model is well fitted to the quantitative observations.

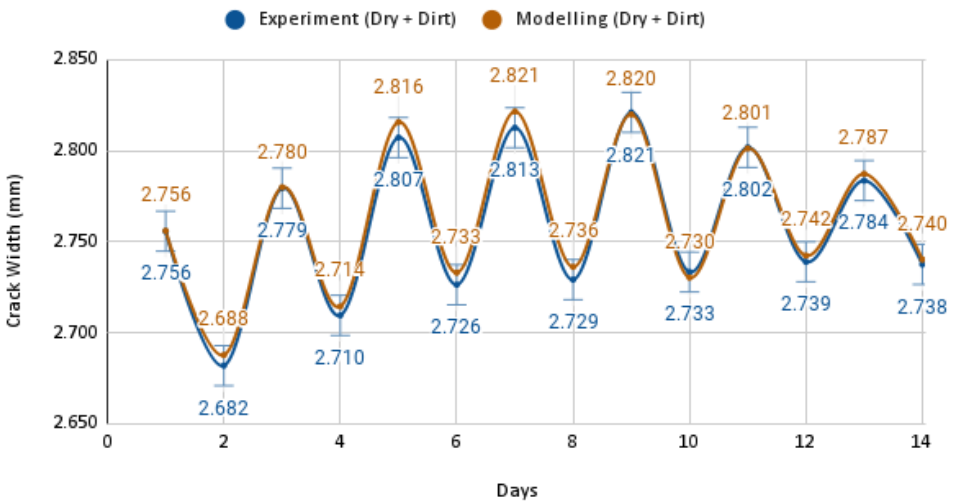

Figure 81. Graph of modelled and measured crack width for "dry + dirt" case

5.5 Summary

1. The freeze thaw testing of cracked asphalt has been carried out successfully, with the crack opening and closing by about 70-85 µm in each test.
2. When plotting crack width against time, most plots show a downward trend whereas dry + Dirt shows an upward trend, caused by the crack closure prevention by the presence of detritus. The generally downward trend is due to the isothermal viscoelastic flow of the asphalt.
3. In testing, two strains are measured: strain resulting from crack opening and strain resulting from crack closure. Out of four cases, Dry + dirt of grain size 0.5mm managed to reduce the strain resulting from crack closure by 20% (from a projected 611 micro-strain to 480 micro-strain).
4. The resulting 131 micro-strain can be used to obtain a thermally induced internal stress borne by the adjacent asphalt. Water + Dirt does not have significant potential to prevent crack closure because the dirt is allowed to rotate and cannot interlock to form a bridge in the suspension.
5. To validate the test results, thermal models have been developed involving thermal expansion and contraction coefficients, equations modelling the volumetric expansion of ice, isothermal viscoelastic flow of asphalt and detritus crack closure prevention.

6 Three-point Bending Experiment

6.1 Introduction

In previous chapters, the researcher has observed the presence of detritus in samples cored out of existing pavements in the UK road network. The researcher has also established that this detritus has the potential to prevent crack closure. In this chapter, the researcher now intends to investigate whether the influence detritus has on crack width translates into an indirect influence on the crack length. Having already simulated the effect of freeze thaw cycles in the laboratory, the researcher now seeks to mimic the impact of tyre loading on a pavement and the evolution of the resulting top-down cracks. Top-down cracking is a complex phenomenon. However, one simple way it is initiated is by the generation of significant tension on the surface of the pavement, triggering a crack to grow deeper as the crack mouth opens wider under the same tension. Models describing this crack evolution will be propounded and the novel experimentation used to validate these models will be discussed. Consequently, the relationship between crack width and crack length will be quantified and through this, the extent to which that relationship is altered by the presence of detritus will be determined.

6.2 Modelling

As mentioned in the literature review, the modelling of crack propagation of interest to the researcher is either phenomenological or from fracture mechanics. Fracture mechanics is not readily applied to the research because it does not factor in the effect of detritus in the crack. Phenomenological models however are also not birthed from any theory. The researcher therefore attempts to derive a ratchet mechanism model to characterise the effect of detritus on crack propagation. Take note of the following symbols

used to derive the crack growth ratchet mechanism.

$2\theta = rotation\ at\ crack\ tip\ or\ angle\ subtended\ by\ sides\ of\ crack$

$2r = crack\ width\ at\ crack\ mouth\ opening$

$l = crack\ length$

$l_0 = initial\ crack\ length$

$l_p = depth\ of\ detritus\ placement\ from\ crack\ mouth\ opening$

$\delta = forcing\ term\ that\ opens\ crack\ in\ expansion\ phase$

$r_p = detritus\ grain\ size$

$K = Stress\ Intensity\ Factor$

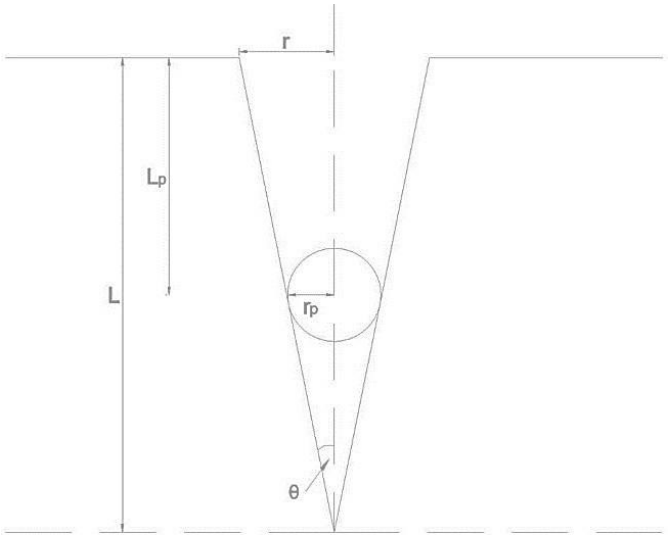

$$\tan\theta = \frac{r}{l} = \frac{r_p}{(l - l_p)} \quad \text{Equation 53}$$

$$r(l - l_p) = r_p l \quad \text{Equation 54}$$

$$l - l_p = \frac{r_p}{r} l \quad \text{Equation 55}$$

$$l - \frac{r_p}{r} l = l_p \quad \text{Equation 56}$$

$$l_p = l\left(1 - \frac{r_p}{r}\right) \quad \text{Equation 57}$$

Crack Expansion

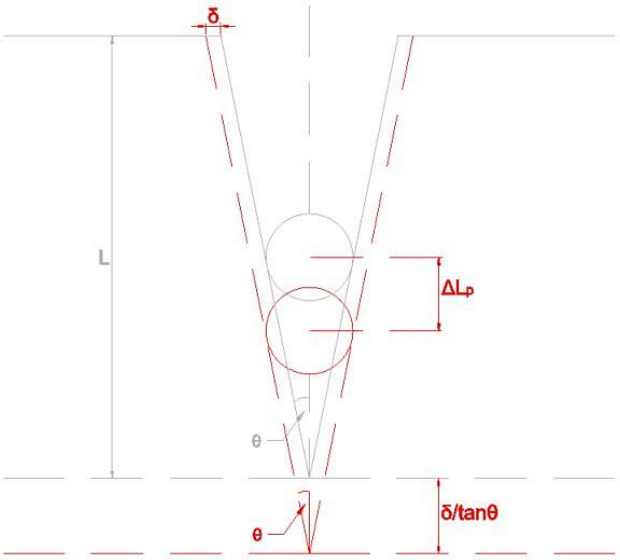

$$\tan\theta = \frac{r+\delta}{l+{}^{\delta}/_{\tan\theta}} = \frac{r_p}{l-l_p-\Delta l_p+{}^{\delta}/_{\tan\theta}}$$ Equation 58

$$\frac{r}{l} = \frac{r_p}{l-\left(l\left(1-{}^{r_p}/_{r}\right)\right)-\Delta l_p+\delta({}^{l}/_{r})}$$ Equation 59

$$\frac{r}{l} = \frac{r_p}{l-\left(l-l\frac{r_p}{r}\right)-\Delta l_p+{}^{\delta l}/_{r}}$$ Equation 60

$$\frac{r}{l} = \frac{r_p}{l-l+l\frac{r_p}{r}-\Delta l_p+{}^{\delta l}/_{r}}$$ Equation 61

$$\frac{r}{l} = \frac{r_p}{l\frac{r_p}{r}-\Delta l_p+{}^{\delta l}/_{r}}$$ Equation 62

$$r_p = \frac{r}{l}\left(l\frac{r_p}{r} - \Delta l_p + \frac{\delta l}{r}\right)$$ Equation 63

$$r_p = r_p - \frac{r}{l}\Delta l_p + \delta$$ Equation 64

$$\delta = \frac{r}{l}\Delta l_p$$ Equation 65

$$\Delta l_p = \frac{\delta l}{r}$$ Equation 66

Crack Relaxation

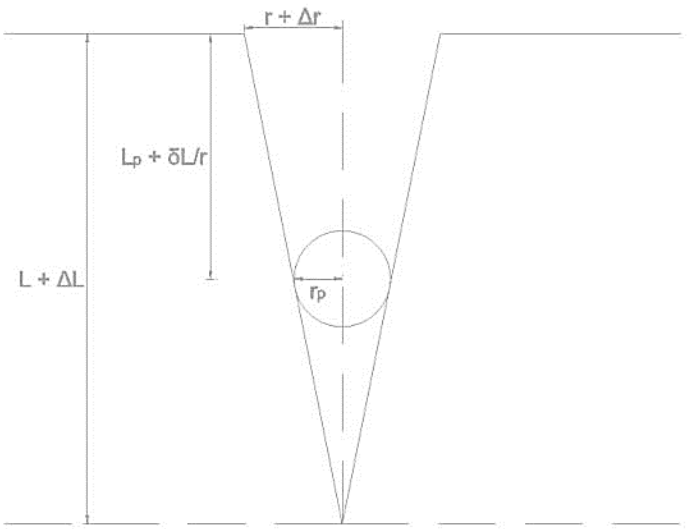

$$\frac{r+\Delta r}{l+\Delta l} = \frac{r_p}{l+\Delta l-\left(l_p+{\delta l}/{r}\right)}$$ Equation 67

$$\frac{r+\Delta r}{l+\Delta l} = \frac{r_p}{l+\Delta l-l+{lr_p}/{r}-{\delta l}/{r}}$$ Equation 68

$$\frac{r+\Delta r}{l+\Delta l} = \frac{r_p}{\Delta l+{lr_p}/{r}-{\delta l}/{r}}$$ Equation 69

$$\frac{r+\Delta r}{l+\Delta l} = \frac{r_p}{\frac{l}{r}\left(\frac{r}{l}\Delta l+r_p-\delta\right)}$$ Equation 70

$$(r+\Delta r)\times\left(\frac{r}{l}\Delta l+r_p-\delta\right)=\frac{r}{l}(l+\Delta l)\,r_p$$ Equation 71

$$r^2\frac{\Delta l}{l}+rr_p-\delta r+\Delta r\frac{\Delta l}{l}+\Delta rr_p-\Delta r\delta=rr_p+\frac{\Delta l}{l}rr_p$$ Equation 72

$$\frac{\Delta l}{l}\left(r^2+\Delta rr-rr_p\right)=\delta r+\Delta r\delta-\Delta rr_p$$ Equation 73

$$\frac{\Delta l}{l}\,r^2\left(1+\frac{\Delta r}{r}-\frac{r_p}{r}\right)=\delta\left(r+\Delta r-r_p\frac{\Delta r}{\delta}\right)$$ Equation 74

$$\frac{\Delta l}{l}\left(1+\frac{\Delta r}{r}-\frac{r_p}{r}\right)=\frac{\delta}{r}\left(1+\frac{\Delta r}{r}-\frac{r_p}{r}\frac{\Delta r}{\delta}\right)$$ Equation 75

$$\frac{\Delta l}{l} = \frac{\delta}{r}\left(\frac{1+\frac{\Delta r}{r}-\frac{r_p \Delta r}{r\ \delta}}{1+\frac{\Delta r}{r}-\frac{r_p}{r}}\right)$$ Equation 76

$$\Delta l = \frac{\delta l}{r}\left[\frac{1+\frac{\Delta r}{r}-\frac{r_p \Delta r}{r\ \delta}}{1+\frac{\Delta r}{r}-\frac{r_p}{r}}\right],\ where\ \frac{\delta l}{r} = \Delta l_p$$ Equation 77

In the absence of the detritus, the formula reduces to:

$$\Delta l = \frac{\delta l}{r}\left[\frac{1+\frac{\Delta r}{r}-\frac{r_p \Delta r}{r\ \delta}}{1+\frac{\Delta r}{r}-\frac{r_p}{r}}\right],$$ Equation 78

with no Detritus $r_p = 0$

$$\frac{\delta l}{r}\left[\frac{1+\frac{\Delta r}{r}-0}{1+\frac{\Delta r}{r}-0}\right] = \frac{\delta l}{r}$$ Equation 79

$a_{No\ detritus}(n)$ *is therefore modelled as shown below*:

$$a_{No\ detritus}(n) = l_0\left(1 + A\frac{\delta(n)}{r(n)}\right),$$ Equation 80

where 'a' is the crack length and 'n' is the number of cycles

where $\delta(n), r(n)$ *are empirical polynomial functions*

$A = an^2 + bn + c,$ *where* a, b, c *are fitting constants.*

$a_{detritus}(n)$ *is therefore modelled as shown below*:

$$\Delta l_n = \Delta l_{pn}\left[\frac{1+\frac{\Delta r_n}{r_{n-1}}-\frac{r_p\ \ \Delta r_n}{r_{n-1}\ \delta_n}}{1+\frac{\Delta r_n}{r_{n-1}}-\frac{r_p}{r_{n-1}}}\right],$$ Equation 81

where $r_n = r_{n-1} + \Delta r_n$

$$\Delta l_{pn} = A\frac{\delta_{av} \times l_{final}}{r_{final} \times n_{failure}},\quad A = an^2 + bn + c,$$ Equation 82

where a, b, c *are fitting constants.*

$l_{final} = 30mm - l_0,$ *for 3 pt bending*

$$a_{detritus}(n) = l_0 + \Delta l_{pn}\left[\frac{1+\frac{\Delta r_n}{r_{n-1}}-\frac{r_p\ \ \Delta r_n}{r_{n-1}\ \delta_n}}{1+\frac{\Delta r_n}{r_{n-1}}-\frac{r_p}{r_{n-1}}}\right]$$ Equation 83

6.3 Experiment

The experimentation is meant to simulate the scenario of a car tyre repeatedly passing over a road surface, thereby initiating a top-down crack that is propagated by fatigue. The researcher proposes that the three-point bending test with some amendments offers a good framework for this. If the conventional three-point bending test was inverted, (two load points at the top, 1 load point at the bottom) this would generate the tension at the top of the sample to cause top-down crack propagation. However, the layers underneath the surface course which counteract the load of the tyres need to be represented in the experiment as well. The researcher therefore proposes the use of rubber to represent this. Lastly, in order to simulate the pavement in saturated condition (e.g., on a rainy day), all this equipment needs to be set in a water-tight basin with some transparent window for crack measurement. With these alterations, the researcher can develop a novel testing rig capable of measuring the effect of water and detritus on the evolution of crack width and length. From the results of the previous chapter, it was understood that the dirt with water does not have a significant effect on the prevention of crack closure. Therefore, it has been excluded from the cases studied in this chapter. This is also because it is considered that the water may simply wash the dirt out of the crack. The samples used for the test are 10mm Stone Mastic Asphalt samples with dimensions 150 x 30 x 30mm as earlier described in the methodology chapter.

6.3.1 Bespoke equipment parts

Figure 82 shows the rendered model of the bespoke equipment for the three-point bending experiment.

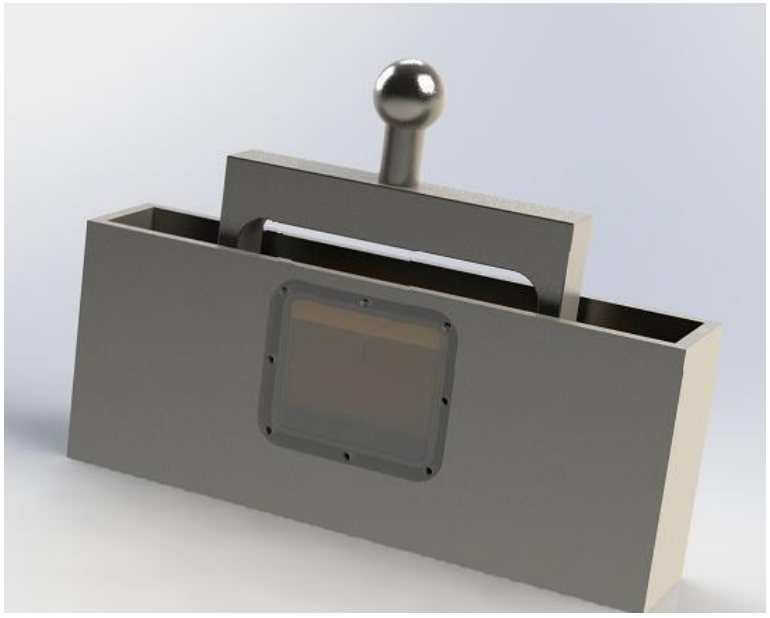

Figure 82. Image of 3D rendering of a Three-point Bending rig

Figure 83 shows images of the actual loading plate and basin.

Figure 83. Image of loading plate and basin

1. **Loading plate:** These are the two points acting on the top of the sample in the inverted three-point bending test. The distance between the two loading points is determined by an ASTM recommendation that states that for a single edge notched rectangular specimen, this distance should be four times the height of the sample. In this case, that distance is 120mm. The bulb at the top is a fitting for the NAT testing rig the novel equipment will be used with. This is made of aluminium because the entire unit is not in contact with water for long periods. Figure 84 shows an image of ASTM recommendation.

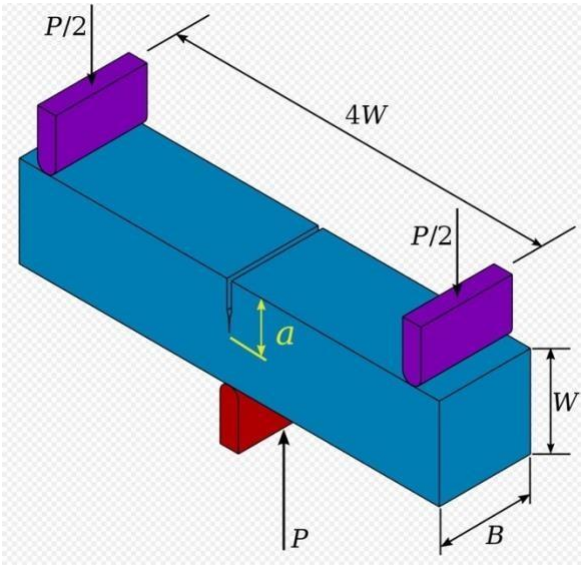

Figure 84. Image of ASTM recommendation. (Bower, 2009)

2. **Basin:** This is the most important aspect of the novel method. Within the basin is a triangular prism in the centre 30mm in height, acting as the third point underneath the sample. Also, on the ends are clamp plates for stretching rubber across to simulate the underlying layers. Lastly, there is the polycarbonate window, for the crack measurements. The length of the unit is the sum of the sample length (150mm) and the 40mm clearance either side of the sample to allow for any rotation as the sample cracks. The height of the unit is the sum of the triangular prism's height (30mm), height of the sample (30mm) and a 30mm clearance. Because of the prolonged contact with water, this unit is made of stainless steel.

6.3.2 Image analysis method

Once the test commences, there are two modes of data acquisition: from the NAT actuator, measuring load and vertical displacement or from an erected camera in front of the polycarbonate window, capturing crack length and width. Concerning image acquisition and analysis, a video of 5400s is captured for every experiment. Every video can be converted into a stack with 9-13 frames for each second of filming. To register, align and analyse all these image frames for each test would be very time consuming and very susceptible to Fiji Software crashes and lags. Therefore, the researcher opted to obtain images of the crack dimensions at 300s intervals, thereby using 19 data points to derive the global trend of crack width over time. Beside crack widths, there is also a need to quantify the extent of opening and closing with each cycle. Therefore, 19 three-second videos demonstrating the opening and closure of cracks every 300s intervals are also obtained. Once these images and videos are obtained for each test, they are set to scale, joined to form a stack, the stack is registered and aligned, and the grayscale profile is obtained for each frame. The change in crack width is derived from the changes in greyscale profiles. For the determination of the crack length, the initial crack length i.e., crack length at 300 cycles will first be measured, which is done by a simple line drawn and measured from the top of the sample to the tip of the crack. Thereafter, the test runs until the sample is fully fractured. Therefore, the change in crack length from beginning to end of a test is determined by the difference between the height of the sample (30mm) and the initial crack length measured at 300 cycles.

6.3.3 Detritus inclusion

In the tests requiring the presence of detritus, 1g of detritus of 0.5mm grain size was funnelled into the notch until it was filled. This is shown in Figure 85.

Figure 85. Image of detritus in notch

6.3.4 Rubber

As earlier stated, the rubber simulates the layer beneath the surface course. The underlying layers ensure that the surface course returns to rest after a load causing recoverable deformation to be taken away. Polycraft GP3481-F general purpose silicone rubber was used to represent this, with the following properties:

1. Curing time: 6 - 8 hours
2. Cured colour: light pink.
3. Hardness Shore A: 27
4. Tensile strength: 3 MPa
5. Linear Shrinkage: 0.2-0.5
6. Elongation at break: 520%

Out of these parameters, it is the Shore hardness of the rubber that determines its performance in resisting loads. The shore hardness is a

measure of the rubber's resistance to indentation and is measured by a durometer. A material of Hardness of 27 Shore A is classed as soft, almost as soft as a rubber band. This is shown in figure 86. Therefore, the resistance to deformation will be less than rubbers with higher hardness values. In this case, soft rubber is useful because it exaggerates the extent of crack opening and closing that would have been otherwise miniscule in a road, to adequately test the phenomenon of prevention of crack closure.

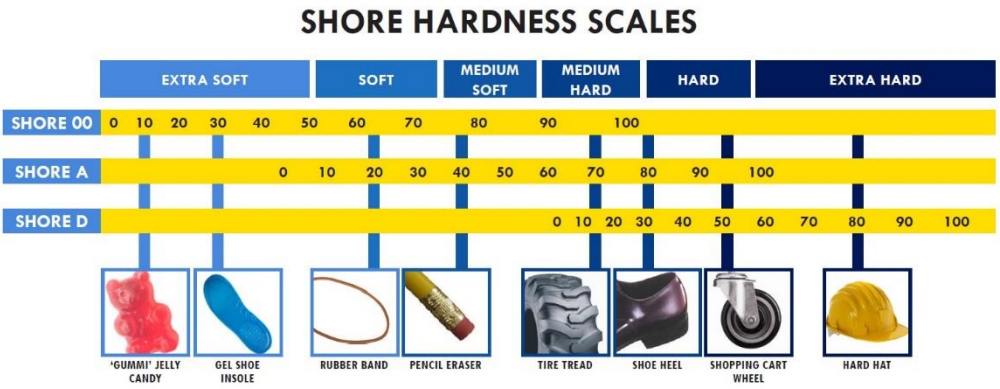

Figure 86. Image of shore hardness scales. Smooth-On, Inc. (2019)

6.3.5 Test

The white painted rectangular single edge notched sample (notched 5mm deep) is tested in displacement control, a haversine wave with a specified pk-pk displacement of 0.7mm at a holding load of 0.5kN at 1 Hz frequency at 20^{o}C temperature for 5400s. This will be carried out in the dry case, the water case and the dry with dirt case.

6.4 Results

All the samples tested in this experiment had a load curve and a vertical displacement plot. In the three-point bending test, the material property that quantifies a sample's resistance to flexure is called the flexural modulus; defined by Equation 84. In this experiment, it is referred to as the effective flexural modulus because the effect of the underlying rubber is not factored into equation 84. Table 4 gives the flexural moduli and failure point for all samples tested.

$$E_{flex} = \frac{L^3 F}{4wh^3 d},\ where: \qquad \text{Equation 84}$$

$L = Length\ between\ supports,$

$h = sample\ height,$

$w = sample\ width,$

$d = deflection,$

$F = force\ applied\ at\ midspan$

Table 4. The flexure modulus and failure point of specimens

Sample	Load (300 cycles)	Deflection (300 cycles)	Flex. Modulus (MPa)	Failure
Dry 1	1.86	5.31	186.68	2,700
Dry 2	1.74	5.36	173.13	4,500
Dry 3	1.95	4.82	215.81	5,400
Dry 4	1.72	5.32	172.80	3,000
Water 1	1.70	6.25	145.43	3,000
Water 2	1.89	5.92	170.04	2,100
Water 3	1.97	5.49	191.62	3,300
Water 4	1.85	6.14	160.81	2,700
Dry + Coarse 1	1.77	5.19	182.32	2,400
Dry + Coarse 2	1.79	5.38	177.10	2,700
Dry + Coarse 3	1.85	5.28	186.98	2,700
Dry + Coarse 4	1.87	5.36	186.27	4,200

The mean of the flexure moduli is 179.08MPa. All the samples fall generally within two standard deviations of the mean, where the standard deviation is 17.36 MPa.

6.4.1 Failure Criterion

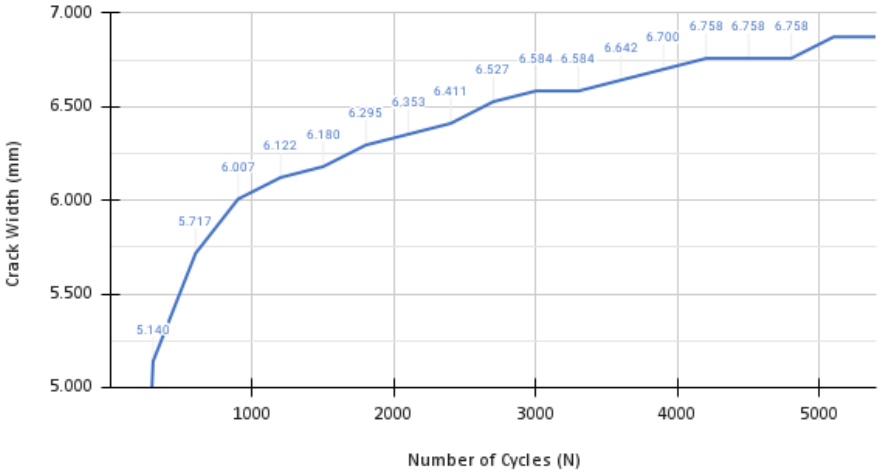

Figure 87. Graph of measured crack width over time for a typical sample.

In the experiment, the change in crack length from the beginning to end of a test is by finding the difference between the sample's height (30mm) and the initial crack length. It is also of interest to determine the point in time at which a sample is fully fractured using measurements of the change in crack width, that are more directly measured cycle by cycle. From the previous Freeze thaw experiment, a sample that is fully cracked opens by about 100 µm due to thermal effects. After this opening, the sample (generally speaking) then closes by the same 100 µm. Therefore, after one full cycle the crack width is unchanged if the opening and closing is recoverable. This will be assumed to be the failure criterion purely from crack width measurements: If the crack width remains unchanged for 2 consecutive data points.

In Figure 87, that point is 3000 cycles at a width of 6.584mm. Prior to 3000 cycles; there is a steady increase in crack width for every 300 cycles interval. The reason however, that the crack width increases even after the sample is fully fractured is the presence of the holding load (0.5kN), which pushes the

actuator down further each cycle, such that this target load is maintained. Once the sample is pushed down further, it is forced to open wider.

6.4.2 Cycles to failure

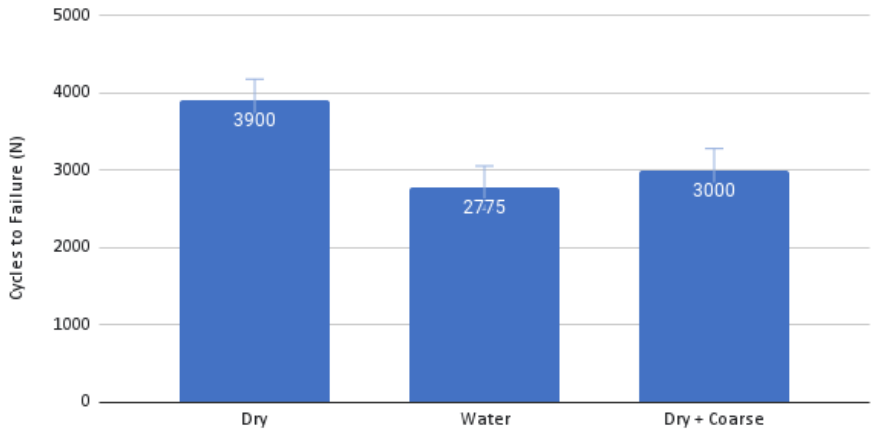

Figure 88. Graph of average cycles to failure for 'Dry', 'Water' and 'Dry + Coarse'

Figure 88 shows that the dirt causes samples to fail faster. This also shows that the greatest effect on crack propagation is the presence of water, seeing as those samples fail on average at 2775 cycles.

6.4.3 Crack width relationship

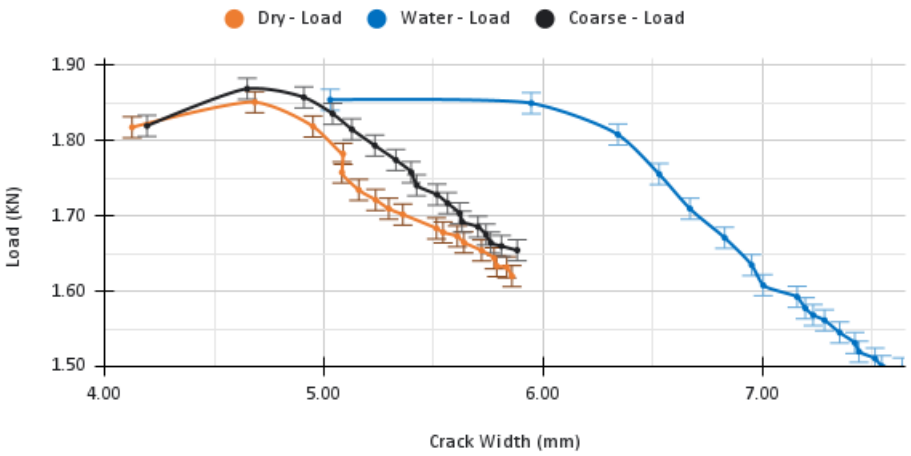

Figure 89. Graph of maximum load against crack width for 'Dry', 'Water' and 'Dry + Coarse' cases.

Figure 89 shows the correlation between the load incident on the sample and the evolution of crack width. This also has some physical meaning in what is typically observed in the road. It would be of interest to know the extent to which a crack will widen for a corresponding load exerted on it by a car tyre. In this figure 89, there is generally a negative correlation after a peak, with the water case showing the steepest gradient and widest range of values. To interpret the results, a given load is selected and the resulting crack widths from this are gleaned from the graph. For a 1.8kN load for example, a dry sample would have 5.0mm crack width, a Dry + Coarse sample would have 5.2mm crack width and a sample fully immersed in water would have 6.4mm crack width. This again shows the influence of the dirt to increase crack width independent of load and the influence of water to cause an asphalt sample to weaken in flexural strength.

6.4.4 Crack length relationship

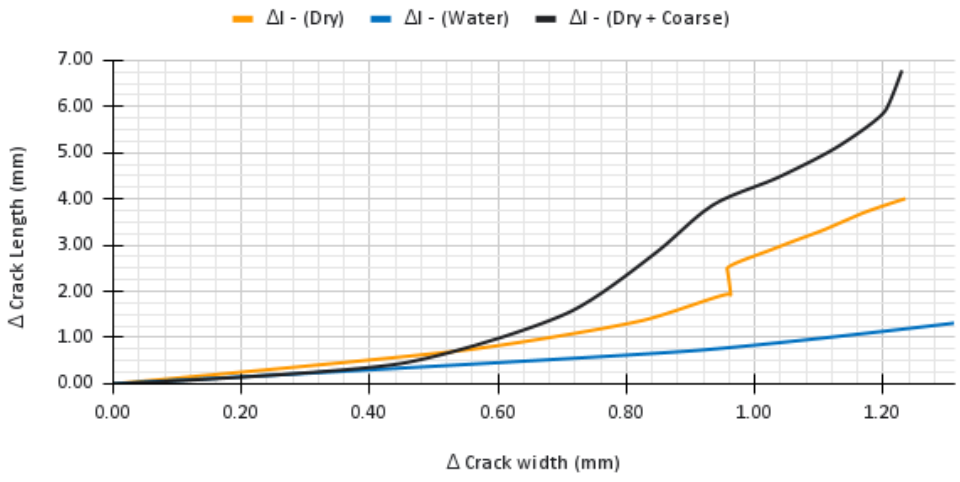

Figure 90. Graph of calculated change in crack length against measured change in crack width for 'Dry', 'Water' & 'Dry + Coarse' cases

Figure 90 offers a relationship between the change in calculated crack length and the change in measured crack width. This relationship is valid for crack widths from 4.13 – 7.64mm and crack lengths from 23.42 – 30.00mm. As earlier said the change in crack width was measured directly cycle by cycle.

The change in crack length from beginning to end was measured by the difference of sample height (30mm) and initial crack length. The change in crack length cycle by cycle was determined by the ratchet mechanism model, assuming a constant triangular shaped crack. According to the data, if the crack width changes by 1 mm in each case, the water sample will change by about 1 mm in crack length, the dry sample will grow by over 2 mm in crack length and the dry + Coarse sample will increase by over 4 mm in crack length. This demonstrates what the ratchet mechanism hypothesised, that by the prevention of crack closure, there will be an indirect increase in the crack length. In terms of whether the triangular shaped geometry assumed for the crack is valid, the images obtained during the test suggest that it is a reasonable enough assumption. This is shown in Figure 91.

Figure 91. Image of rectangular sample at end of test

6.4.5 Modelling

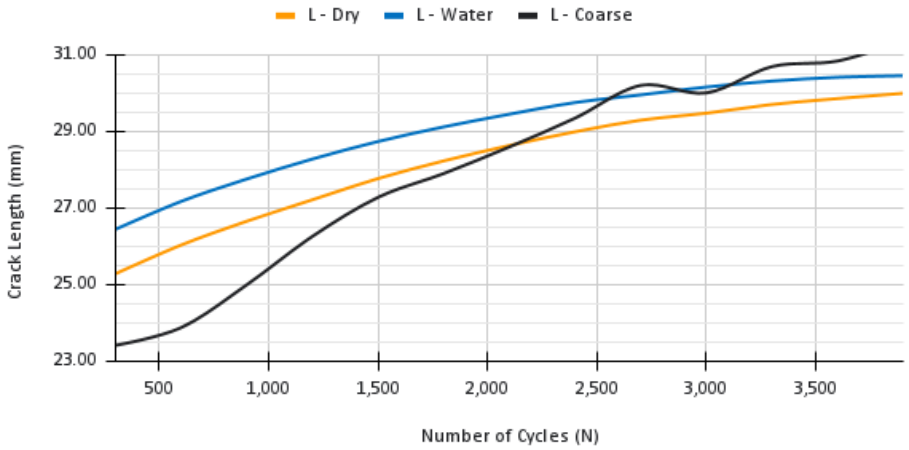

Figure 92. Graph of calculated crack length against number of cycles for 'Dry', 'Water' and 'Dry + Coarse' cases

Figure 92 shows the results of the model that is formulated in section 6.2, which uses crack widths, global crack length changes and delta opening terms to determine the corresponding crack length for every cycle. These values plotted are obtained from calculations obtained using Equation 83. The initial values the graphs begin from are the average initial crack lengths measured at 300 cycles. From the graph, it is postulated that the presence of water only pushes the dry curve upwards, as the two plots of dry and water seem relatively parallel and hence no change in gradient or rate of growth, from 0 to 3900 cycles. The presence of detritus however does show a change in gradient, denoting an acceleration in the rate of crack growth per cycle.

6.4.6 Rubber and local effects

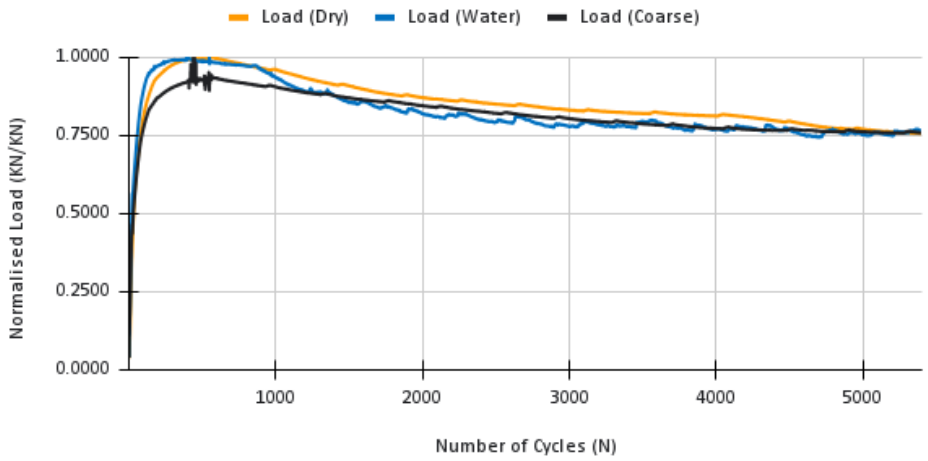

Figure 93. Graph of normalised peak to peak load against number of cycles for typical 'Dry', 'Water' and Dry + Coarse cases

As earlier stated, the experiment is run as a displacement controlled haversine test, set to a peak-to-peak displacement of 0.7 mm with a 0.5kN holding load. Therefore, for each cycle there is a minimum load which is always 0.5kN and a load required to achieve the 0.7 mm displacement, which is called the peak-to-peak load. The graphs of typical peak to peak loads are plotted in figure 93. Now these peak-to-peak loads have been normalised with all load values represented as a fraction of the maximum load for that test, achieved at around 450 cycles. The first point of interest is that all these curves approximate to some horizontal asymptote which is 75% of the maximum load. In all these cases, by 5000 cycles the sample has fractured and therefore offers no resistance to loads. The asymptote is therefore determined to be the influence of the underlying rubber that the sample continues to be supported on. The second point of interest is the local effects of the detritus on the load curves. At around 450 cycles, when the target displacements are finally reached by the machine, in this instance there are severe spikes in the load curve, up to about 8% of the maximum load. This occurs as the detritus falls and is wedged between the walls of the crack. By preventing crack closure, the sample fails to return to its initial orientation. Therefore, exerting the same 0.7mm displacement moves the sample further

down, pushing more against the underlying rubber and thereby requiring a greater load to achieve the same displacement. As can be seen in the graph, this is much more exaggerated in the local effect than it is in the graphs of global trends.

6.5 Summary

1. The dirt has the potential to increase crack width by about 100µm after for a cyclic load application of about 1.65 kN.
2. A relationship between crack width and crack length per cycle has been satisfactorily established, with the presence of the detritus causing a greater growth in crack length for a unit change in crack width.
3. The detritus also influences load curves locally, with spikes inload when the dirt engages with the walls of the sample to prevent crack closures.

7 Hydraulic Fracturing Experiment

7.1 Introduction

Asphalt pavements fail in a number of ways, some of which have been discussed in previous chapters; freeze thaw cycles, top-down cracking etc. In this chapter, the researcher investigates the role of pore water pressure in the asphalt cracking problem and the effect of detritus on this scenario. On a rainy day in the winter, precipitation percolates into the pores of a road and is trapped. With time, the pavement may even become saturated. When a tyre passes over the saturated strip of road, it pressurises the water existing in the pores. The water in turn pushes against the surrounding asphalt material. This can cause the coalescing of pores which etch out a crack path. This mechanism of failure is an established one in the field of hydraulic fracturing; where pressurised fluid containing proppants is used to fracture rock formations and the proppants within the fluid sit in the cracks of the rock, holding them open for shale gas extraction. In the subsequent paragraphs, the models and principles governing fluid-driven crack propagation in hydraulic fracturing will be applied to asphalt cracking and the novel equipment required for the testing of asphalt in this failure mode will be discussed.

7.2 Modelling

To characterize fatigue failure which may be caused by the fluid, a phenomenological model was adopted as shown below:

$$N_f = A\left(\frac{1}{\varepsilon}\right)^b \qquad \text{Equation 85}$$

$where\ N_f = Cycles\ to\ failure,\ \ \varepsilon = initial\ strain$

$A, b\ are\ fitting\ constants$

7.3 Experiment

A 50% asphalt filler blend mastic of 100mm diameter and approximately 30mm thickness, weighing 280g is poured into the mould. The sample is conditioned at 5^{o}C but is tested at room temperature. The bespoke equipment shown in Figure 94 is filled with 30ml of water and loaded using a cyclic load from 0.05kN compression to 0.5kN compression force (707.4 kPa water pressure) at a rate of 1Hz. The test is load controlled. The failure criterion is to observe a leakage in the centre of the specimen, this is the sign that the fluid has initiated and propagated a crack from within the sample to the surface (15mm travel). The test will be carried out with and without dirt.

7.3.1 Bespoke Equipment parts

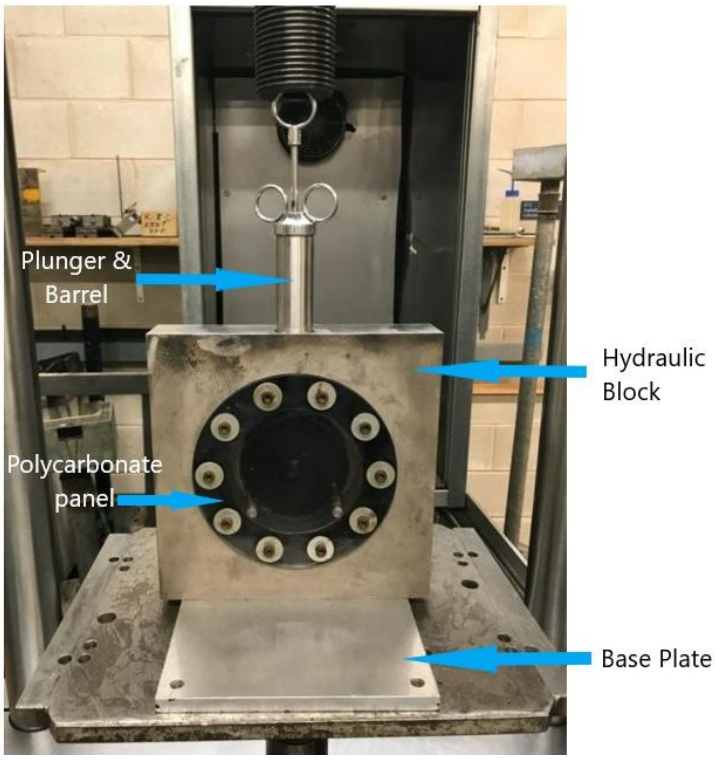

Figure 94. Hydraulic Fracturing rig

1. **Plunger and Barrel:** This is the element that will serve as the reservoir, storing the material to be pumped into the sample. The barrel is 30mm in diameter and 100mm in length. It is made of stainless steel and is resistant to rust. The plunger is obviously the unit driving the constituents of the barrel into the

specimen. It has fitted around its mouth an O-ring, to ensure no leakage of water between the plunger and inner walls of the barrel when pressurising the fluid. The top of the plunger is also the element that is in contact with the MAND actuator and transfers the loads inputted to the fluid. The plunger has about 80mm travel.

2. **Syringe unit:** The syringe unit is the intermediary link between the barrel and the sample. The contents of the barrel are pushed through the syringe unit and are emptied out in the matrix. It is screwed on and fastened to the Hydraulic block. It is approximately 100mm in length and is made of two parts: the first part screwed onto the barrel has an inner diameter of 10mm, and the second part which is set into the centre of the sample it has an inner diameter of 6mm. O-rings are used where appropriate in this unit to ensure watertightness. The syringe unit is made of stainless steel, which is shown in Figure 95.

Figure 95. Syringe Unit

3. **Hydraulic Block:** This is the main unit. It is a 250mm x 250mm x 50mm stainless steel block with a few features. Firstly, it has a 120mm diameter wide and 35mm deep chamber that is machined out to house the specimen. It also has in addition to that a 5mm recess to house a rubber gasket and polycarbonate screen. There are also screws underneath the block to screw onto a base plate. At the top is a 50mm deep, 35mm diameter wide recess such that the barrel appears sunk into the block.

4. **Polycarbonate screen:** This is the transparent screen placed in the 5mm recess with a rubber gasket. This aids in viewing the aperture and blocks the observer from aggressive water jets and projectiles coming from the sample, during the test.

5. **Base Plate:** This is connected to the hydraulic block and helps to offer more stability when stood upright, because of the block's lack of significant thickness. It also aids in more convenient conveying of the heavy block. Figure 96 shows a 3D rendering of the base plate connected to the hydraulic block.

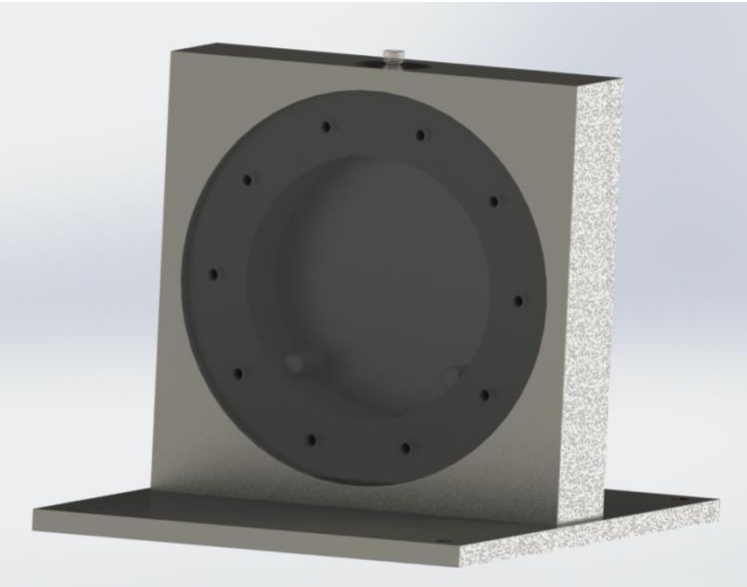

Figure 96. Hydraulic Block and Base plate Render

7.3.2 Sample Preparation

The sample is a 50% asphalt filler mastic blend. 140g of pen 20 grade bitumen is heated to 180^{o}C. It is then poured into a tin and the tin is placed on a hot plate at maximum temperature. 140g of aggregate filler is then measured and poured into the tin, being mixed over the hot plate to maintain the fluid nature of the bitumen and thus workability of the filler blend. To prepare the mould, rubber units of 10mm thickness are to line the circumference of the sample chamber to achieve a 100mm diameter specimen. Also, a rubber covered rod should be placed in the syringe unit to prevent the filler blend from entering the syringe. It should be sufficiently greased to prevent the

material sticking to the mould after testing. Once the mould is prepared and the filler blend is mixed to form a consistent substance, it should be poured into the sample chamber. It should then be placed in a conditioning cabinet set at 5^{o}C and allowed to cool overnight.

7.3.3 Detritus Inclusion

In the tests requiring the presence of detritus, 5g of aggregate filler is placed into the barrel before the experiment commences, and 20ml of water is poured in and mixed with it.

7.4 Results

Six tests were run in the experiment. Two experiments were conducted with only water and the remainder of the experiments were water with dirt. This was because of the better repeatability between the water tests and the lower repeatability with the water + dirt tests, therefore requiring more repetitions. Because of the uniqueness of each test, they will be analysed individually. Thereafter, key implications of the results may be placed in the larger context of the test and hypothesis. The failure mechanism is defined by an orifice or aperture forming on what is observed as a bulge or a blister on the surface of the mastic asphalt due to the pumping of water.

7.4.1 Peak to Peak Displacement

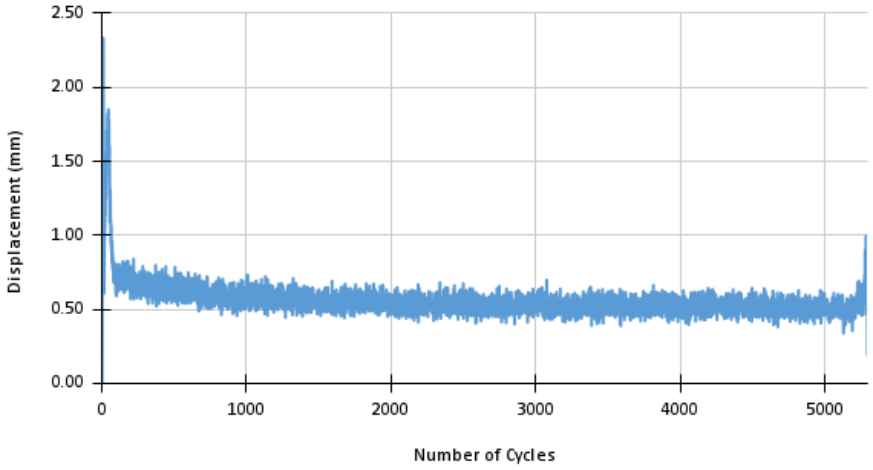

Figure 97. Peak to Peak displacement for a typical test with water

Figure 97 shows the peak to peak of the load controlled cyclic displacement of the plunger applied to the water in the barrel. At the beginning of the test, the MAND machine is set to cycle between a minimum load of 0.05kN and a maximum load of 0.5kN in one second. The graph above is what this 0.45kN load change equates to in terms of vertical stroke for every cycle. The double amplitude tends to 0.5mm as the test progresses past 2000 cycles. The 0.5mm vertical stroke equates to about 0.4ml water pumped per cycle.

7.4.2 Displacement

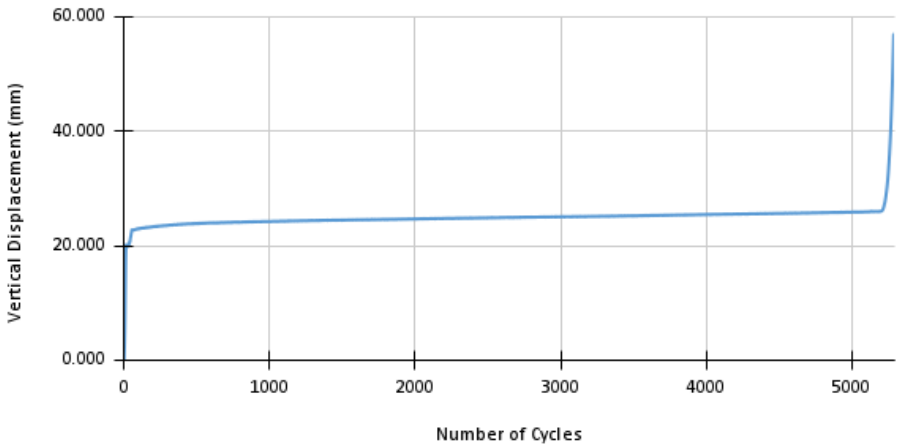

Figure 98. Displacement of the plunger plate for a typical test with water

Figure 98 shows the average or mean displacement of the plunger plate from the beginning of the test with time. This plot resembles a typical power series plot. At the beginning of the test, the plunger plate goes down and compresses the air present until it starts to exert a force of 0.5kN on the water, then it reaches a steady state. The mean change in position of the plunger plate's cycling between 0.05kN and 0.5kN is what is shown above. Then after 5000 cycles, fatigue causes an aperture or orifice to form on the surface of the mastic asphalt blister and the water gushes out of the orifice under high pressure. An image of this is shown in Figure 99.

Figure 99. Water jet

In the end the total travel of the plunger plate is about 60mm. However, it is the displacement of the steady state that gives insight to the volume of water pumped to form the blister and then eventually the cracking of the blister in the form of an aperture or orifice on its surface.

7.4.3 Volume

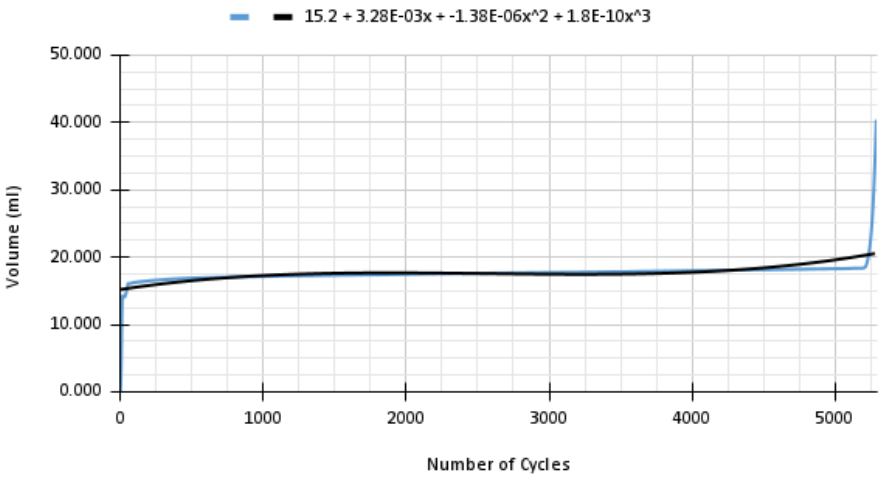

Figure 100. Volume pumped in a typical test with water.

Figure 100 is obtained by multiplying the displacement plot by the area of the 30mm diameter wide plunger plate. The volume therefore also resembles a typical power series plot. One significant point to note is the y-intercept, which gives some inclination of the volume of air present to be compressed. Also of note is the total travel. The range of volume values in the test is about 40ml. This is a relatively consistent reading, seeing as around 15ml of air and 30ml of water is underneath the plunger plate. The gradient of the steady state phase of this graph is what gives a value of the volumetric flow rate of each experiment. In Figure 100 for example, the air is compressed in about 100 cycles, and the sample fails in about 5000 cycles. The failure volume obtained is the difference in water volume at these two points in the experiment, and the flow rate is that difference divided by 4900. This is shown in table 5.

Table 5. Test Properties

Test	Failure Volume (ml)	Cycles to Failure	Flow Rate (ml/cycle)
T1 - Water	3.792	5,220	7.26E-04
T2 - Water	3.956	5,257	7.53E-04
T3 - Dirt	1.495	3,829	3.90E-04
T4 - Dirt	3.902	4,565	8.55E-04
T5 - Dirt	1.857	3,091	6.01E-04
T6 - Dirt	2.033	2,533	8.03E-04

Table 5 shows the key properties of each test conducted. The failure volume is the amount of water or suspension pumped by the time an orifice is observed on the surface of the specimen. The flow rate is obtained by dividing the failure volume by the cycles to failure. From the results above, it is demonstrated that the presence of the detritus causes the sample to fail faster. All dirt samples failed in around 2500-4500 cycles, whereas the samples without dirt failed in about 5300 cycles.

Regarding the development of the mastic asphalt blisters, the dirt present seems to prevent it from relaxing and forms an internal cake lining on the frontier of the blister. This is shown below in Figure 100

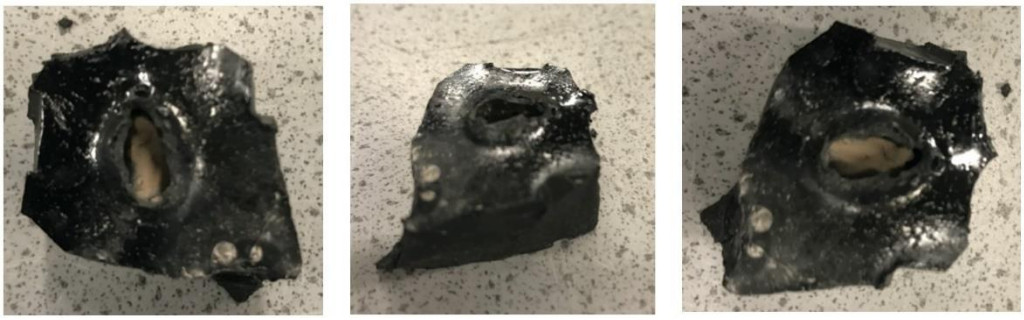

Figure 101. Image of Internal detritus cake for Test 5 (T5)

It is hypothesized that when the water is pumped, the detritus prevented the blister relaxation when the pressure is unloaded. This process continues and accelerates the growth of the blister, such that the membrane stresses are sufficient to cause a tear and form an aperture on the blister's surface. This may also account for the reason why with generally lower volumes pumped at time of failure, the samples fail faster.

In terms of flow rate, in some cases, the introduction of dirt increases flow and in other cases reduces flow. Figure 102 shows the orifice at time of failure for T5, when the test is carried out with dirt.

Figure 102. Image of sample at point of failure for Test 5 (T5)

Figure 102 shows water mixed dirt oozing out of the orifice as compared to Figure 99 where are water jet was gushing out of the aperture. This oozing effect was observed for Test 3 (T3) and Test 5 (T5). In the cases of these tests,

the flow rates were much lower than the flow rates of tests with just water.

In the case of T4 and T6, the water gushed out of the orifice as a water jet, and the emitting appeared not to have mixed with the dirt. The resulting flow rates in these tests were higher than the flow rates of tests with just water.

The reason for this variation is also hypothesized to be the placement of the internal detritus lining as well as the position of the orifice on the blister. If there is no detritus lining the blister behind the orifice, it means the fluid driven crack only had to travel through the asphalt. Otherwise, the fluid must travel through the asphalt as well as the lining of detritus on the inner walls of the blister. This is purely a hypothesis and an inference from the qualitative observations of the test.

7.4.4 Modelling

The terms A and b can be found to complete the phenomenological relationship in Equation 85. The strain on the asphalt was not directly measured. However, because the water in the barrel is incompressible at test pressures in a closed system, it is deduced that the strain on the asphalt is proportional to the change in the height of the water column in the barrel. This is shown in equation 86:

$$\varepsilon = \beta \cdot \frac{h_{300} - h_{air}}{h_{air}} \qquad \text{Equation 86}$$

$where$:

$\varepsilon = initial\ strain,$

$h = height\ of\ air/water\ column\ in\ barrel,$

$\beta = constant\ of\ proportionality$

Because the experiment is measuring change in cycles to failure in the presence of dirt relative to tests in the absence of dirt, whatever value of β is chosen is constant for all tests. Arbitrarily, it will be therefore set at 0.5. The water column pumped in the first 300 cycles of the test will be used to determine initial strain. In order to obtain the water column pumped in the

first 300 cycles, the height of the air column compressed must be subtracted from the total actuator travel in the first 300 cycles. The length of the air column is obtained from the y-intercepts of the trend lines of each experiment's displacement graph. Values of this for each test is shown in table 6 below.

Table 6. Table showing values for initial strain calculation.

Test	Air column length (mm)	Total travel at 300 cycles (mm)	Initial strain (mm/mm)
T1 - Water	21.50	23.57	0.048
T2 - Water	21.22	22.65	0.034
T3 - Dirt	13.60	13.80	0.007
T4 - Dirt	15.84	16.47	0.020
T5 - Dirt	15.56	16.47	0.036
T6 - Dirt	15.56	16.52	0.031

The natural log of Cycles to failure is plotted against the natural log of the reciprocal of the initial strain, after which a trend line is plotted through the scatter to obtain the values of A and b to complete the phenomenological model. In the case of dirt, this is shown in Figure 103 below.

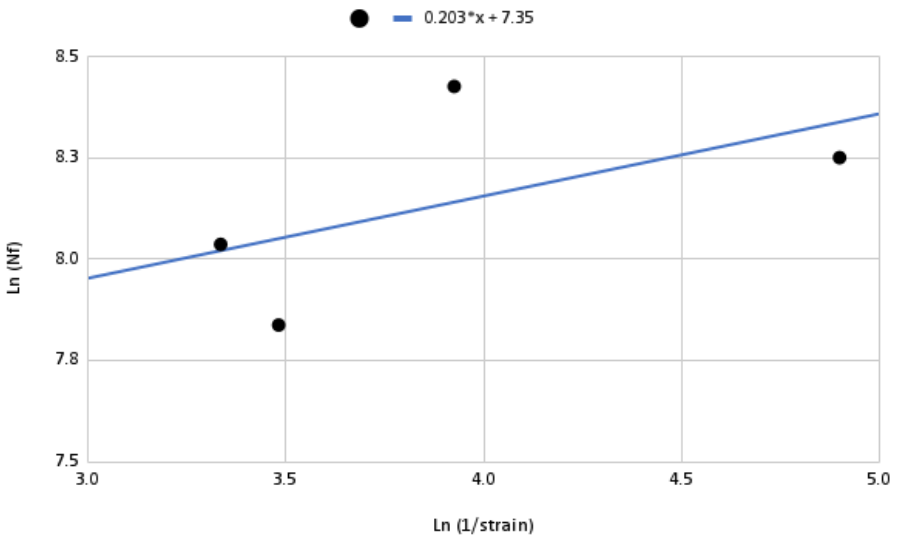

Figure 103. Trend line to obtain phenomenological model constants for dirt case.

Therefore, using the equation and values of strain, the A and b terms can be found. This is shown in Table 7.

Table 7. A and b terms for phenomenological model

Regime	A	b
Water	4915	0.020
Dirt	1556	0.203

For the research, the stress chosen to control the test was at 707.4 KPa. It is evident as shown in figure 104 that the dirt causes the sample to fail faster for initial strains greater than 0.25%, assuming β = 0.5

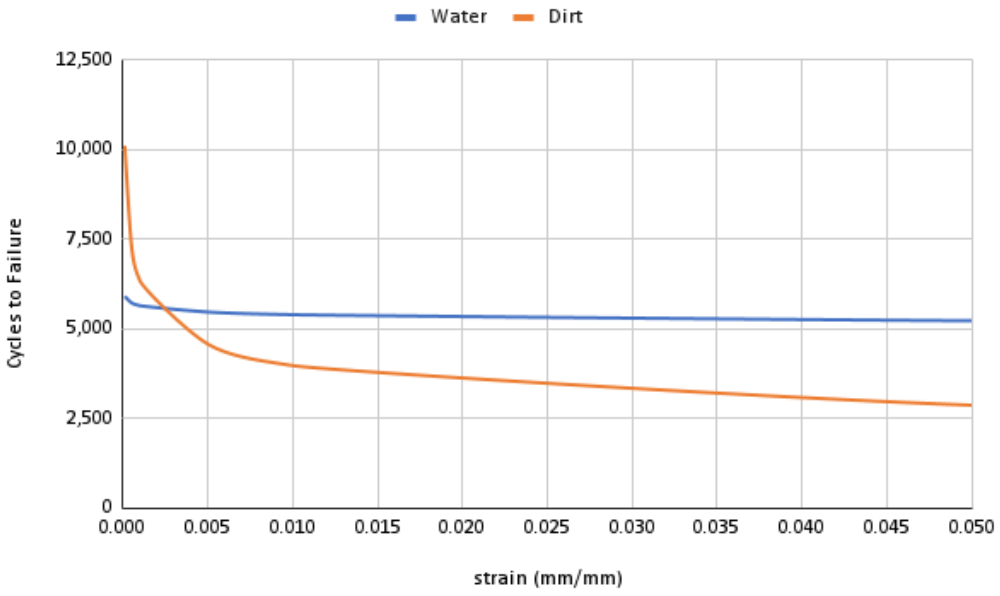

Figure 104. Phenomenological model

7.5 Summary

1. Detritus can accelerate the rate of fluid driven crack propagation through an asphalt mastic.
2. A novel experiment has been developed in which an asphalt mastic is poured around an injection needle in a bespoke mould such that the needle mouth is positioned in the centre of the mastic when it hardens. The top of the needle is then connected to a barrel which is filled with

water and a plunger plate pushes the water into the sample, much like a syringe.

3. In the tests carried without dirt the sample fails in 5200-5300 cycles. In the tests carried out with dirt the sample fails in 2500-4500 cycles.
4. The dirt seemed to be deposited more in the asphalt blister and formed a cake on the lining of the blister such that the geometry is not permitted to relax upon unloading.

8 Conclusion and Future Work

The intention of this project was to experiment and model the formation of road surface potholes. Firstly, the formation of a pothole that initiated from the surface of the road downwards was broken down into four main stages:

1. Crack Initiation/Presences of voids
2. Crack Propagation/Interconnection of voids
3. Pothole carving/ Interconnection of cracks
4. Pothole Forming/dislodging

The second stage of crack propagation/interconnection of voids was isolated as the main driving force of the pothole forming process, and thus chosen as the subject of the study. To measure the validity of this initial hypothesis, it had to be compared to reality somehow. In response to this, a widely accepted observation offered a good starting point: that potholes form more frequently in winter than the rest of the year. Having evaluated the peculiarities of the wintertime, the researcher arrived at a set of parameters that were to make up the framework of testing for accelerated crack propagation/interconnection of voids as the driving force for commensurately accelerated pothole formation. These were:

1. Effect of freeze thaw cycles on the pavement
2. Top-down crack propagation due to tyre loading
3. Increase in precipitation and the potential of the pavement to hydraulically fracture.
4. Presence of detritus transported into cracks.

Road surface detritus deposited into the cracks became the novelty of the research, because in evaluating factors that made roads more susceptible to crack propagation in the winter, it seemed to be the one least researched in pavement engineering. Something analogous to this however had been

researched at length in Chemical Engineering, in the study of hydraulic fracture and proppant technology. To harness shale gas, pressurised fluids create cracks in rock formations and coarse particles called proppants in the fracture fluid hold the crack open as the gas escapes out of it. This seemed to have significant bearing on how the role of incompressible road surface detritus was perceived by the researcher and that in the context of pothole formation its influence was underestimated. This gave the researcher more impetus to make the detritus' potential to prevent crack closure the focal point of the research. It was therefore hypothesised that by the prevention of crack closure, a ratchet mechanism will trigger the crack to grow progressively wider and the crack will be encouraged to grow further and faster. To provide a context within which to evaluate the influence of detritus, the other three significant factors to pothole formation had to be simulated in a laboratory scenario in a novel way, seeing as the novelty of detritus was hardly tested prior in the pavement engineering academic community.

To accomplish this, a comprehensive knowledge base had to be established by an appraisal of the relevant literature. This spanned from an overview of fatigue cracking asphalt, water damage, temperature cycling and even to hydraulic fracturing and proppant technology models. This was carried out in chapter two of the thesis. From this, the purpose of chapter three was to make concrete the approach of the investigation. The novel and innovative test methods required for the successful interrogation of the hypothesis were laid out and outlined, to be frequently referred to in latter chapters of the thesis. With a research motivation, a good knowledge base and a workable methodology framework demarcated, the remainder of the thesis was focused on the fulfilment of the four objectives outlined in the introduction chapter. With a chapter dedicated to each one, the objectives are:

1. To develop a novel experiment to prove the presence of detritus in cracks in the UK road network, to examine the method of their placement and to

investigate the distribution of detritus along a specimen's height and the gradation of detritus caught in cracks.

2. To develop a novel experiment and a calibrated model to investigate the potential of detritus in prevention of crack closure in freeze thaw cycling of a sample's temperature.
3. To develop a novel experiment and a calibrated model to investigate the effect of crack closure prevention on the rate of crack growth in top-down cracks induced by a sample in three-point bending. This is an approximate simulation of the tensile stresses, that are induced by a car tyre at the surface of an asphalt pavement, that cause top-down cracks to form and propagate.
4. To develop a novel experiment and a calibrated model to investigate the effect of detritus on the rate of crack growth when the crack is propagated by cyclically pressurised fluid. This is an approximate simulation of the mechanical pore water pressures, that are induced by a car tyre in the interconnected pores of a saturated pavement, that cause the cracks to propagate.

8.1 Conclusions

The Key conclusions of the various investigations conducted are as follows:

1. It is proven that there is dirt present in the cracks of roads in the UK road network. The crack widths of the surface course measured range between 2.7mm - 4.5mm on average, and approximately 60% - 70% of the crack volume in the surface course is occupied by detritus, in the scope of this experiment. As the pavement depth increases, the crack width interestingly increases, decreases, and eventually increases again, showing a 'w' shape. This suggests to the presence of different forms of cracking present in a pavement: top- down, bottom-up and a combination of the two as the pavement depth transitions from a region dominated by one to a region dominated by the other. At depths below the surface course, the volume

fraction filled with detritus reaches 100% with some occurrences of bridging. Also, when dirt was extracted from 10 asphalt cores, about 40g of detritus was obtained, which is on average 4g per pavement core. The gradation of the extracted detritus shows that 51% of the detritus is fine grained (i.e. < 0.125mm) and 49% is coarse grained. This is not a decisive result in determining the method of detritus placement, but it makes for a more informed hypothesis. From the results, it may be postulated that about half of the detritus is washed in by precipitation being fine, since fines are more easily transported in suspension. Conversely, the other half of the detritus in the crack may have been aggregates, stripped of their binder by water ingress, being coarser and being typically of a grain size greater than the average width of the crack.

2. It has been shown that detritus can prevent crack closure when the opening and closure of the crack is driven by thermal expansion and contraction of a sample subject to freeze thaw cycling. The novel experiment involved two halves of an asphalt sample glued to steel end plates and placed close together with 2.7mm distance between them in a watertight basin to simulate a fully formed crack in the surface course. In the experiment, the crack opens and closes by about 100 μm and two strains are measured: strain resulting from crack opening and strain resulting from crack closure. Out of four cases (Dry, Dry + Dirt, Water, Water + Dirt), Dry dirt of grain size 0.5mm managed to reduce the strain resulting from crack closure by 20% (from a projected 611 micro-strain to 480 micro-strain). The resulting 131 micro-strain is thermally induced internal stress borne by the adjacent asphalt. Water + Dirt does not have significant potential to prevent crack closure. To validate the test results, thermal models were developed involving thermal expansion and contraction coefficients, equations modelling the volumetric expansion of ice, isothermal viscoelastic flow of asphalt at standard temperature and pressure and detritus crack closure prevention.

3. It has been demonstrated that detritus can prevent crack closure when the opening and closure of the crack is driven by tensions at the top of the sample caused by simulated tyre loads and compression at the base of the sample returning it to rest by simulated underlying pavement layers. The novel experiment is an inverted three-point bending test with two points at the top of the sample causing tension. Beneath the sample is a third point load surrounded by cured rubber poured around it. When the two-point loads push down in each cycle, the rubber deforms. When the two points unload, the rubber returns to rest and the sample returns with it. Three cases are tested (Water, Dry, Dry + Dirt) and the Dry + Dirt shows a ratcheted increase of about 100 μm relative to the Dry for a given load of 1.65 kN. However, it is deduced that an increase in growth rate of crack width causes an increase in growth rate of crack length. A 1 mm change in crack width causes about a 4mm growth in crack length in the presence of dirt, whereas there is only about a 3mm change in the absence of it. Samples with dirt are also shown to fail in about 3000 cycles, whereas without dirt the samples fail in 3900 cycles on average. The influence of water in the test however is shown to have greater bearing than the influence of dirt in all metrics of crack length, crack width, load, and vertical displacement.

4. It has also been evidenced that detritus can prevent the relaxation of mastic asphalt blister surfaces and accelerate the rate of fluid driven crack propagation through an asphalt mastic. The novel experiment is an asphalt mastic poured around an injection needle in a bespoke mould such that the needle mouth is positioned in the centre of the mastic when it hardens. The top of the needle is then connected to a barrel which is filled with water and a plunger plate pushes the water into the sample, much like a syringe. In the tests carried out without dirt the sample fails in 5300 cycles. In the tests carried out with dirt the sample fails in 2500-4500 cycles, satisfying the objective. The dirt seemed to be deposited in the asphalt blister and formed a cake on the lining of the blister such that the geometry does not relax.

8.2 Future work

Even though the objectives have been met within the scope set out, the project did have some limitations which are in turn opportunities to further the research. Recommendations to further the research are outlined below.

8.2.1 Detritus in cores experiment

- For the measurement of crack widths and volumes, only one sample was used because of the pungent fumes emitted from a cut resin surface heated by the friction of the cutting blade. Perhaps having a fume extractor adjacent to the cutting apparatus may aid in this, and therefore allow more cuts of specimens to be made.
- For the detritus obtained from the cores that are graded, they may be subject to some elemental mapping or mineral liberation analysis technique in order to characterise their mineralogy.
- When obtaining the gradation of the detritus, detritus obtained per slice and hence depth should be sieved and graded separately in order to better quantify the more frequently occurring grain sizes with changes in depth.

8.2.2 Freeze thaw cycle experiment

- A constant width of 2.7mm was used for the duration of the test.
  Perhaps the width may be altered to increase the amount of trapped water in the crack and thus increase the volumetric expansion of ice.
- Also 0.5mm was used in experiments with detritus. Perhaps this may be expanded to other grain sizes.

8.2.3 Three-point bending experiment

- Because asphalt inherently varies significantly from sample to sample, a lot more tests should be carried out and the samples with the closest cluster of flexural stiffness should be chosen to be averaged. This seems the only

practical way of dealing with the variability of the asphalt samples. This was not possible due to time constraints, and a large amount of time was spent refining the methodology to a workable point.

- Different conditioning temperatures and temperatures of testing could be explored to observe how that influences the viscoelasticity of the sample.
- Different displacements and frequencies could also be explored.
- Different Shore hardness values of underlying rubber may be considered to increase or decrease the extent of crack opening and closing.
- Bigger notches and larger masses of detritus (larger than 1g) may also be explored.

8.2.4 Hydraulic fracturing

- Temperature control is imperative in this test. As a limitation of the testing apparatus available, temperature control was not available.
- 50% Asphalt mastic filler blends were used. Perhaps, more steps can be taken to incrementally move the material towards asphalt.
- 6% volume fraction of filler detritus was used. This can be varied.
- More repetitions of this test must be carried out. This was not possible due to time constraints, and a large amount of time was spent refining the methodology to a workable point.
- In the test, the filler was placed in the barrel. Perhaps it may be placed in the syringe such that all the dirt goes directly into the mastic asphalt blister.
- Different grain sizes of fine and coarse aggregates may be explored.
- Different loads and frequencies may be tested.
- The needle diameter may also be altered.
- Some modelling to characterise growth of the mastic asphalt blister should be considered e.g., to model the blister as a growing spherical cap.

References

1. Adachi, K. and Tainosho, Y. (2005). Single particle characterization of size-fractionated road sediments. *Applied Geochemistry*, 20(5), pp.849–859. doi:10.1016/j.apgeochem.2005.01.005.

2. Aguiar-Moya, J.P., Salazar-Delgado, J., Baldi-Sevilla, A., Leiva-Villacorta, F. and Loria-Salazar, L. (2015). Effect of Aging on Adhesion Properties of Asphalt Mixtures with the Use of Bitumen Bond Strength and Surface Energy Measurement Tests. *Transportation Research Record: Journal of the Transportation Research Board*, 2505(1), pp.57–65. doi:10.3141/2505-08.

3. Bessmertnykh, A., Dontsov, E. and Ballarini, R. (2020). The effects of proppant on the near-front behavior of a hydraulic fracture. *Engineering Fracture Mechanics*, 235, p.107110. doi:10.1016/j.engfracmech.2020.107110.

4. Bower, A.F. (2009). *Applied Mechanics of Solids*. CRC Press.

5. Chen, Z. (2013). An ABAQUS Implementation of the XFEM for Hydraulic Fracture Problems. *Effective and Sustainable Hydraulic Fracturing*. doi:10.5772/56287.

6. Croll, J.G.A. (2009). Possible role of thermal ratchetting in alligator cracking of asphalt pavements. *International Journal of Pavement Engineering*, 10(6), pp.447–453. doi:10.1080/10298430902730547.

7. Department for Transport (2012). Potholes review: Prevention and a better cure. [online] Available at: https://assets.publishing.service.gov.uk/government/uploads/system/uploads/attachment_data/file/3995/pothole-review.pdf.

8. Duojie, C., Si, W., Ma, B., Hu, Y., Liu, X. and Wang, X. (2021). Assessment of Freeze-Thaw Cycles Impact on Flexural Tensile Characteristics of Asphalt Mixture in Cold Regions. *Mathematical Problems in Engineering*, 2021, pp.1–10. doi:10.1155/2021/6697693.

9. Fan, Z., Xu, H., Xiao, J. and Tan, Y. (2020). Effects of freeze-thaw cycles on fatigue performance of asphalt mixture and development of fatigue-freeze-thaw (FFT) uniform equation. *Construction and Building Materials*, 242, p.118043. doi:10.1016/j.conbuildmat.2020.118043.

10. Gauthier, G. and Anderson, D.A. (2006). Fracture mechanics and asphalt binders. *Road Materials and Pavement Design*, 7(sup1), pp.9–35. doi:10.1080/14680629.2006.9690056.

11. GOV.UK. (2022). *Quarterly traffic estimates (TRA25)*. [online] Available at: https://www.gov.uk/government/statistical-data-sets/tra25-quarterly-estimates.

12. Islam, M.R. and Tarefder, R.A. (2015). Coefficients of Thermal Contraction and Expansion of Asphalt Concrete in the Laboratory. *Journal of Materials in Civil Engineering*, 27(11). doi:10.1061/(asce)mt.1943-5533.0001277.

13. Jackson, H. (2018). *THE ROLE OF SEDIMENTS IN FORMING FREEZE-THAW POTHOLES*.

14. Koch, C. and Brilakis, I. (2011). Pothole detection in asphalt pavement images. *Advanced Engineering Informatics*, 25(3), pp.507–515. doi:10.1016/j.aei.2011.01.002.

15. Kringos, N., Scarpas, T., Kasbergen, C. and Selvadurai, P. (2008). Modelling of combined physical–mechanical moisture-induced damage in asphaltic mixes, Part 1: governing processes and formulations. *International Journal of Pavement Engineering*, 9(2), pp.115–128. doi:10.1080/10298430701792185.

16. Lamothe, S., Perraton, D. and Di Benedetto, H. (2014). Contraction and expansion of partially saturated hot mix asphalt samples exposed to freeze–thaw cycles. *Road Materials and Pavement Design*, 16(2), pp.277–299. doi:10.1080/14680629.2014.990917.

17. Lampe, B. (2020). *Is Pothole Damage Really More Common During Winter Months?* [online] NAPA Know How Blog. Available at: https://knowhow.napaonline.com/is-pothole-damage-really-more-common-

during-winter-months/ [Accessed 3 Nov. 2022].

18. Liu, J., Sun, Y., Wang, W. and Chen, J. (2017). Using the viscoelastic parameters to estimate the glass transition temperature of asphalt binders. *Construction and Building Materials*, 153, pp.908–917. doi:10.1016/j.conbuildmat.2017.07.120.

19. López-Montero, T. and Miró, R. (2017). Ageing and temperature effect on the fatigue performance of bituminous mixtures. *Materiales de Construcción*, 7(080), p.126. doi:10.3989/mc.2017.04216.

20. Ma, Y., Chen, X., Geng, Y. and Zhang, X. (2020). Effect of Clogging on the Permeability of Porous Asphalt Pavement. *Advances in Materials Science and Engineering*, 2020, pp.1–9. doi:10.1155/2020/4851291.

21. Maggiore, C. (2014). *A comparison of different test and analysis methods for asphalt fatigue.*.

22. Mahmud, M.Z.H., Hassan, N.A., Hainin, M.R., Ismail, C.R., Jaya, R.P., Warid, M.N.M., Yaacob, H. and Mashros, N. (2021). Characterisation of microstructural and sound absorption properties of porous asphalt subjected to progressive clogging. *Construction and Building Materials*, 283, p.122654. doi:10.1016/j.conbuildmat.2021.122654.

23. McCormack, T. (2020). *Tarmacadam, Bitmac and Asphalt*. [online] www.pavingexpert.com. Available at: https://www.pavingexpert.com/tarmac01.

24. McSweeney, R.T., Tomlinson, J.E., Darch, G.J.C., Parker, J. and Holland, T. (2016). Impacts of climate change on marginal nights for road salting. *Proceedings of the Institution of Civil Engineers - Transport*, 169(2), pp.65–75. doi:10.1680/jtran.14.00037.

25. Northern Ireland Executive. (2021). *The Northern Ireland Transport Statistics 2020-2021 statistical report has been published today*. [online] Available at: https://www.northernireland.gov.uk/news/northern-ireland-transport-statistics-2020-2021-statistical-report-has-been-published-today.

26. O'Keeffe, N.J., Huppert, H.E. and Linden, P.F. (2018). Experimental exploration of fluid-driven cracks in brittle hydrogels. *Journal of Fluid Mechanics*, 844, pp.435–458. doi:10.1017/jfm.2018.203.

27. Olard, F., Di Benedetto, H., Dony, A. and Vaniscote, J.-C. . (2005). Properties of bituminous mixtures at low temperatures and relations with binder characteristics. *Materials and Structures*, 38(1), pp.121–126. doi:10.1007/bf02480584.

28. Owens, P.N., Caley, K.A., Campbell, S., Koiter, A.J., Droppo, I.G. and Taylor, K.G. (2011). Total and size-fractionated mass of road-deposited sediment in the city of Prince George, British Columbia, Canada: implications for air and water quality in an urban environment. *Journal of Soils and Sediments*, 11(6), pp.1040–1051. doi:10.1007/s11368-011-0383-y.

29. Pflanzer, L.R.P., Lydia Ramsey (2015). *Is It OK To Eat Snow?* [online] Business Insider. Available at: https://www.businessinsider.com/is-it-ok-to-eat-snow-2015-1?r=US&IR=T.

30. Portillo, O. and Cebon, D. (2014). Fracture mechanics of idealised bituminous mixes. *International Journal of Pavement Engineering*, 17(2), pp.103–122. doi:10.1080/10298436.2014.925556.

31. Saeed, F., Rahman, M., Chamberlain, D. and Collins, P. (2019). Asphalt surface damage due to combined action of water and dynamic loading. *Construction and Building Materials*, 196, pp.530–538. doi:10.1016/j.conbuildmat.2018.10.225.

32. Scott, M. (2013). *Dusting the Virtues of Snow*. [online] earthobservatory.nasa.gov. Available at: https://earthobservatory.nasa.gov/features/DirtySnow.

33. Seleznev, A., Yarmoshenko, I., Malinovsky, G., Ilgasheva, E., Baglaeva, E., Ryanskaya, A., Kiseleva, D. and Gulyaeva, T. (2019). Snow-dirt sludge as an indicator of environmental and sedimentation processes in the urban environment. *Scientific Reports*, 9(1). doi:10.1038/s41598-019-53793-z.

34. Shah, P. (2020). *Potholes on UK roads in 2030 - Cebr forecasts*. [online] Available at: https://www.zurich.co.uk/-/media/media-centre/docs/potholes_cebr_report.pdf [Accessed 8 Nov. 2022].

35. Si, W., Li, N., Ma, B., Ren, J., Wang, H. and Hu, J. (2015). Impact of freeze-thaw cycles on compressive characteristics of asphalt mixture in cold regions. *Journal of Wuhan University of Technology-Mater. Sci. Ed.*, 30(4), pp.703–709. doi:10.1007/s11595-015-1215-5.

36. Smooth-On, Inc. (2019). *Durometer Shore Hardness Scale*. [online] Available at: https://www.smooth-on.com/page/durometer-shore-hardness-scale/.

37. Sun, L., Wang, G., Zhang, H. and Liu, L. (2018). Initiation and Propagation of Top-Down Cracking in Asphalt Pavement. *Applied Sciences*, 8(5), p.774. doi:10.3390/app8050774.

38. Sun, Y., Guo, R., Gao, L., Wang, J., Wang, X. and Yuan, X. (2019). Study on Dynamic Response Characteristics of Saturated Asphalt Pavement under Multi-Field Coupling. *Materials*, 12(6), p.959. doi:10.3390/ma12060959.

39. Thom, N. (2014). *Principles of pavement engineering*. London: Ice Publishing.

40. Vu, V.T., Chupin, O., Piau, J.-M., Hammoum, F. and Bouron, S. (2018). Experimental study and modeling of the behavior of partially saturated asphalt concrete under freezing condition. *Construction and Building Materials*, 163, pp.169–178. doi:10.1016/j.conbuildmat.2017.12.070.

41. Wang, H. and Sharma, M.M. (2018). Modeling of hydraulic fracture closure on proppants with proppant settling. *Journal of Petroleum Science and Engineering*, 171, pp.636–645. doi:10.1016/j.petrol.2018.07.067.

42. www.weatheronline.co.uk. (n.d.). *weather forecast Europe - WeatherOnline*. [online] Available at: https://www.weatheronline.co.uk/weather/maps/city?FMM=8&FYY=200 [Accessed 8 Nov. 2022].

43. Xu, H., Guo, W. and Tan, Y. (2015). Internal structure evolution of asphalt mixtures during freeze–thaw cycles. *Materials & Design*, 86, pp.436–446.

doi:10.1016/j.matdes.2015.07.073.

44. Xu, H., Guo, W. and Tan, Y. (2016). Permeability of asphalt mixtures exposed to freeze–thaw cycles. *Cold Regions Science and Technology*, 123, pp.99–106. doi:10.1016/j.coldregions.2015.12.001.

45. Yilmaz, A. and Karahancer, S. (2012). Water Effect on Deteriorations of Asphalt Pavements. *The Online Journal of Science and Technology*, 2(1).

46. Yin, Y.M. (2012). Fatigue Experiments of Simulating Propagating Process of Reflective Cracking in Asphalt Concrete Overlays. *Applied Mechanics and Materials*, 193-194, pp.1454–1460. doi:10.4028/www.scientific.net/amm.193-194.1454.

Appendix

Below are the manufactured drawings with dimensions of the bespoke equipment for the Three-point bending and Hydraulic fracturing rigs.

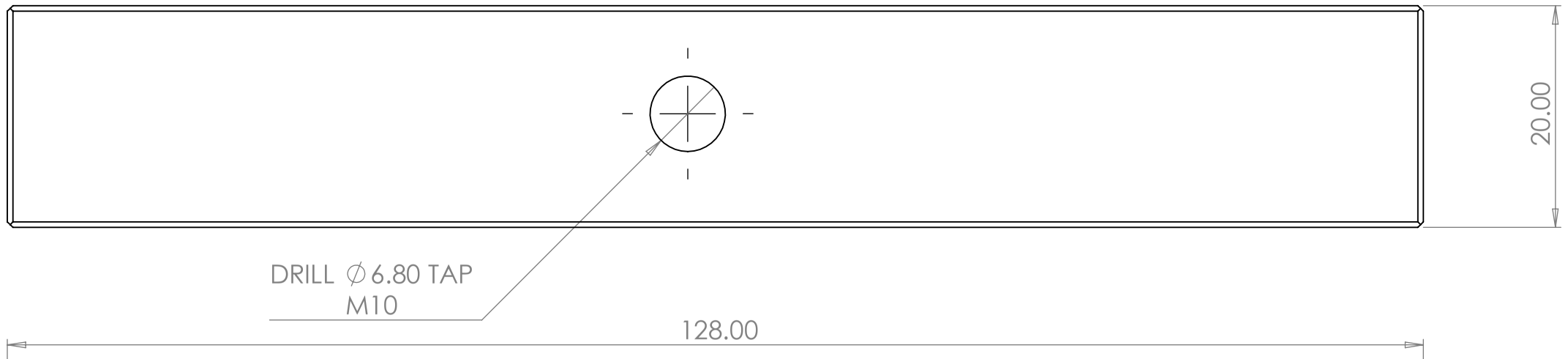

UNLESS OTHERWISE SPECIFIED: DIMENSIONS ARE IN MILLIMETERS SURFACE FINISH: TOLERANCES: LINEAR: ANGULAR:		FINISH:		DEBURR AND BREAK SHARP EDGES		DO NOT SCALE DRAWING	REVISION
	NAME	SIGNATURE	DATE			TITLE:	
DRAWN							
CHK'D							
APPV'D							
MFG							
Q.A				MATERIAL:		DWG NO. 001	A3
				WEIGHT:		SCALE:2:1	SHEET 1 OF 1

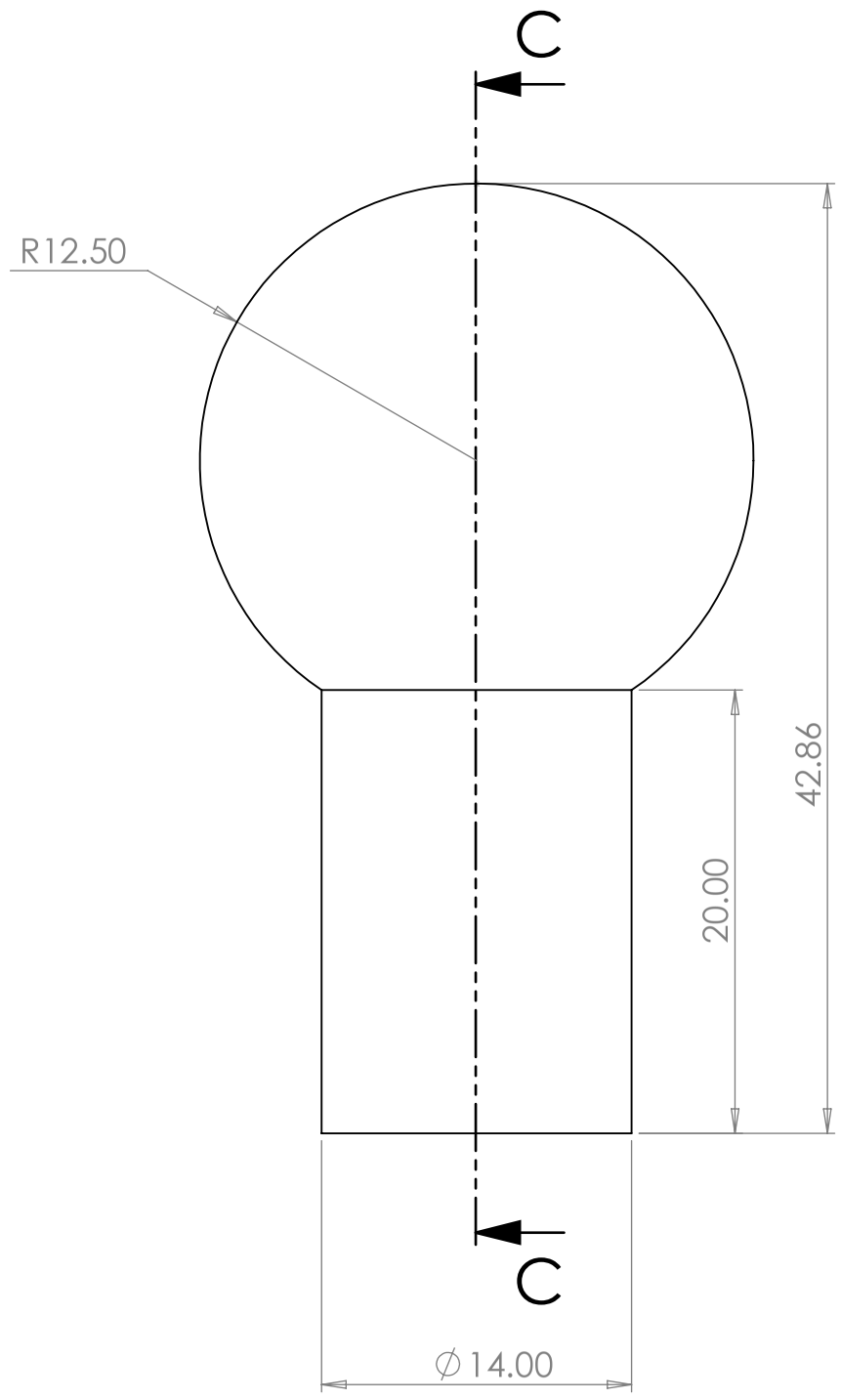

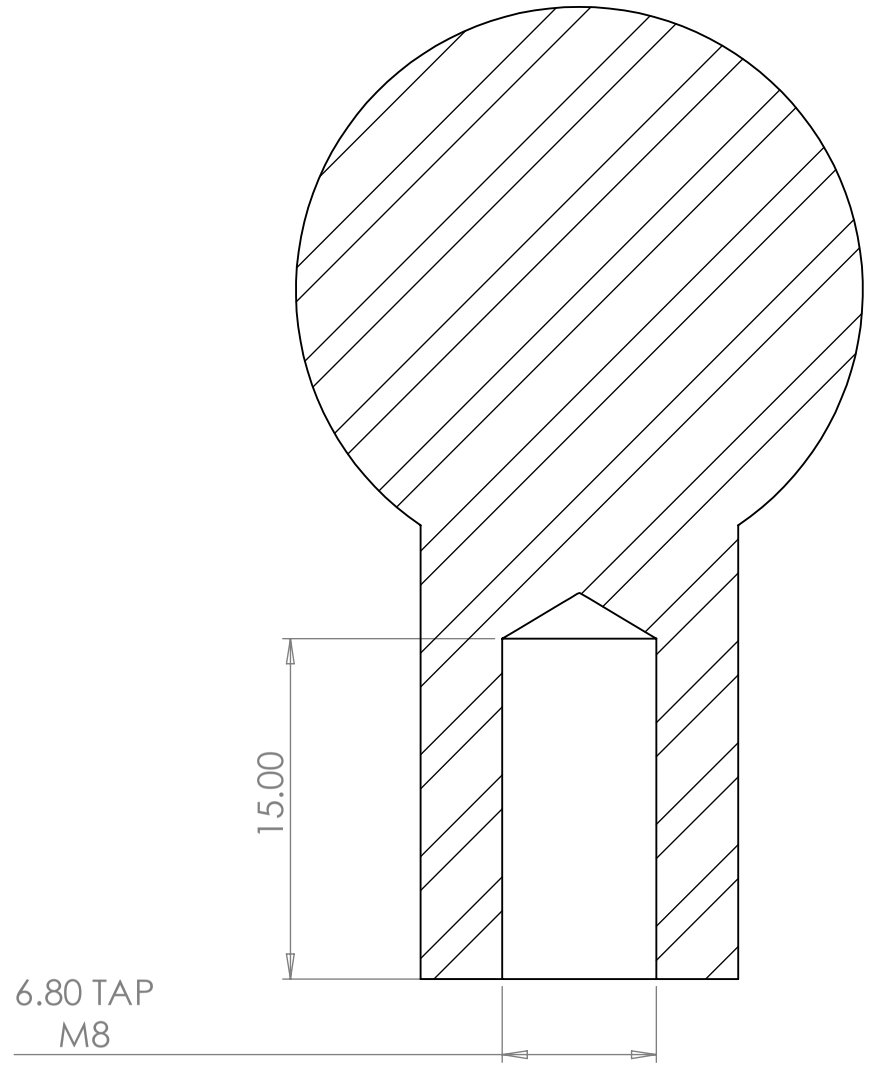

SECTION C-C

UNLESS OTHERWISE SPECIFIED: DIMENSIONS ARE IN MILLIMETERS SURFACE FINISH: TOLERANCES: LINEAR: ANGULAR:		FINISH:			DEBURR AND BREAK SHARP EDGES	DO NOT SCALE DRAWING	REVISION
	NAME	SIGNATURE	DATE			TITLE: LOAD ROD	
DRAWN							
CHK'D							
APPV'D							
MFG							
Q.A				MATERIAL: STAINLESS STEEL		DWG NO. 002	A3
				WEIGHT:		SCALE:3:1	SHEET 1 OF 1

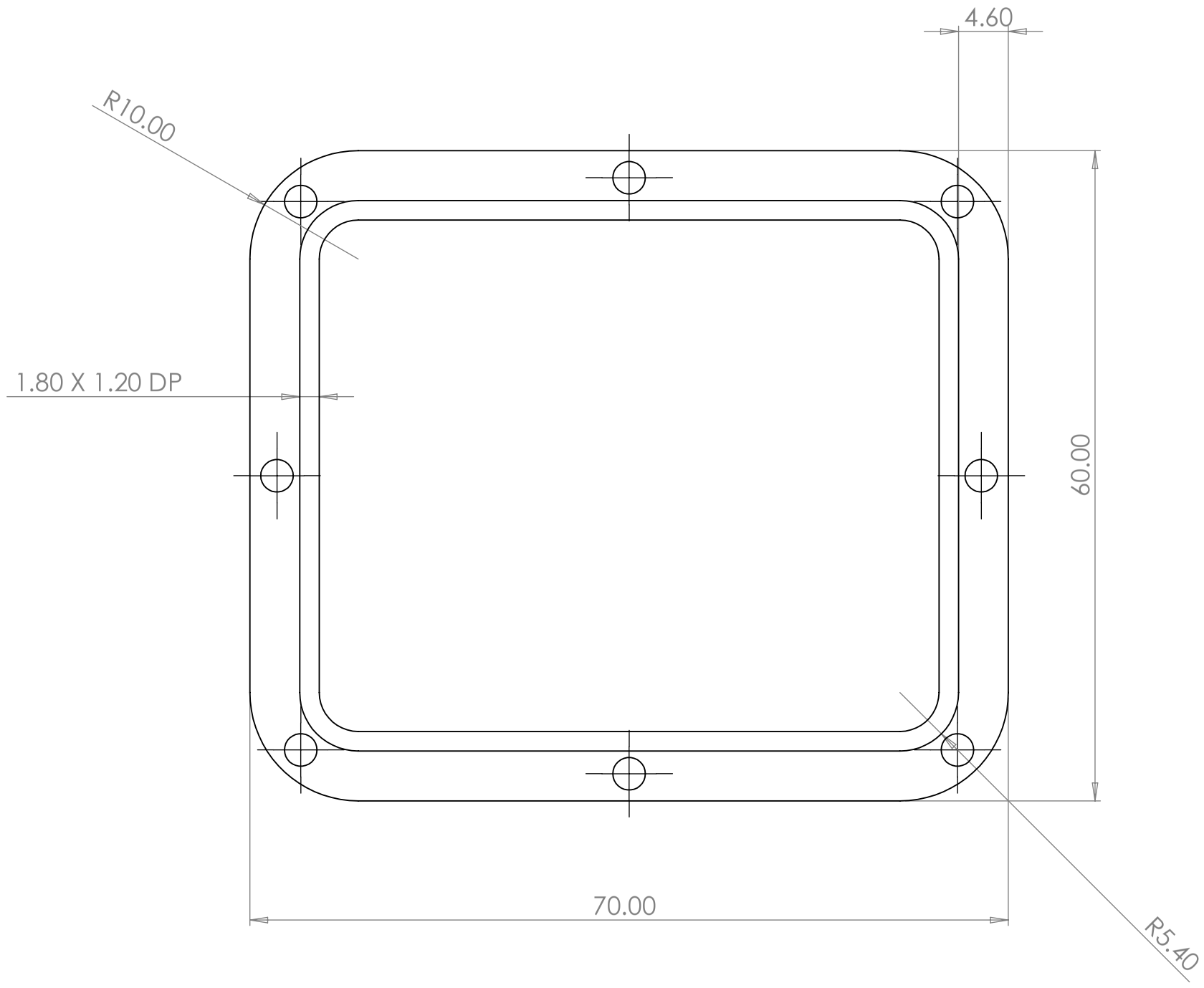

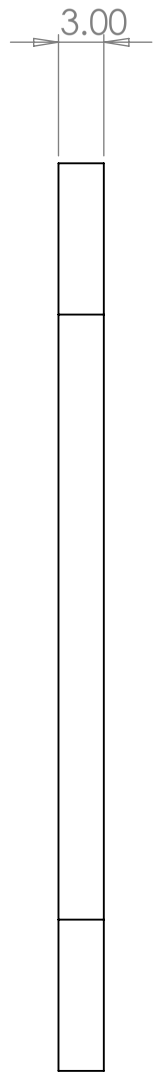

UNLESS OTHERWISE SPECIFIED: DIMENSIONS ARE IN MILLIMETERS SURFACE FINISH: TOLERANCES: LINEAR: ANGULAR:		FINISH:			DEBURR AND BREAK SHARP EDGES	DO NOT SCALE DRAWING	REVISION
	NAME	SIGNATURE	DATE			TITLE:	
DRAWN							
CHK'D							
APPV'D							
MFG							
Q.A				MATERIAL:		DWG NO. 003	A3
				WEIGHT:		SCALE:2:1	SHEET 1 OF 2

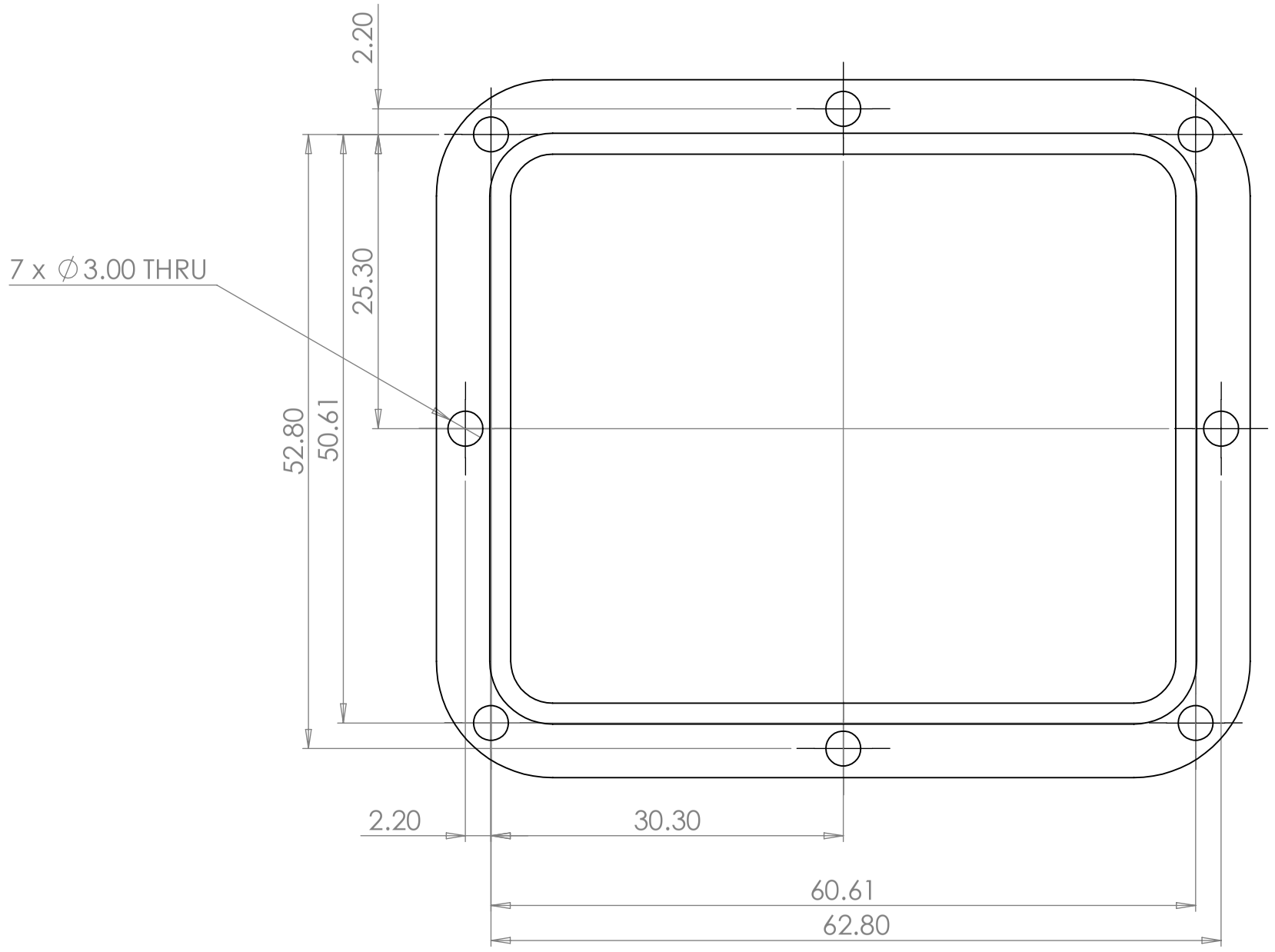

UNLESS OTHERWISE SPECIFIED: DIMENSIONS ARE IN MILLIMETERS SURFACE FINISH: TOLERANCES: LINEAR: ANGULAR:		FINISH:		DEBURR AND BREAK SHARP EDGES		DO NOT SCALE DRAWING	REVISION
	NAME	SIGNATURE	DATE			TITLE:	
DRAWN							
CHK'D							
APPV'D							
MFG							
Q.A				MATERIAL:		DWG NO. 003	A3
				WEIGHT:		SCALE:2:1	SHEET 2 OF 2

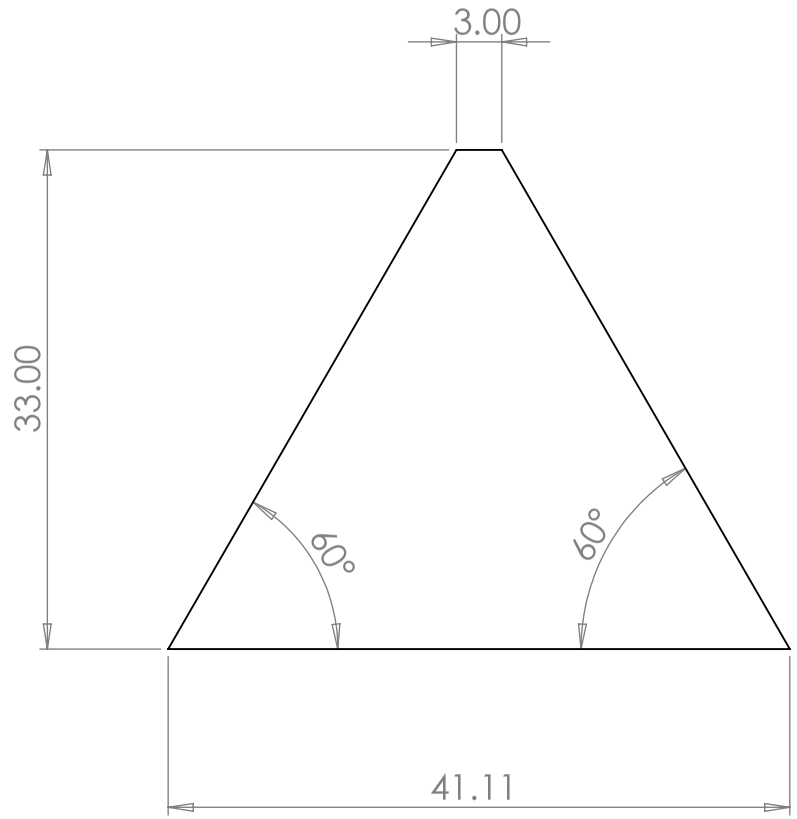

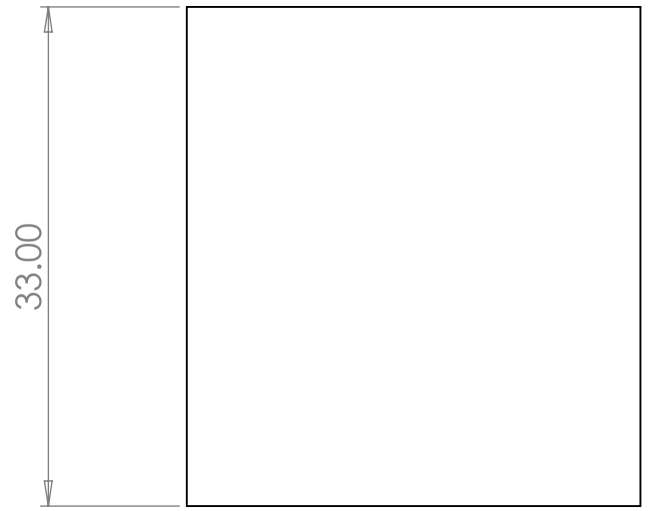

UNLESS OTHERWISE SPECIFIED: DIMENSIONS ARE IN MILLIMETERS SURFACE FINISH: TOLERANCES: LINEAR: ANGULAR:	FINISH:			DEBURR AND BREAK SHARP EDGES	DO NOT SCALE DRAWING	REVISION
	NAME	SIGNATURE	DATE		TITLE: SUPPORT	
DRAWN						
CHK'D						
APPV'D						
MFG						
Q.A				MATERIAL: STAINLESS STEEL	DWG NO. 004	A3
				WEIGHT:	SCALE:2:1	SHEET 1 OF 1

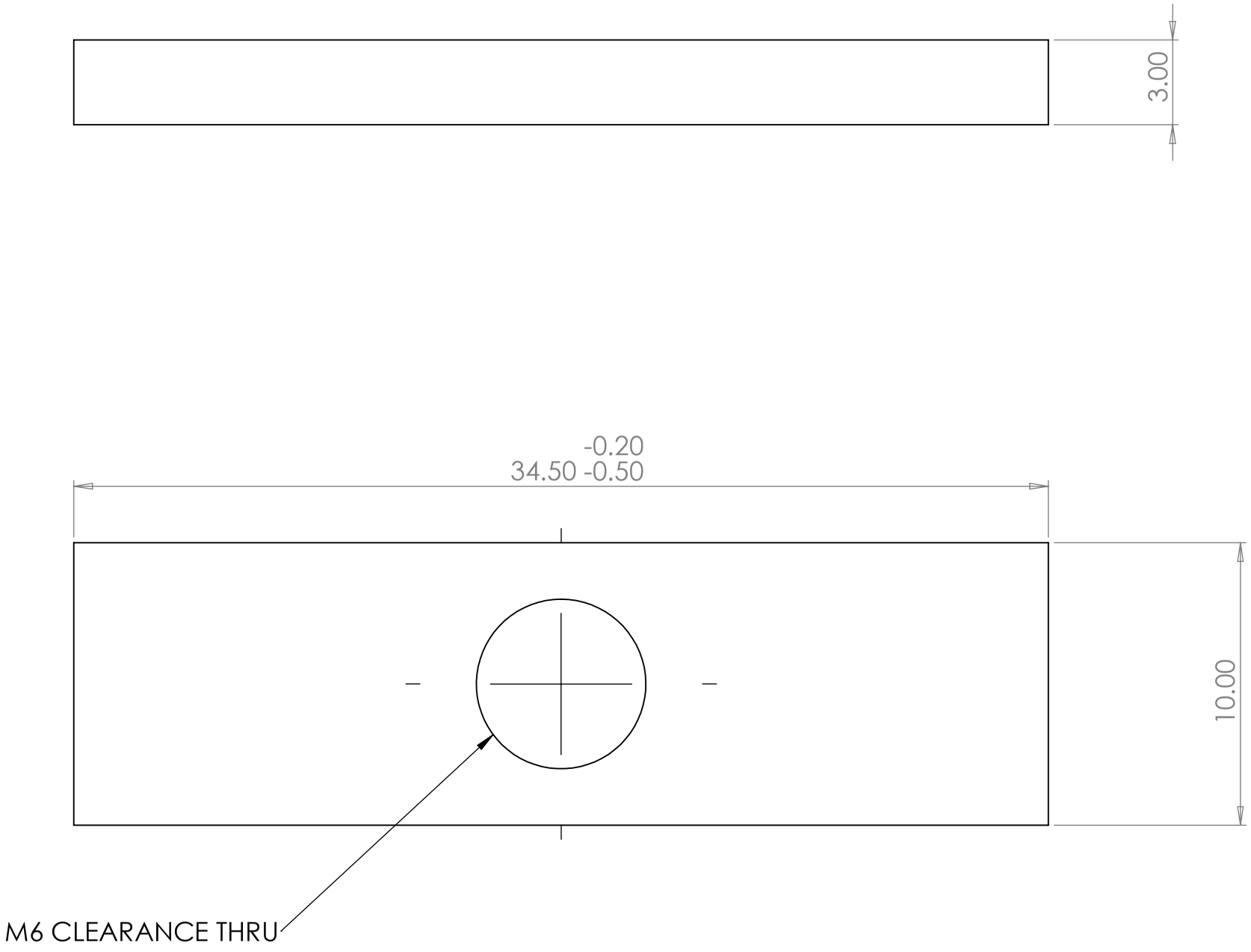

UNLESS OTHERWISE SPECIFIED: DIMENSIONS ARE IN MILLIMETERS SURFACE FINISH: TOLERANCES: LINEAR: ANGULAR:	FINISH:				DEBURR AND BREAK SHARP EDGES	DO NOT SCALE DRAWING	REVISION
	NAME	SIGNATURE	DATE			TITLE: RUBBER CLAMP	
DRAWN							
CHK'D							
APPV'D							
MFG							
Q.A				MATERIAL: STAINLESS STEEL		DWG NO. 005	A3
				WEIGHT:		SCALE:5:1	SHEET 1 OF 1

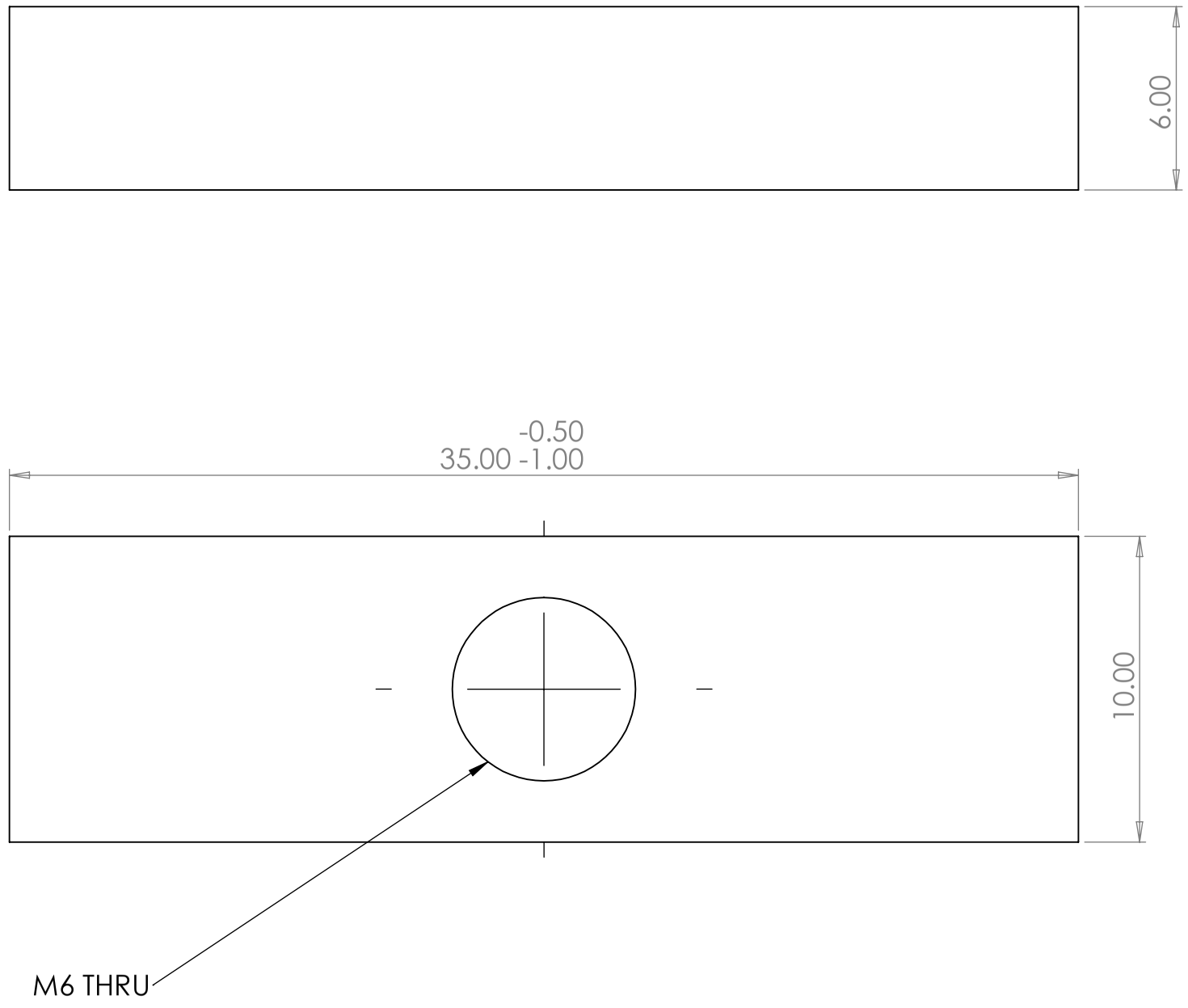

UNLESS OTHERWISE SPECIFIED: DIMENSIONS ARE IN MILLIMETERS SURFACE FINISH: TOLERANCES: LINEAR: ANGULAR:		FINISH:			DEBURR AND BREAK SHARP EDGES	DO NOT SCALE DRAWING	REVISION
	NAME	SIGNATURE	DATE			TITLE: RUBBER MOUNTING PLATE	
DRAWN							
CHK'D							
APPV'D							
MFG							
Q.A				MATERIAL: STAINLESS STEEL		DWG NO. 006	A3
				WEIGHT:		SCALE:5:1	SHEET 1 OF 1

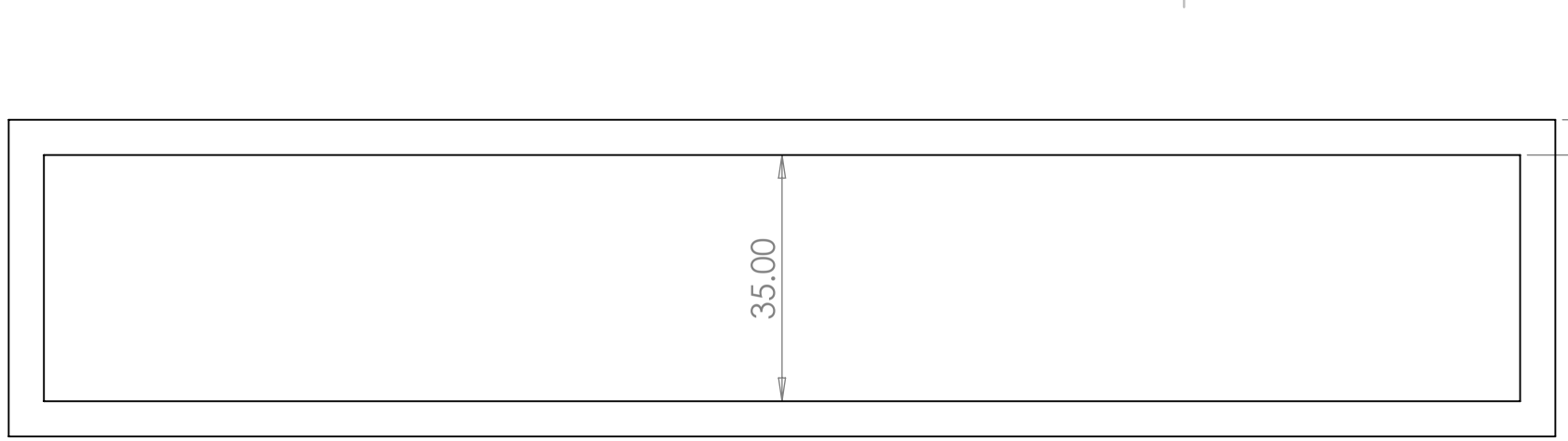

VIEW A

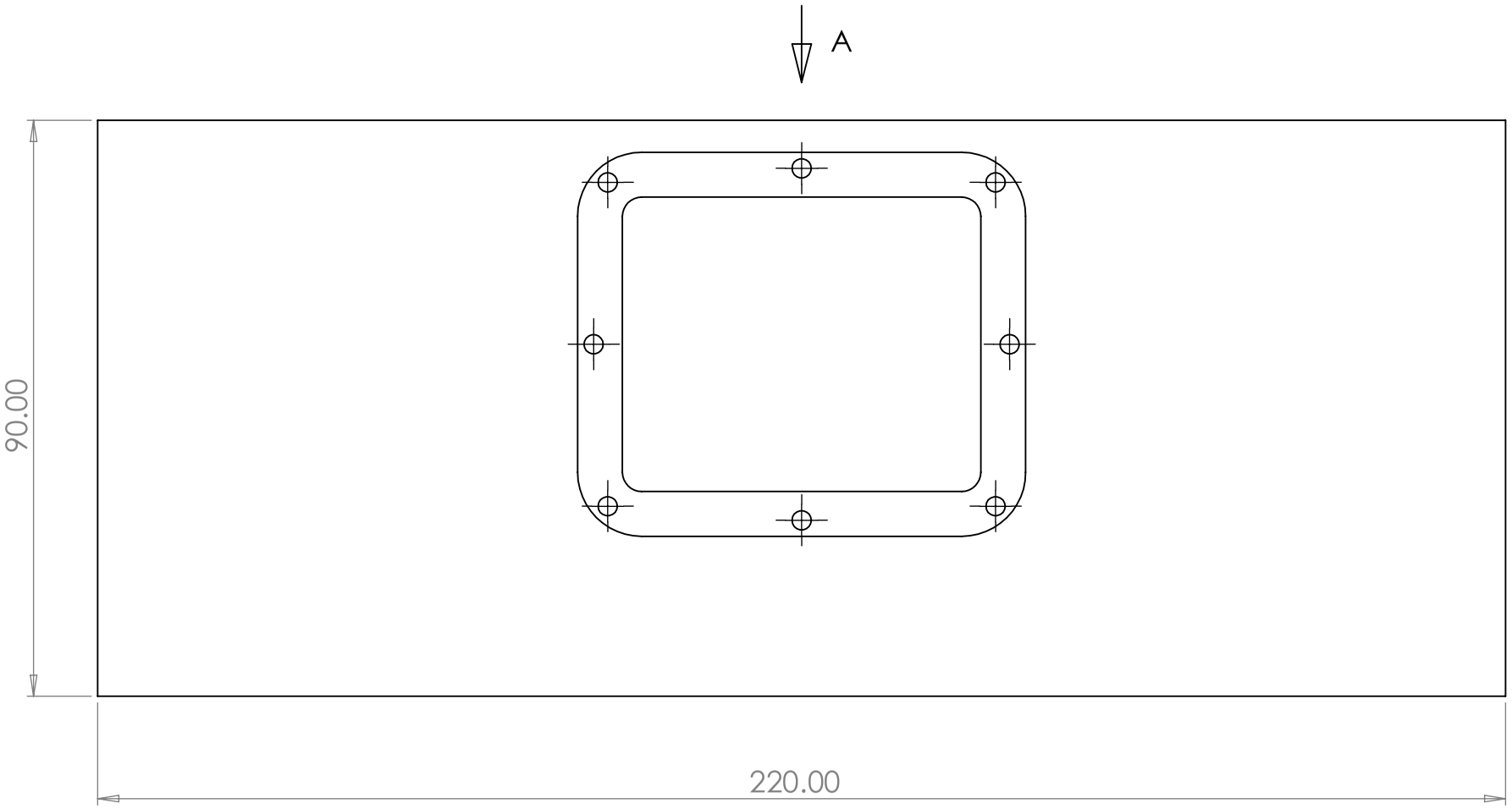

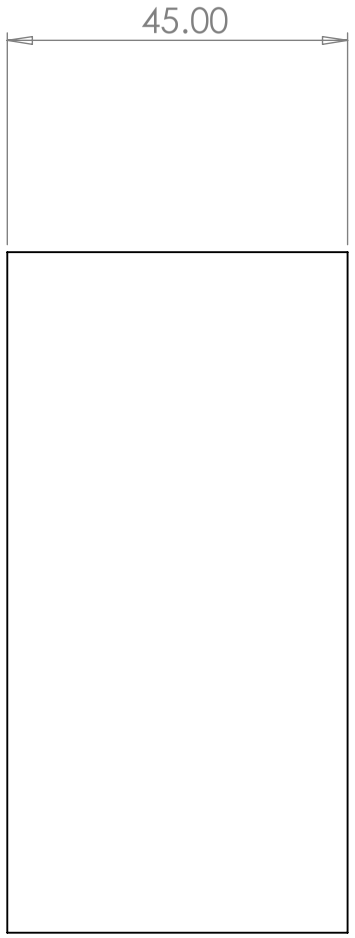

UNLESS OTHERWISE SPECIFIED: DIMENSIONS ARE IN MILLIMETERS SURFACE FINISH: TOLERANCES: LINEAR: ANGULAR:		FINISH:		DEBURR AND BREAK SHARP EDGES		DO NOT SCALE DRAWING	REVISION
	NAME	SIGNATURE	DATE			TITLE: BASIN	
DRAWN							
CHK'D							
APPV'D							
MFG							
Q.A				MATERIAL: STAINLESS STEEL		DWG NO. 007	A3
				WEIGHT:		SCALE:1:1	SHEET 1 OF 4

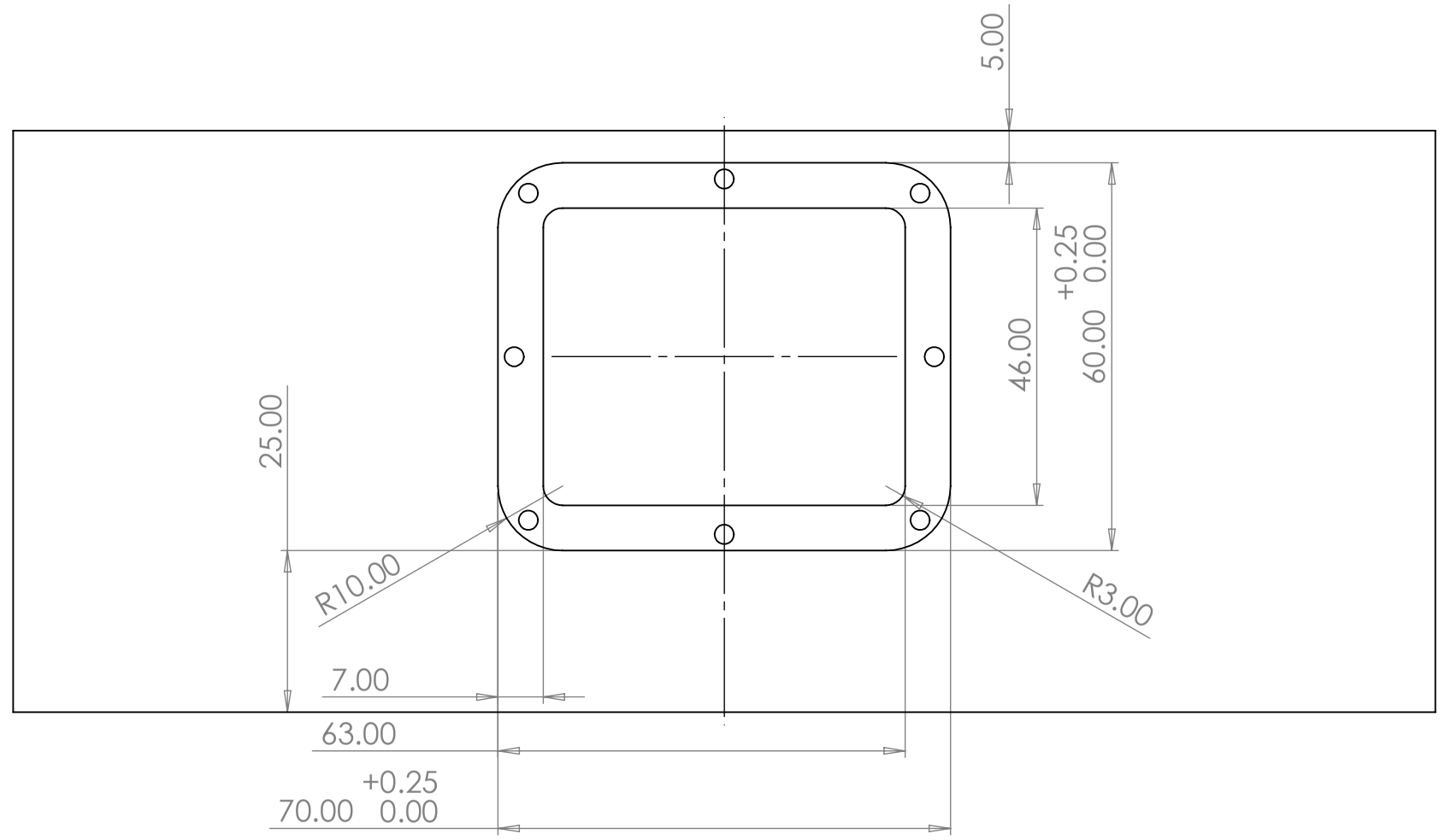

UNLESS OTHERWISE SPECIFIED: DIMENSIONS ARE IN MILLIMETERS SURFACE FINISH: TOLERANCES: LINEAR: ANGULAR:		FINISH:			DEBURR AND BREAK SHARP EDGES	DO NOT SCALE DRAWING	REVISION
	NAME	SIGNATURE	DATE			TITLE: BASIN WINDOW POCKET	
DRAWN							
CHK'D							
APPV'D							
MFG							
Q.A				MATERIAL:		DWG NO. 007	A3
				WEIGHT:		SCALE:1:1	SHEET 2 OF 4

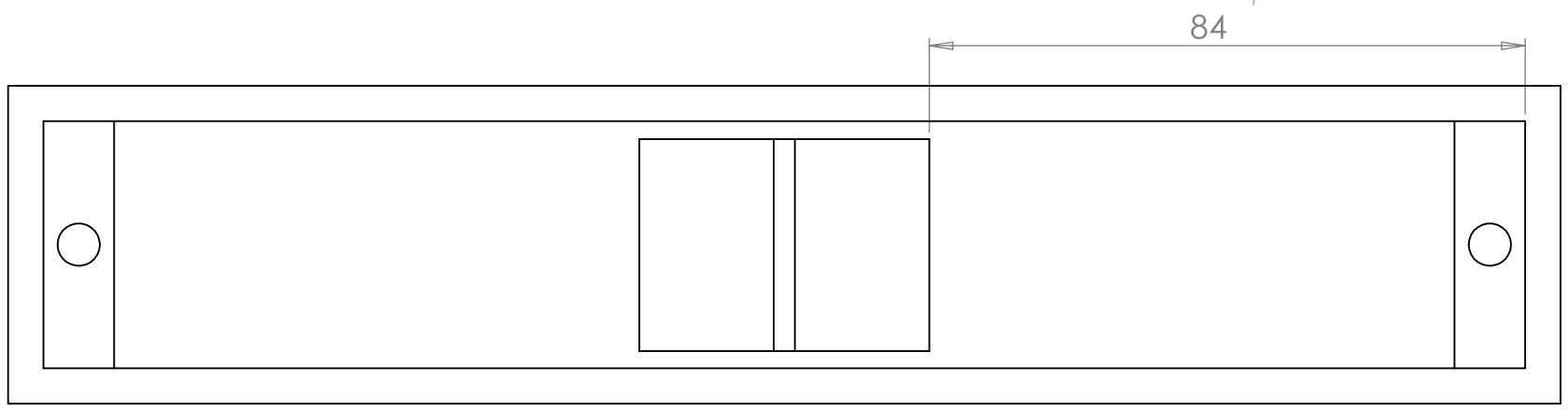

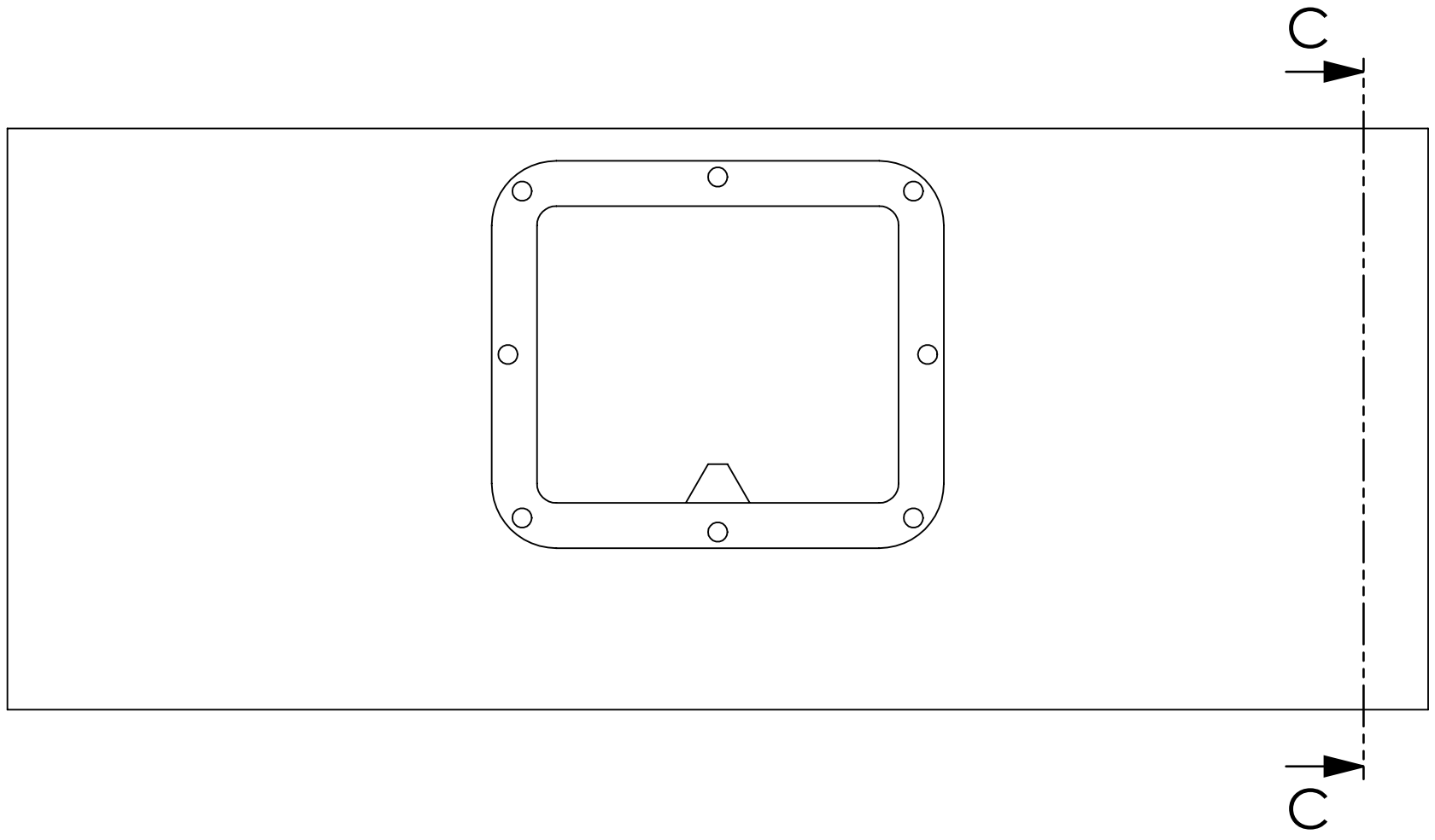

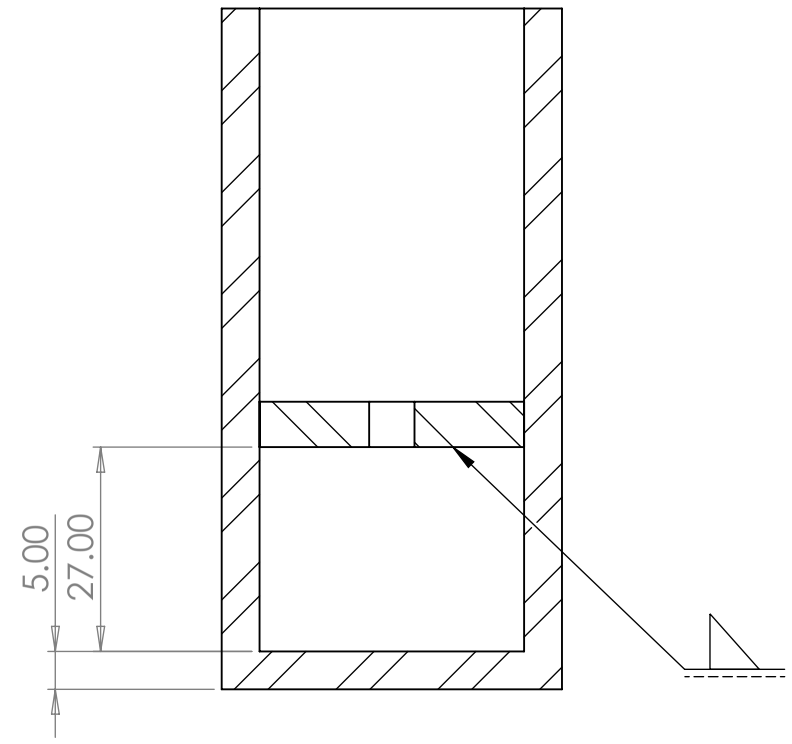

SECTION C-C

UNLESS OTHERWISE SPECIFIED: DIMENSIONS ARE IN MILLIMETERS SURFACE FINISH: TOLERANCES: LINEAR: ANGULAR:		FINISH:		DEBURR AND BREAK SHARP EDGES		DO NOT SCALE DRAWING	REVISION
	NAME	SIGNATURE	DATE			TITLE:	
DRAWN							
CHK'D							
APPV'D							
MFG							
Q.A				MATERIAL:		DWG NO. 007	A3
				WEIGHT:		SCALE:1:1	SHEET 3 OF 4

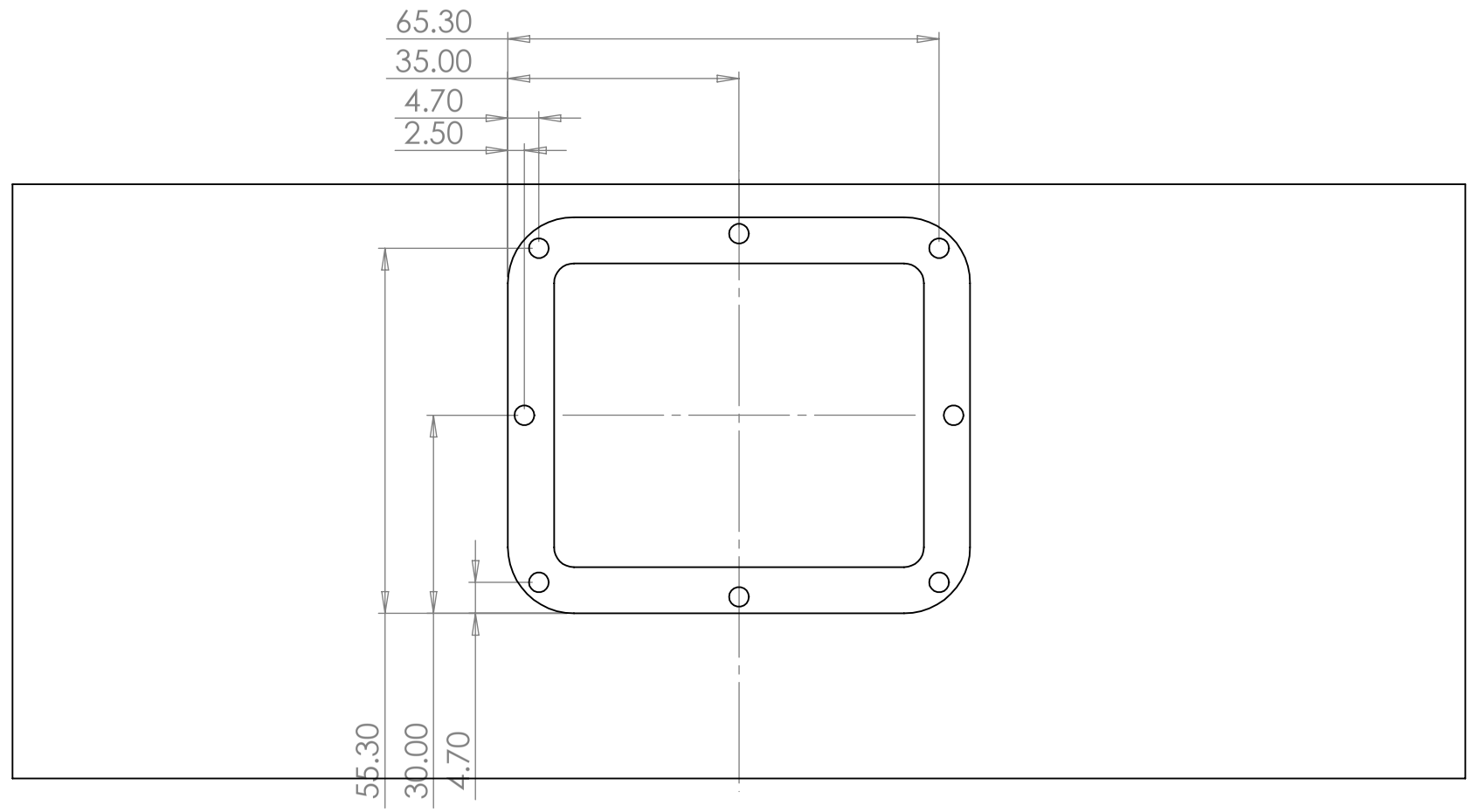

UNLESS OTHERWISE SPECIFIED: DIMENSIONS ARE IN MILLIMETERS SURFACE FINISH: TOLERANCES: LINEAR: ANGULAR:		FINISH:			DEBURR AND BREAK SHARP EDGES	DO NOT SCALE DRAWING	REVISION
	NAME	SIGNATURE	DATE			TITLE:	
DRAWN							
CHK'D							
APPV'D							
MFG							
Q.A				MATERIAL:		DWG NO. 007	A3
				WEIGHT:		SCALE:1:1	SHEET 4 OF 4

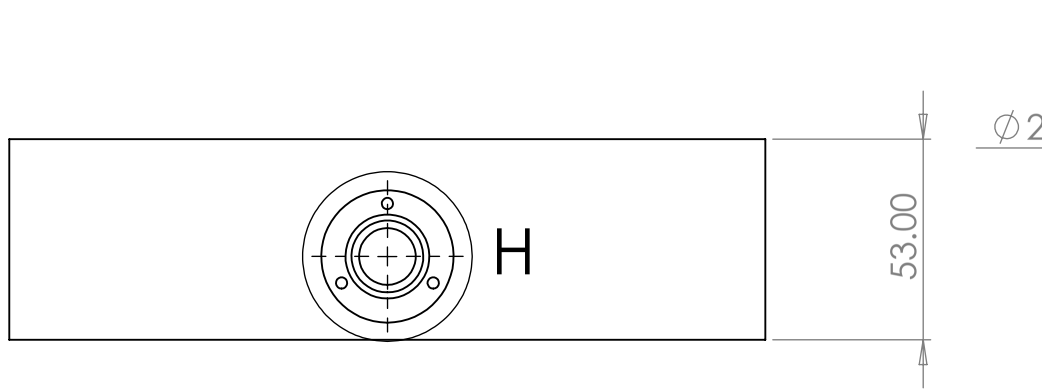

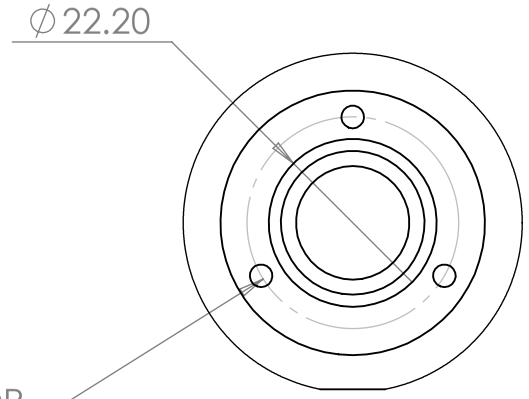

DETAIL H

SCALE 1 : 1

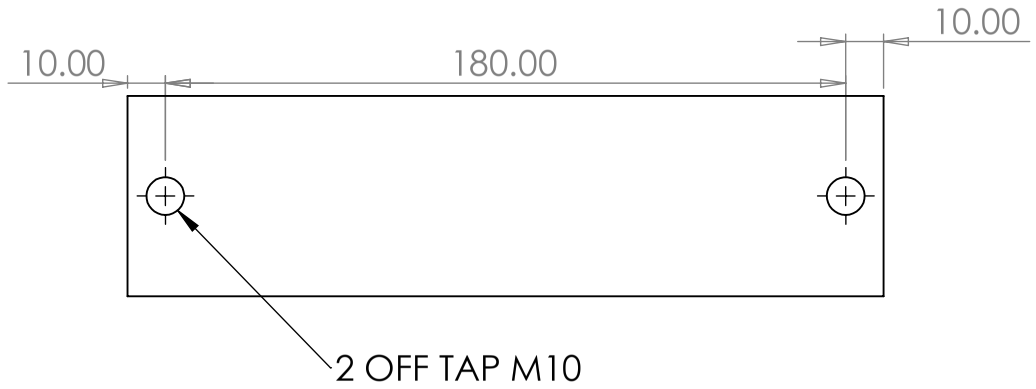

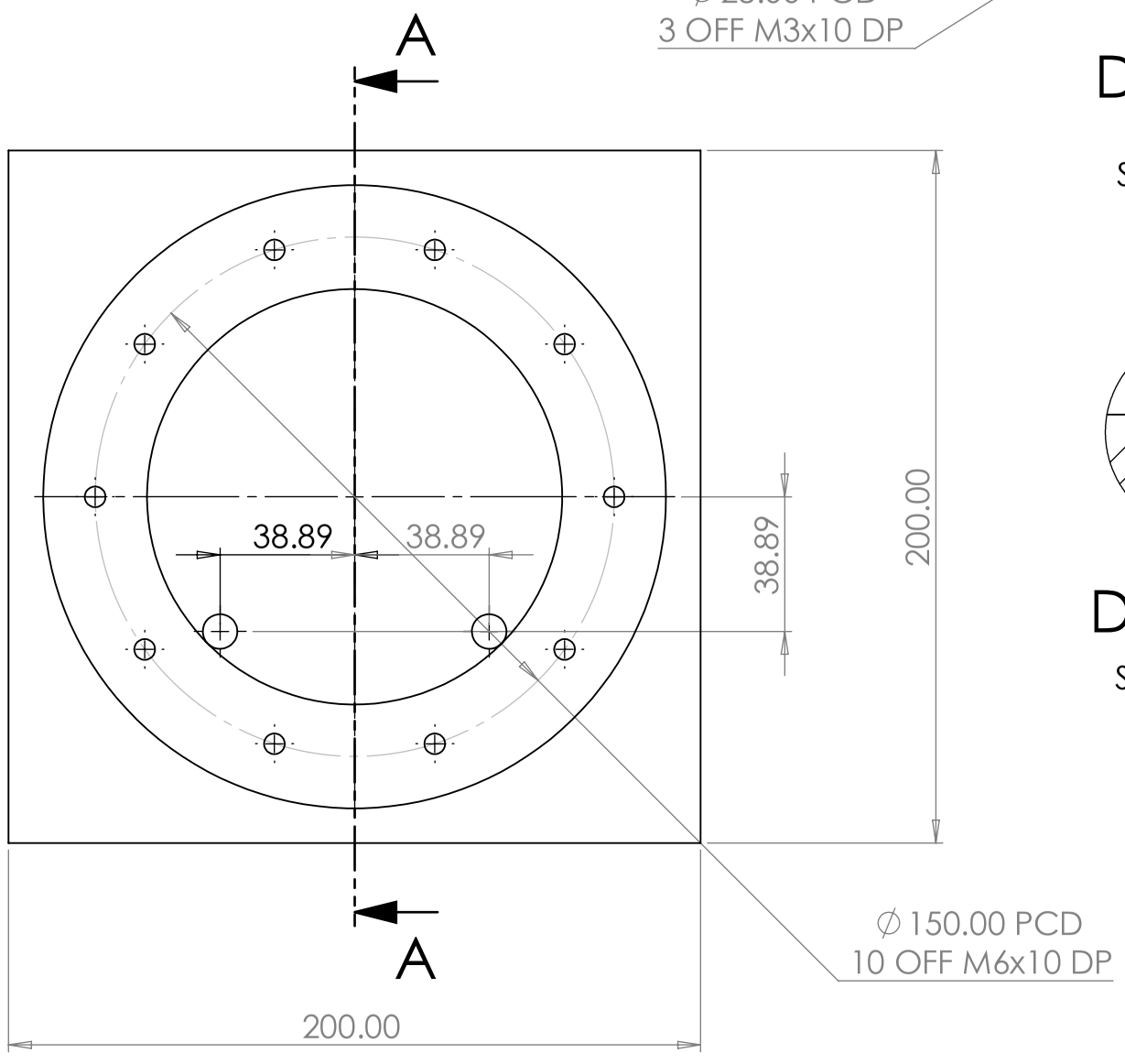

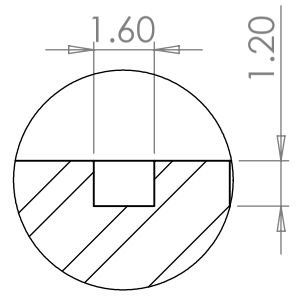

DETAIL G

SCALE 5 : 1

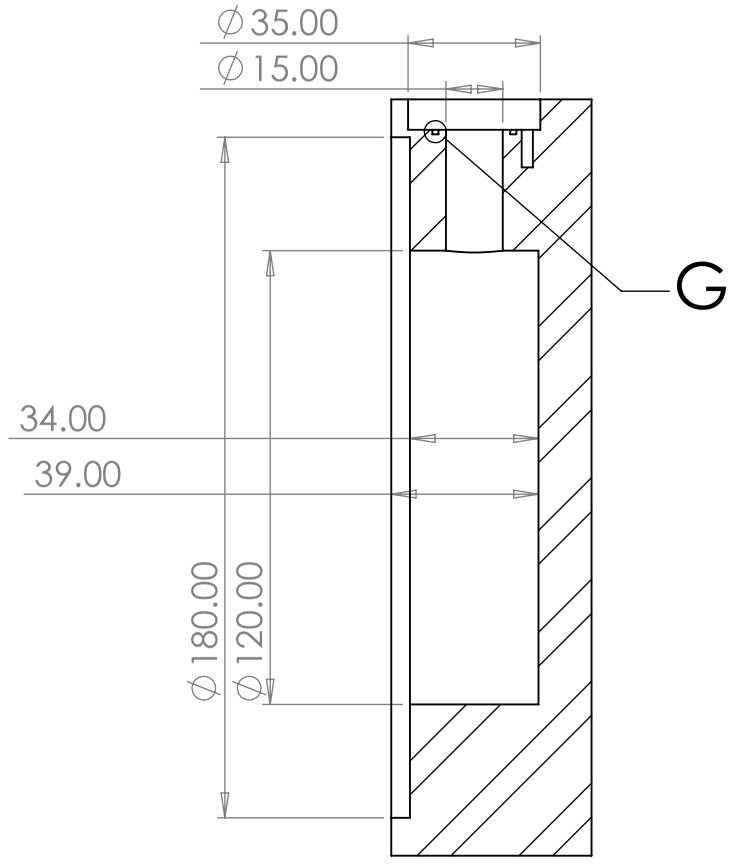

SECTION A-A

UNLESS OTHERWISE SPECIFIED: DIMENSIONS ARE IN MILLIMETERS SURFACE FINISH: TOLERANCES: LINEAR: ANGULAR:		FINISH:		DEBURR AND BREAK SHARP EDGES		DO NOT SCALE DRAWING	REVISION
	NAME	SIGNATURE	DATE			TITLE: CHAMBER	
DRAWN							
CHK'D							
APPV'D							
MFG							
Q.A				MATERIAL: STAINLESS STEEL		DWG NO. 001	A3
				WEIGHT:		SCALE:1:2	SHEET 1 OF 1

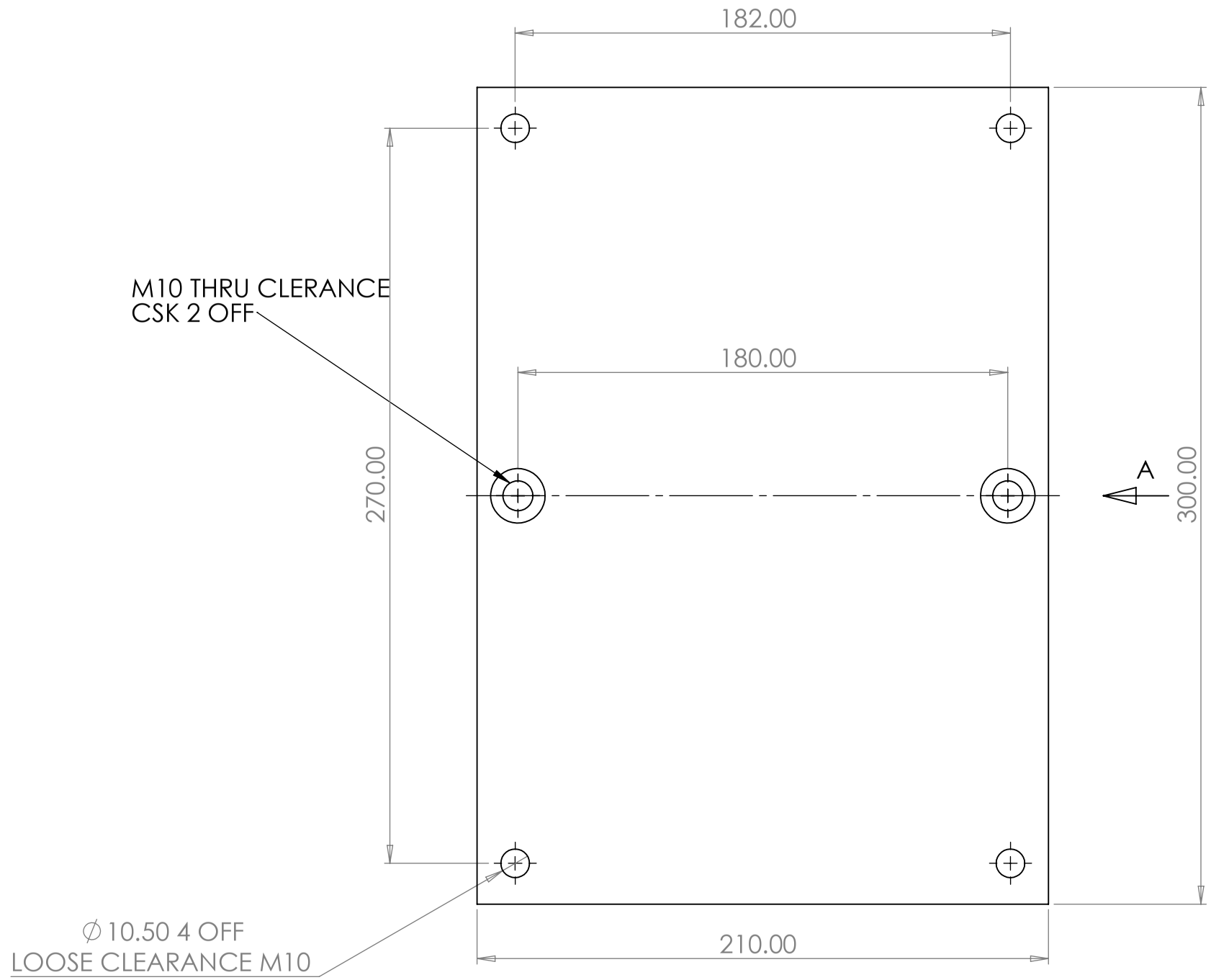

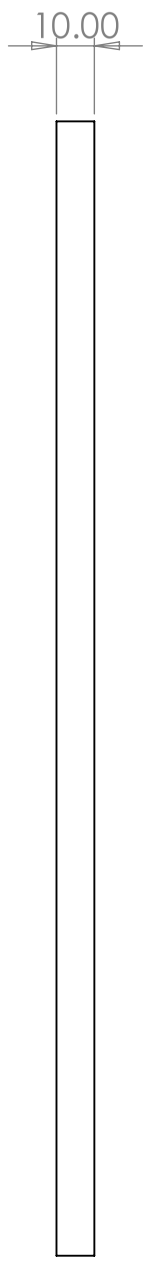

VIEW A

UNLESS OTHERWISE SPECIFIED: DIMENSIONS ARE IN MILLIMETERS SURFACE FINISH: TOLERANCES: LINEAR: ANGULAR:	FINISH:		DEBURR AND BREAK SHARP EDGES	DO NOT SCALE DRAWING	REVISION		
	NAME	SIGNATURE	DATE	TITLE:			
DRAWN							
CHK'D							
APPV'D							
MFG							
Q.A				MATERIAL: ALUMINIUM		DWG NO. 002	A3
				WEIGHT:		SCALE:1:2	SHEET 1 OF 1

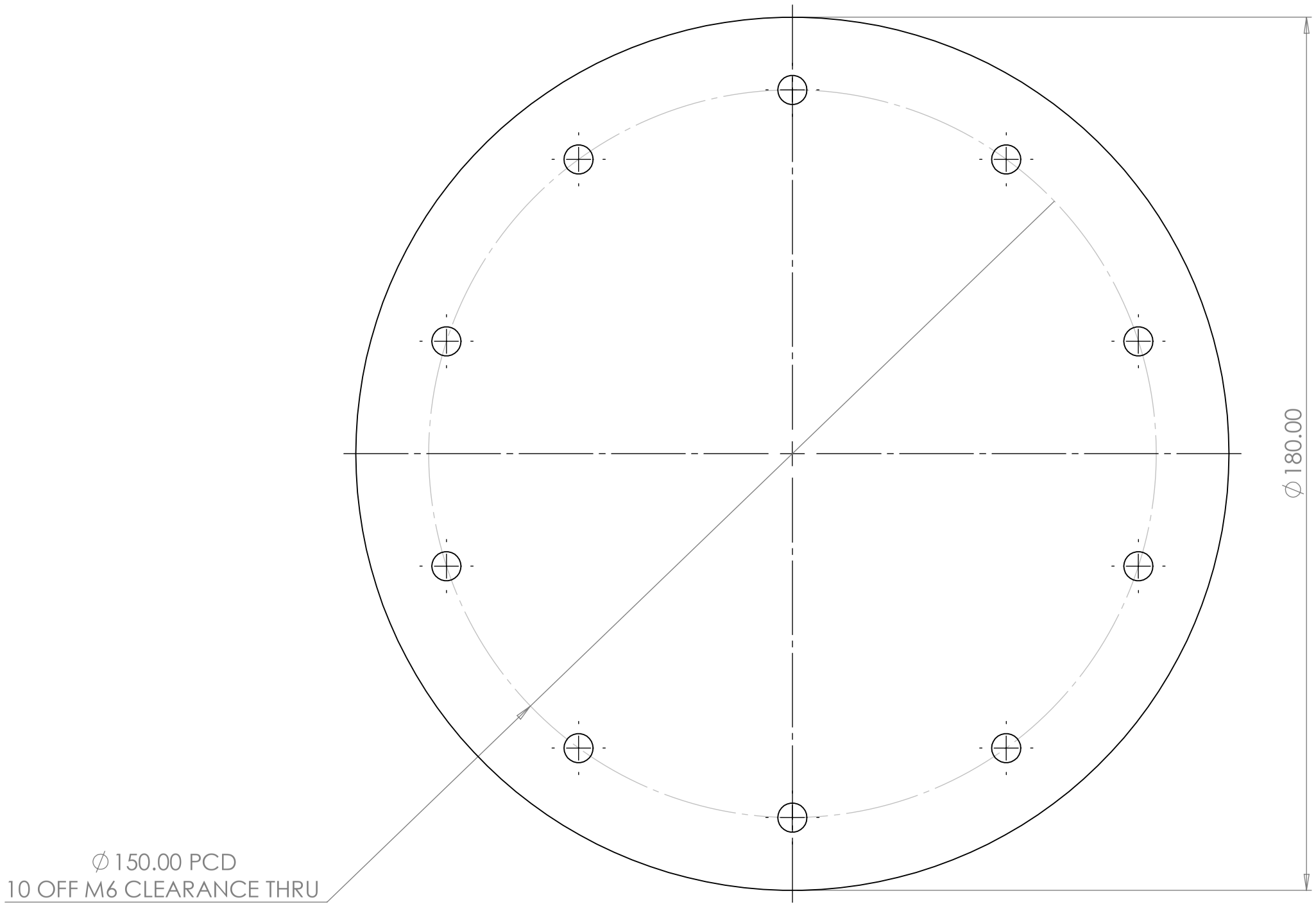

UNLESS OTHERWISE SPECIFIED: DIMENSIONS ARE IN MILLIMETERS SURFACE FINISH: TOLERANCES: LINEAR: ANGULAR:		FINISH:			DEBURR AND BREAK SHARP EDGES	DO NOT SCALE DRAWING	REVISION
	NAME	SIGNATURE	DATE			TITLE: Window	
DRAWN							
CHK'D							
APPV'D							
MFG							
Q.A				MATERIAL: POLYCARBONATE		DWG NO. 003	A3
				WEIGHT:		SCALE:1:1	SHEET 1 OF 1

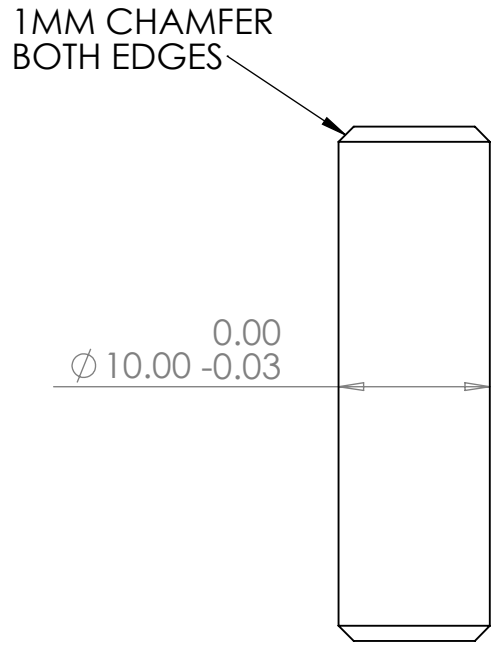

2 OFF

UNLESS OTHERWISE SPECIFIED: DIMENSIONS ARE IN MILLIMETERS SURFACE FINISH: TOLERANCES: LINEAR: ANGULAR:	FINISH:	DEBURR AND BREAK SHARP EDGES	DO NOT SCALE DRAWING / REVISION

	NAME	SIGNATURE	DATE
DRAWN			
CHK'D			
APPV'D			
MFG			
Q.A			

TITLE:

MOUNTING DOWEL

MATERIAL: STAINLESS STEEL	DWG NO. 004	A4
WEIGHT:	SCALE:2:1	SHEET 1 OF 1

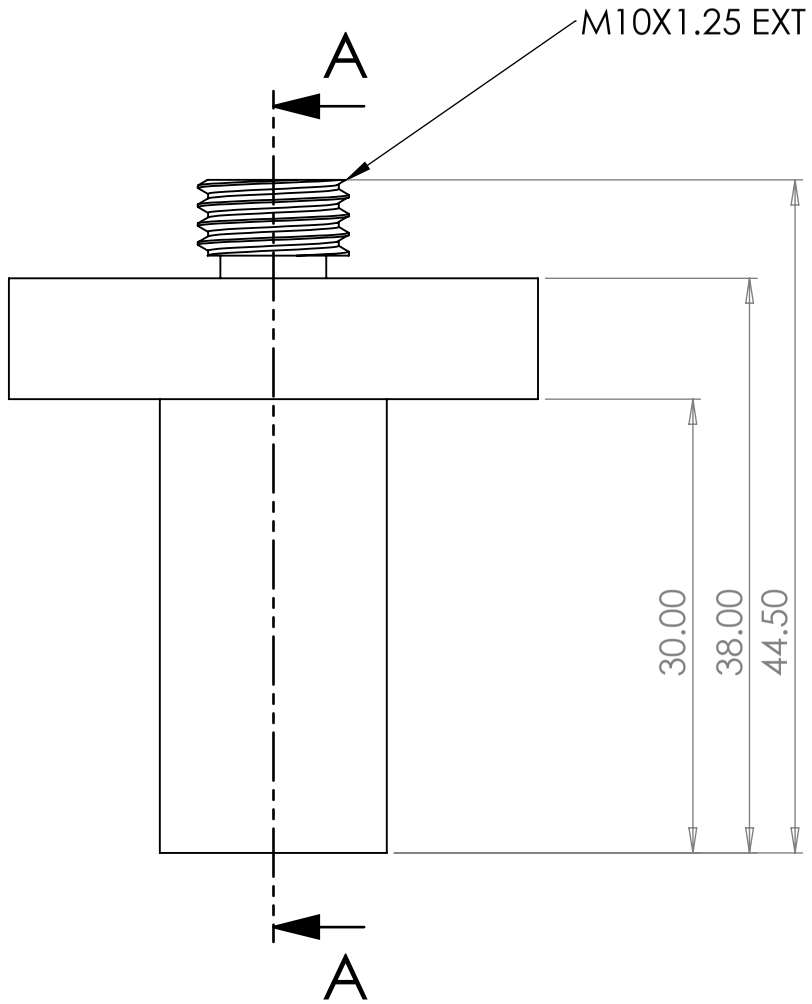

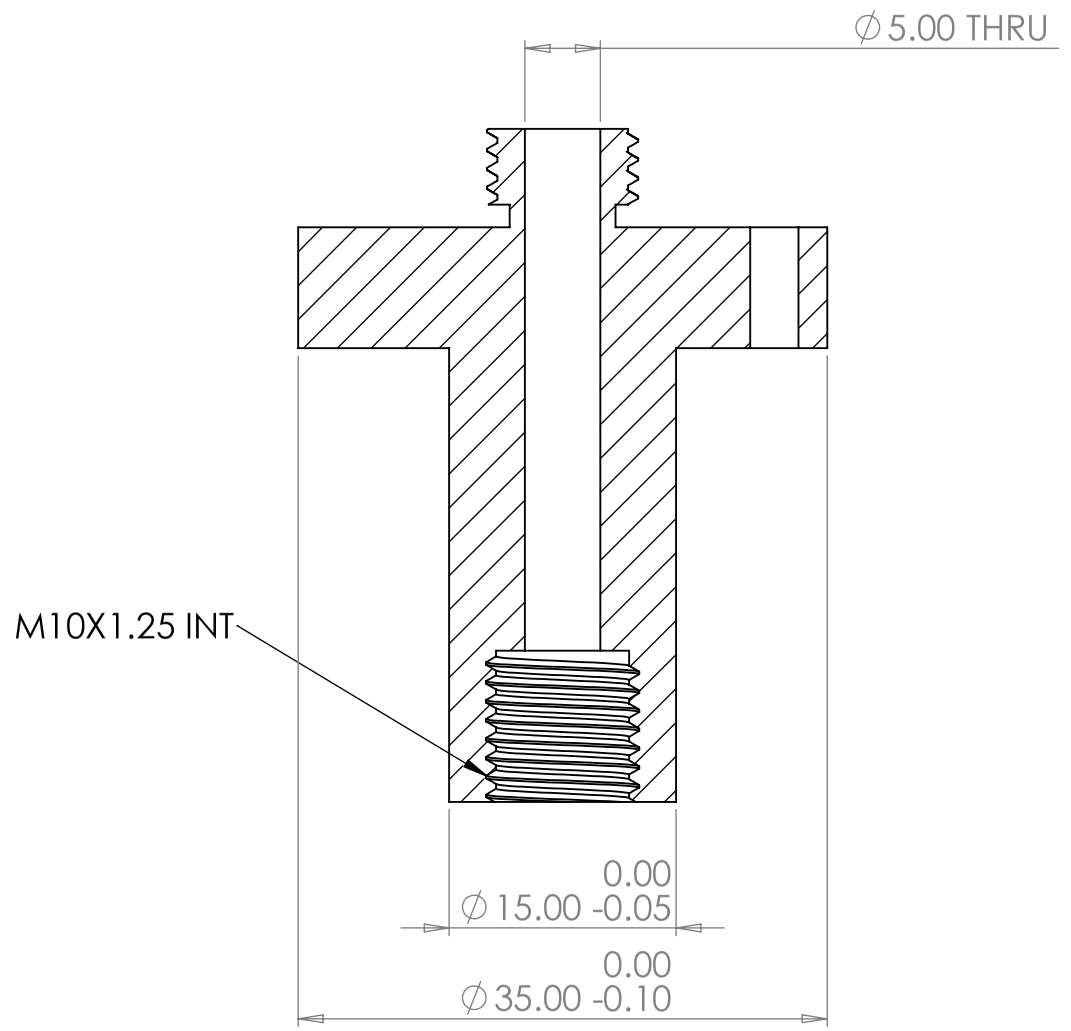

SECTION A-A

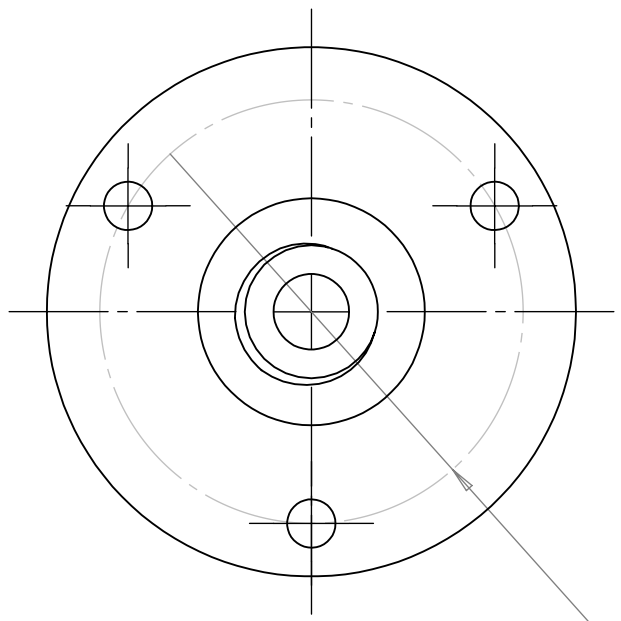

UNLESS OTHERWISE SPECIFIED: DIMENSIONS ARE IN MILLIMETERS SURFACE FINISH: TOLERANCES: LINEAR: ANGULAR:		FINISH:		DEBURR AND BREAK SHARP EDGES		DO NOT SCALE DRAWING	REVISION
	NAME	SIGNATURE	DATE			TITLE: SYRINGE ADAPTER	
DRAWN							
CHK'D							
APPV'D							
MFG							
Q.A				MATERIAL: STAINLESS STEEL		DWG NO. 005	A3
				WEIGHT:		SCALE:2:1	SHEET 1 OF 1